# Investigation of Slice Emittance Using an Energy-chirped Electron Beam in a Dispersive Section for Photo Injector Characterization at PITZ

Dissertation
zur Erlangung des Doktorgrades
des Departments Physik
der Universität Hamburg

vorgelegt von
Yevgeniy Ivanisenko
aus Charkiw

Hamburg

2012

| | |
|---|---|
| Gutachter der Dissertation: | Prof. Dr. Jörg Roßbach<br>Dr. Frank Stephan |
| Gutachter der Disputation: | Prof. Dr. Jörg Roßbach<br>Dr. Jens Osterhoff |
| Datum der Disputation: | 22.05.2012 |
| Vorsitzende/Vorsitzender<br>des Prüfungsausschusses: | Prof. Dr. Alexander Lichtenstein |
| Vorsitzender<br>des Promotionsausschusses: | Prof. Dr. Peter Hauschildt |
| Leiterin des Departments Physik: | Prof. Dr. Daniela Pfannkuche |
| Dekan der Fakultät fü Mathematik,<br>Informatik und Naturwissenschaften: | Prof. Dr. Heinrich Graener |

**Zusammenfassung**

In dieser Arbeit wird eine Diagnostik für die transversale Slice Emittanz mit einer effektiven zeitlichen Auflösung von bis zu 2 ps beschrieben, wie sie Photoinjektor Teststand in Zeuthen (PITZ) implementiert wird. Die Messungen wurden für verschiedene Elektronenpaketladungen, erzeugt durch einen Laserpuls mit zeitlichem Flat-Top-Profil mit 21-22 ps Halbwertsbreite, durchgeführt. Die Diagnostik erlaubt es, die Kompensation der projizierten Emittanz durch ein Solenoid-Magnetfeld experimentell zu untersuchen und trägt somit zur Strahlenemittanzoptimierung für die Anforderungen linacbasierten FELs im kurzen Wellenlängenbereich bei.

Die Diagnostik nutzt die Korrelation zwischen der longitudinalen Position eines Teilchens im Paket und seinem Impuls aus. Dadurch ist es möglich, mit Hilfe eines Dipolmagneten, die longitudinale Verteilung des Pakets in eine transversale Verteilung zu überführen. Ein schmaler Schlitz am Ausgang des Dipolmagneten schneidet einen kleinen Teil des Teilchenensembles, eine Scheibe (englisch: Slice), deren Emittanz auf einem Schirm mittels Slit-Scanoder Quadrupol-Scan- Technik analysiert wird.

In den Experimenten wurde beobachtet, dass die Werte der Slice Emittanz um 5-10 % niedriger sind als die Werte der projizierten Emittanz. Dies deutet eine hohe Effektivität der Solenoidkompensation hin. Aufgrund eines Strahlhalos zeigen Quadrupol-Scan-Technik und Slit-Scan-Technik unterschiedliche Messwerte für die Emittanz. Der beobachtete Halo umfasst nur 10 % der Elektronenpaketladung, trägt aber bis zu 40 % der Emittanz bei.

**Abstract**

This work describes a transverse slice emittance diagnostics with an RMS temporal resolution down to 2 ps that was implemented at the Photo Injector Test facility in Zeuten (PITZ). The measurements were performed for several bunch charges generated by a laser pulse that has a flat-top temporal profile of 21-22 ps FWHM duration. This diagnostics allows to study the beam projected emittance compensation with a solenoid magnetic field experimentally and therefore contributes to the beam emittance optimization for the needs of short wavelength linac-based FELs in particular.

The diagnostics is based upon the usage of electron bunches which have a correlation between the longitudinal position and the momentum of the bunch particles. This property allows to convert the bunch longitudinal distribution into a transverse one in a dipole magnet. A slit with a narrow opening at the dipole exit selects a fraction of the particle ensemble, a slice, which emittance is analyzed at a screen downstream. Slit scan and quadrupole scan techniques can be used to measure the emittance of the slices.

In the experiments it was found that the slice emittance values are 5-10% lower than the projected emittance values, indicating a good effectivity of the solenoid compensation. The emittance obtained using quadrupole scan technique has shown different results when compared to slit scan technique due to a beam halo. The observed beam halo in phase space contributes up to 40% of the emittance value while having only 10% of the bunch charge.

*To my dear family, Inna and Denis.*

# Contents

# Chapter 1

# Introduction

Nowadays particle accelerators are essential tools in a wide variety of research areas. Among numerous applications of charged particle beams, production of synchrotron radiation has become a rapidly developing branch of the accelerator technology. At the current stage the radiation generated by a free electron laser (FEL) combines highest peak intensity with almost full coherence. The FEL sources can produce femtosecond short pulses, hence giving a possibility for high time resolution experiments. The FEL radiation wavelength is tunable via the electron beam energy. All these valuable properties make electron accelerators a unique tool in the world of coherent radiation sources. Unlike conventional lasers FELs already can provide high-brightness coherent EUV [1] and X-ray radiation down to 0.15 nm [2].

The FEL operation in short wavelength regimes requires a high brightness driving electron beam. The high brightness is achieved by producing high peak current beams with low transverse emittance. One of the best candidates for the high-brightness electron beam generation is a photo injector.

Transverse emittance is an important beam property that characterizes the size and the divergence of the beam. The electron beam transverse emittance originates in the injector and only degrades during the beam transportation in a linear accelerator. One can not improve the transverse emittance downstream of the cathode, but the emittance degradation can be minimized. Therefore, the beam transverse emittance at the injector output is a key value for the FEL performance.

Checking and controlling the beam parameters in the FEL user facilities is an important and challenging task. Most of the beam parameters are

the direct consequence of the electron gun quality. To maximize the experimental up-time at user facilities worldwide all the possible beam studies are done in specially devoted injector test setups [3, 4, 5, 6, 7, 8]. The injectors of the Free electron LASer in Hamburg (FLASH), DESY, are conditioned, optimized and characterized at the Photo Injector Test facility in Zeuthen (PITZ) before they are delivered and installed to the main FEL linac. Also the electron source development for the European XFEL is done at PITZ.

Usually the transverse emittance of an electron bunch is characterized in terms of a projected emittance value. The electron bunch can have a complex longitudinal structure and therefore the transverse phase space distribution of the particles can change along the bunch. A transverse emittance diagnostics that has a sub-bunch temporal resolution is applied to study the bunch transverse slice emittance, which is defined as the emittance of the particles within a time window shorter than the bunch. The diagnostics allows to investigate e.g. the effect of the emittance compensation using a solenoid field. Several groups have already reported earlier about slice emittance measured at the photo injector output [9, 10]. Still the bunch charge used in the experiments does not exceed 300 pC and the emittance measurements were done using the quadrupole scan technique.

The bunch projected emittance is a standard optimization parameter at PITZ [11]. The mode of the injector operation assumes a significant contribution of the transverse-longitudinal coupling. The space charge contribution is minimized by applying solenoid compensation. Although the solenoid compensation is a sufficient technique to achieve the emittance required by the European XFEL [12] one can obtain more beam dynamics details from slice emittance studies for further setup developments and improvements.

This work describes a transverse slice emittance diagnostics based on the usage of an energy-chirped[1] electron beam in a dispersive section at PITZ and the first results for various bunch charges. The measurements at PITZ, which are presented in this thesis, were done with bunch charges up to 1 nC. The 1 nC measurements were performed using the quadrupole scan technique and the slit scan technique so that a comparison is possible.

The structure of this thesis is as follows.

The particle beam emittance definition is introduced and discussed in detail in Chapter 2. The beam dynamics that impacts the emittance is presented e.g. the beam emittance solenoid compensation. A linear transverse force acting on the bunch is considered an important case, when the

[1]The position of a particle within the bunch is correlated to its longitudinal momentum

transverse emittance is conserved. The emittance measurement techniques relevant to this thesis are presented.

A PITZ facility overview is given in Chapter 3. A short description of existing and planned diagnostics is presented, typical beam parameters from the setup simulations are shown.

Chapter 4 is devoted to the slice emittance diagnostics implementation at PITZ: the description of the components, the temporal resolution of the setup. The optics read-out system upgrade is given in details in this chapter. The data collection and processing procedures of the slice emittance diagnostics are presented as an important part of the emittance analysis.

In Chapter 5 the slice emittance measurement results are presented. The numerical simulation results of the setup are given as a reference for the experimental studies.

The thesis outcomes are summarized in Chapter 6. Future plans and experimental capabilities of the setup are reviewed and a list of proposed measurements is presented.

# Chapter 2

# Particle beam emittance and measurement techniques

Emittance is a basic particle beam property that plays an important role for accelerators. The chapter starts with an introduction of emittance and different definitions of emittance. Some text is devoted to definitions of thermal, projected and slice emittance. Beam emittance evolution along the beamline is another topic of this chapter. The final part of the chapter contains an overview of emittance measurement techniques that are involved in the slice emittance diagnostics.

## 2.1 Beam emittance

One can find original information about emittance in textbooks, e.g. [13, 14]. Let us only summarize the points which are important to follow the study line of this thesis.

**Particle distribution in phase space.** An electron bunch distribution volume in 6D phase space $[x, y, z, p_x, p_y, p_z]$ is called emittance. In practice we are dealing with a bunch of particles and the center of mass of the bunch is accelerated. The z axis is then chosen to coincide with the direction of movement in the laboratory coordinate system. One can split 6D phase space into a 2D longitudinal part $[z, p_z]$ and a 4D transverse part $[x, y, p_x, p_y]$. In the transverse part x and y planes can be separated if no coupling between the planes is present.

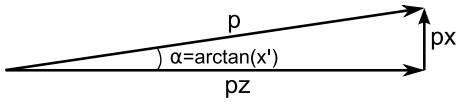


**Figure 2.1:** Divergence of an individual particle.

A phase space type that is applied in experimental studies of emittance is using divergences $x'$ and $y'$ rather than transverse momentum components $p_x$ and $p_y$. In order to distinguish it from the $[x, y, p_x, p_y]$ phase space it is called trace space, for more details see e.g. [15].

The relation between $x'$ and $p_x$ is illustrated by Fig. 2.1 and is explained below. The longitudinal momentum spectrum spread $\delta p$ of a bunch is assumed to be small compared to the mean momentum value $\bar{p}$. Also the particles' longitudinal momentum is typically much larger than the transverse momentum components. These two considerations result in a transverse momentum expression via the particle divergence $x'$ and the beam average longitudinal momentum $\bar{p}$:

$$p_x = x' \cdot p_z \approx x' \cdot \bar{p}. \tag{2.1}$$

The transverse phase space distributions from different z locations along the bunch can be combined together by integrating over the longitudinal distribution of the particles. The emittance value that corresponds to the obtained distribution is called transverse projected emittance. One usually controls the beam quality in terms of projected emittance.

From now on the term "transverse emittance" will appear in the text as the word 'emittance' only, unless it is directly specified differently.

It is convenient to use a statistical (RMS) emittance definition [16] in experiments. In this case emittance is the area of the particle distribution RMS equivalent ellipse (Fig. 2.2) in the trace space. The elliptic shape is coming from circular machines, where any shape of a transverse phase space distribution evolves into an ellipse while circulating [17]. Usually photo injector cathodes are homogeneous and a uniform cathode laser spot is a standard shape. In this case a bunch phase space distribution at the cathode has no correlation and can be characterized with two parameters only: the spot size and the transverse momentum spread of the emitted particles. Along the drift a distribution correlation develops. It is highly desired and all efforts are aimed to keep the correlation linear. The distribution characterization requires then one parameter more. If non-linearities can not

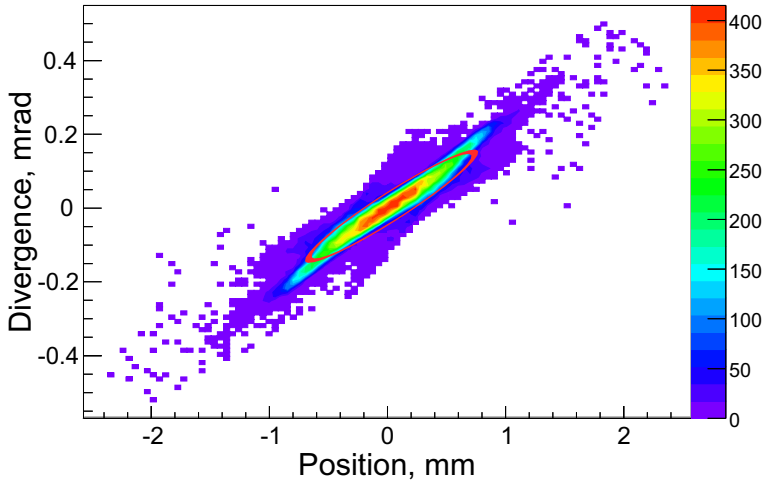


**Figure 2.2:** A phase space distribution in {y,y'} and the corresponding RMS equivalent ellipse.

be neglected an RMS emittance value does not describe the phase space distribution uniquely.

With three parameters one defines a unique RMS equivalent ellipse. The ellipse is defined by the following equation:

$$\sigma_{x'}^2 x^2 - 2\langle xx'\rangle x \cdot x' + \sigma_x^2 x'^2 = \varepsilon^2, \tag{2.2}$$

where $\sigma_{x'}$, $\langle xx'\rangle$, $\sigma_x$ are the statistical second order moments of the particle distribution in trace space.

An ellipse area $S$ in trace space is expressed via the statistical parameters [17]:

$$S = \pi\sqrt{\sigma_x^2\sigma_{x'}^2 - \langle xx'\rangle^2} = \pi\varepsilon, \tag{2.3}$$

where $\varepsilon$ is now emittance.

Eq. 2.3 contains divergence terms dependent on the longitudinal momentum, in such a way that beam emittance is reduced during an acceleration process. Invariant emittance is obtained via an energy normalization that results in the definition of RMS normalized emittance [17]:

$$\varepsilon = \beta\gamma\sqrt{\sigma_x^2\sigma_{x'}^2 - \langle xx'\rangle^2}, \tag{2.4}$$

where $\beta = v/c$, $\gamma$ is the Lorentz factor. The normalized emittance definition expressed via Eq. 2.4 is used from now on in this work.

## 2.2 Beam emittance origin and evolution in an injector

Initial, also known as thermal, electron bunch emittance originates from the emission process at the cathode. The cathode is considered to have homogeneous emission properties over its complete surface. In this case the bunch phase space distribution has no $\{x, x'\}$ correlation. It means only two distribution parameters are required for the emittance evaluation: the transverse emission area RMS size and the transverse momentum RMS spread of the emitted particles. Once the cathode material, the cathode surface properties, and the cathode laser wavelength are defined, there are only minor effects, which can influence the transverse momentum distribution and its RMS spread. Therefore emittance can be minimized directly in the accelerator by reducing the laser spot size at the cathode. The minimum size is limited by the bunch space charge for a constant laser pulse length. Once the limit is reached the longitudinal profile becomes modulated by the reduced emission capability in the presence of the electric field of previously emitted particles. This effect is known as a virtual cathode formation. The first emitted portion of the bunch charge creates a field that can get even higher than the charge extracting RF gradient at the cathode and the particles can not escape the cathode surface or they are reflected back to the cathode. The space charge field decreases while the charge moves away and it allows to emit another charge portion and the process repeats. As it is mentioned below the final emittance consists of several contributions and, though the thermal emittance is reduced, the space charge can induce a dominating transverse emittance growth. Therefore there must be an optimum of the laser spot size to obtain the minimal transverse emittance at the gun output, which is a compromise between the thermal emittance and the space charge contribution to the transverse emittance value.

The laser pulse duration is optimized to achieve the maximum electron beam brightness [18]. And therefore not only the bunch charge maximization is important, but also one needs to keep the transverse emittance low simultaneously. A shorter pulse duration means a larger optimum spot size at the cathode for a constant bunch charge. It results in a higher thermal emittance contribution. A longer pulse duration means a lower thermal emittance can be reached, but because the difference in the RF field along the bunch starts to contribute to the resulting projected transverse emittance of the bunch at the gun output, the peak current achievable after

bunch compression is limited.

As an intermediate conclusion one states that there are three main contributors to the projected transverse emittance of the bunch:

1. emission process,

2. bunch space charge,

3. RF field.

Thermal emittance originates from the emission process at the cathode. If the cathode is homogeneous over the emission area the generated beam distribution in trace space does not have a correlation. The emittance value is then obtained from 2.4 considering that monoenergetic particles are emitted:

$$\beta\gamma = \frac{p}{m_0 c}, \tag{2.5}$$

$$\sigma_{x'} = \sqrt{< x'^2 >} = \sqrt{< \left(\frac{p_t}{p}\right)^2 >} = \frac{\sigma_{p_t}}{p}. \tag{2.6}$$

From this one derives the thermal emittance expression

$$\varepsilon_{th} = \frac{1}{m_0 c}\sigma_{cath}\sigma_{p_t}, \tag{2.7}$$

where $\sigma_{cath}$ is the RMS size of a round emission spot on the cathode (laser spot size for a photo injector), $\sigma_{p_t}$ is the RMS particle transverse momentum value in one plane. By substituting the RMS transverse momentum with the emission energy $E_{kin}$ in Eq. 2.7 the thermal emittance can be parameterized in the frame of an emission model by

$$\sigma_{p_t} = \sqrt{2m_0\frac{E_{kin}}{a_m}} \tag{2.8}$$

with $a_m$ being the model factor between the mean and RMS values of a particles' momentum distribution. If for example monoenergetic particles ($E_{kin}$) are emitted isotropically in a semisphere then $a_m = 3$ [19]. The emittance results in

$$\varepsilon_{th} = \sigma_{cath}\sqrt{\frac{2E_{kin}}{a_m m_0 c^2}}. \tag{2.9}$$

From Eq.2.9 one sees that to minimize thermal emittance one has to reduce the emission spot size and the "transverse" emission energy of the particles. The emission energy is defined by the cathode material, the surface properties and the laser wavelength of a photo injector. The spot size reduction leads to a growing role of space charge effects in the resulting beam emittance. The minimization of the resulting emittance via the laser spot size is a compromise between the thermal emittance and the contribution of the space charge.

Space charge and RF fields contribute in a similar way to bunch emittance. In the first approximation the fields are considered linear with the radial coordinate. The interest in this approximation arises from the fact that transverse RMS emittance is conserved. Still the projected emittance can be changing because these linear forces may vary along the bunch.

When linear forces are considered:

$$\dot{p}_x = F_x(x) = q(z)x. \tag{2.10}$$

An assumption is made that particles are monoenergetic and the energy stays constant. Switching from time derivatives to z coordinate derivatives, Eq. 2.10 can be rewritten

$$\frac{d^2x}{dz^2} = x''_{zz} = \frac{q(z)}{v^2\gamma m_0}x. \tag{2.11}$$

This is a second order non-linear differential equation

$$x''_{zz}(z) + Q(z)x(z) = 0 \tag{2.12}$$

with $Q(z) = -q(z)/v^2\gamma m_0$. This equation is known as the Hill equation. The initial conditions include the particle coordinate $\mathrm{x}_0$ and divergence $\mathrm{x}'_0$ at z=0 m:

$$x(0) = x_0, \tag{2.13}$$
$$x'(0) = x'_0, \tag{2.14}$$

taking into account 2.13, the function x(z) and its derivative can be represented as a sum of two components dependent on z

$$x = x_0\, g(z) + x'_0\, h(z), \tag{2.15}$$
$$x' = x_0\, g'(z) + x'_0\, h'(z), \tag{2.16}$$

where functions g(z) and h(z) meet the initial values of

$$g(0) = 1,\ g'(0) = 0,\ h(0) = 0,\ h'(0) = 1. \tag{2.17}$$

The coordinate and divergence functions are linearly dependent on the initial values and these transport equations can be represented by a particle transport matrix (more about linear beam optics and transport matrix formalism can be found in [20]):

$$\begin{pmatrix} x \\ x' \end{pmatrix} = M_p \begin{pmatrix} x \\ x' \end{pmatrix}_0, \tag{2.18}$$

where $M_p$ is:

$$M_p = \begin{pmatrix} g(z) & h(z) \\ g'(z) & h'(z) \end{pmatrix}. \tag{2.19}$$

The volume in the space of the new coordinates x,x' is expressed via the initial volume times the determinant of the Jacobian matrix J:

$$\mathrm{dxdx'} = \det\ \mathrm{J}\, \mathrm{dx_0 dx'_0} = (\mathrm{gh' - g'h}) \mathrm{dx_0 dx'_0}. \tag{2.20}$$

Liouville's theorem results in $f(x, x') = f(x_0, x'_0)$ The emittance of the transformed phase space distribution can be calculated using formula 2.4, where:

$$\begin{aligned} \sigma_x^2 &= (gh' - g'h) \frac{\iint x^2 f(x, x') dx dx'}{\iint f(x, x') dx dx'} \\ &= (gh' - g'h) \frac{\iint (x_0\, g(z) + x'_0\, h(z))^2 f(x_0, x'_0) dx_0 dx'_0}{\iint f(x_0, x'_0) dx_0 dx'_0}, \end{aligned} \tag{2.21}$$

$$\begin{aligned} \sigma_{x'}^2 &= (gh' - g'h) \frac{\iint x'^2 f(x, x') dx dx'}{\iint f(x, x') dx dx'} \\ &= (gh' - g'h) \frac{\iint (x_0\, g'(z) + x'_0\, h'(z))^2 f(x_0, x'_0) dx_0 dx'_0}{\iint f(x_0, x'_0) dx_0 dx'_0}, \end{aligned} \tag{2.22}$$

$$\begin{aligned} \overline{xx'} &= (gh' - g'h) \frac{\iint xx' f(x, x') dx dx'}{\iint f(x, x') dx dx'} \\ &= (gh' - g'h) \frac{\iint (x_0\, g(z) + x'_0\, h(z))(x_0\, g'(z) + x'_0\, h'(z)) f(x_0, x'_0) dx_0 dx'_0}{\iint f(x_0, x'_0) dx_0 dx'_0}. \end{aligned} \tag{2.23}$$

The expressions above show that the beam parameters RMS size squared, RMS divergence squared, and position-divergence covariance are linearly transformed along the beamline in case of linear forces. A beam transport matrix $M_b$ can be evaluated from equations 2.21-2.23:

$$\begin{pmatrix} \sigma_x^2 \\ \overline{xx'} \\ \sigma_x'^2 \end{pmatrix} = M_b \begin{pmatrix} \sigma_x^2 \\ \overline{xx'} \\ \sigma_x'^2 \end{pmatrix}_0, \tag{2.24}$$

where $M_b$ is equal to:

$$M_b = (gh' - g'h) \begin{pmatrix} g^2 & 2gh & h^2 \\ gg' & g'h + gh' & hh' \\ g'^2 & 2g'h' & h'^2 \end{pmatrix}. \tag{2.25}$$

Therefore a new emittance value from 2.4 equals

$$\begin{aligned} \varepsilon^2 = \beta^2\gamma^2(gh' - g'h)^2 \\ \cdot ((g^2\sigma_{x0}^2 + 2gh\overline{xx'}_0 + h^2\sigma_{x'0}^2)(g'^2\sigma_{x0}^2 + 2g'h'\overline{xx'}_0 + h'^2\sigma_{x'0}^2) \\ - (gg'\sigma_{x0}^2 + (g'h + gh')\overline{xx'}_0 + hh'\sigma_{x'0}^2)^2) \\ = \beta^2\gamma^2(gh' - g'h)^4(\sigma_{x0}^2\sigma_{x'0}^2 - \overline{xx'}_0^2) \\ = (gh' - g'h)^4\varepsilon_0^2 \end{aligned} \tag{2.26}$$

if Jacobian $(gh' - g'h)^2 = 1$ for any z then transverse emittance is conserved along the beamline.

The equation of motion for a linear force constant at a certain section along the particles trajectory turns to a second-order linear differential equation:

$$x''_{zz}(z) + k^2 x(z) = 0, \tag{2.27}$$

where $k^2 = -q/v_z^2\gamma m_0$.

The particle transport matrix $M_p$ in this case equals:

$$M_p = \begin{pmatrix} \cos kz & \frac{1}{k}\sin kz \\ -k\sin kz & \cos kz \end{pmatrix}. \tag{2.28}$$

The beam transport matrix $M_b$ can be evaluated from 2.25:

$$M_b = \begin{pmatrix} \cos^2 kz & \frac{2}{k}\cos kz\sin kz & \frac{1}{k^2}\sin^2 kz \\ -k\cos kz\sin kz & \cos^2 kz - sin^2 kz & \frac{1}{k}\sin kz\cos kz \\ k^2\sin^2 kz & -2k\sin kz\cos kz & cos^2 kz \end{pmatrix}. \tag{2.29}$$

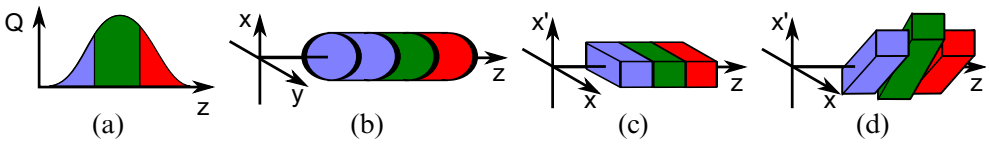


**Figure 2.3:** (a) and (b): a cylindric beam with a gaussian longitudinal distribution. (c): three different parts along the bunch that are matched. (d): the alignment is lost due to the space charge.

The RF fields induce transverse acceleration of the charged particles as well. In a paraxial approximation these forces depend linearly on the transverse distance from the axis. In our particular example an RF cavity is operated with a standing wave. The accelerating electrical field on the axis is:

$$E_z = E_0 \cos kz \sin(\omega t + \psi), \tag{2.30}$$

using the Maxwell's equations for the electro-magnetic field in free space [21] one can find that the two components responsible for the field radial force equal to

$$E_r = \frac{kr}{2} E_0 \sin kz \sin(\omega t + \psi), \tag{2.31}$$

$$B_\phi = \frac{\omega r}{2c} E_0 \cos kz \cos(\omega t + \psi). \tag{2.32}$$

Both are linear with $r$. The final radial momentum obtained from the field is calculated by integrating the impact of these components along the cavity.

An important qualitative example of a linear force impact on a bunch is space charge. The space charge transverse force varies along a finite length bunch and the variation is dependent on the current profile. The most simple bunch shape to be produced in photo injectors is a cylinder shape. It is produced by a laser pulse with a homogeneous transverse spot and a gaussian or a uniform temporal profile: both will result in an electron beam shape that has the charge density in the longitudinal center higher than at the beginning and the end of the bunch. In this case the maximum of the radial space charge force occurs at the middle part of the bunch. Particles of this part have higher divergence caused by the space charge than those in the tails. This leads to a mismatch of different longitudinal parts in transverse phase space and hence the projected emittance grows (Fig 2.3). In case of a uniform laser temporal profile the effect is smaller.

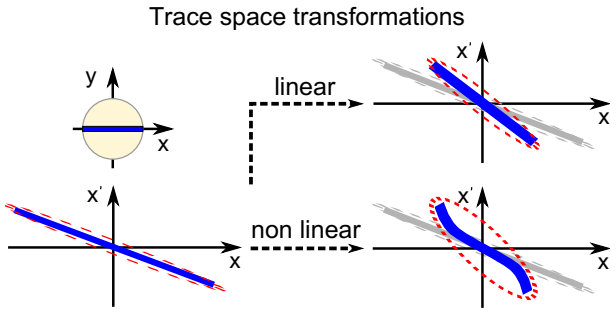


**Figure 2.4:** Linear and non-linear phase space distribution transformations of a bunch horizontal cut. Blue solid line - phase space distribution; red dotted ellipse - 6-RMS emittance; grey contours indicate the initial state before the transformation.

Non-linear transformations of a phase space distribution itself is a complex problem and deserves a separate comprehensive study. Important for this thesis is that these effects can change the transverse RMS emittance and therefore have to be mentioned. The effect is considered in two stages. First, a non-linear transformation of a beam transverse section along X is presented in Fig. 2.4. The result of the distortion is that the RMS emittance grows (dashed ellipse), while the geometrical area and the peak charge density of the phase space distribution stays approximately the same as for the linear transformation. The complete beam phase space distribution would look like the 100% case in Fig. 2.5. The figure shows a simulated experiment where it was possible to associate the low intensity high divergence part of the phase space distribution with the particles starting in the outer ring of the transverse profile at the cathode. A short longitudinal part (about a picosecond) of the bunch was used to exclude longitudinal difference in the transverse dynamics. Then a circle was placed that fully includes the laser spot on the cathode. The circle radius was reduced with a certain step and all the particles outside of it were removed from the phase space distribution obtained at 5 m downstream. In the result we see that the low intensity part, which tends to rotate clock-wise when propagating downstream, is reduced, and when the charge is cut down to 57% only the high charge density part of the distribution remains, which rotates counter-clock wise. At some point along the setup these two parts will overlap again and this will be the minimum slice emittance. The point of this example is to show that non-linear transformations change the RMS emittance of a small longitudinal fragment

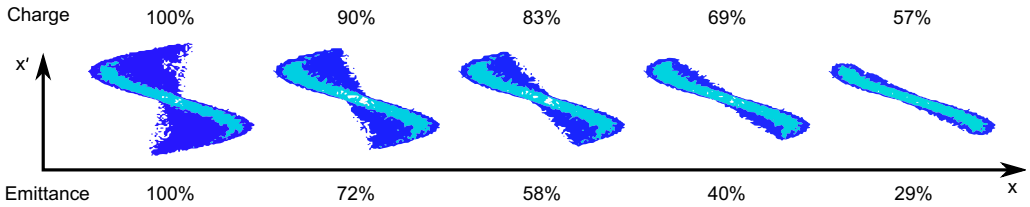


**Figure 2.5:** A progressive cut applied to a transverse phase space distribution of a beam slice by discriminating the particles, which started in the outer ring at the cathode.

of the bunch (slice), and the projected emittance is of course affected as well. Linear forces can change the projected emittance if they change along the bunch, but the slice local emittance stays constant.

At first glance a flat-top shaped laser with a homogeneous transverse spot generates a pencil like electron beam that should not experience non-linear fields in this spatial configuration. But the bunch is distorted by the space charge in the first millimeters in the cavity in such a way that the sharp edge is diluted and a finite length charge density transition appears allowing non-linear space charge to increase emittance.

Let's switch back to the problem of the slice mismatch due to different transverse space charge forces applied along the bunch. There is one technique to compensate the linear space charge contribution to the projected emittance. It utilizes a solenoid magnet with which an injector is usually equipped to focus the beam already in the cavity. The experimental technique was originally proposed in [22]. Describing this effect is not the aim of this thesis, it is still important to introduce it qualitatively. The schematics 2.6 shows principle stages of the compensation process. Although there is a strict order of appearance in the figure the processes can not be sepa-

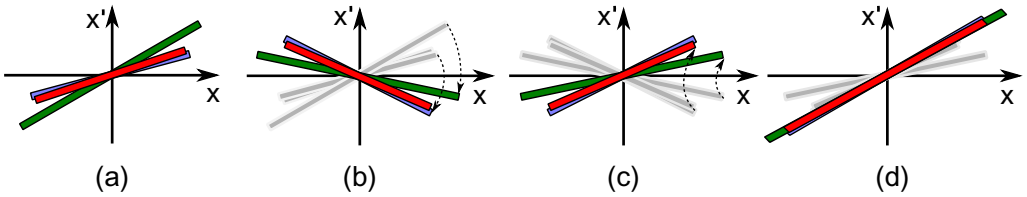


**Figure 2.6:** Projected emittance compensation using a solenoid magnet in an injector area.

rated in time. For a more distinct explanation we have to mention them as they would happen consequently. The uniform charge distribution from Fig. 2.3 is drifting from the cathode and the transverse space charge is not equal along the bunch, which results in a mismatch of the phase spaces as in Fig. 2.6(a). At this point a solenoid focusing is applied. The focussing effect shows up rotating the distribution clockwise in phase space (Fig. 2.6(b)). The middle bunch part that had a leading divergence now has lower convergence than the edge parts. From this stage the bunch is drifting in a free space and as mentioned above, we split the pure drift and the space charge impact into two stages, although they are happening at the same time. Another assumption that has to be made is that the particles do not cross the divergence axis (laminar flow, no cross-over particles). This is true when the process is highly space charge dominated. Convergent particles of the bunch in a drift then will lose transverse kinetic energy in the electric field of the charge, stop and turn to gain transverse momentum in the other direction Fig. 2.6(c). At the same transverse distance from the bunch center they will get back the same kinetic energy they had just after the solenoid focusing. This transformation corresponds to mirroring the phase space distribution across the x axis and does include the first crossing of the phase space distributions. If the periods of the process for different parts of the bunch are close to equal a situation occurs where the edge parts have higher divergence then the middle. At the same time the middle part is accelerated by the space charge stronger and at some point it can get matched with distributions of the edge parts again, the second time, see Fig. 2.6(d). A projected emittance compensation example from ASTRA simulations is shown in Appendix A.1. A double emittance minima structure forms along the z axis and the corresponding slice orientations in phase space are presented.

The dynamics description above has shown that the projected phase space distribution might have higher emittance than individual longitudinal part transverse distributions. In case of full matching with the solenoid one can expect that the projected emittance is just an average transverse emittance weighted value along the bunch. A criterium that could show how well the distributions are overlapped in phase space (the quality of compensation) would be a measurement of the transverse emittance of the charge fraction within a longitudinal gate shorter than the bunch length. It is the same as slicing the bunch into several longitudinal pieces and analyzing emittance for each one of them separately. Introducing a slice phase space diagnostics opens a broad variety of new details to discover about the phase

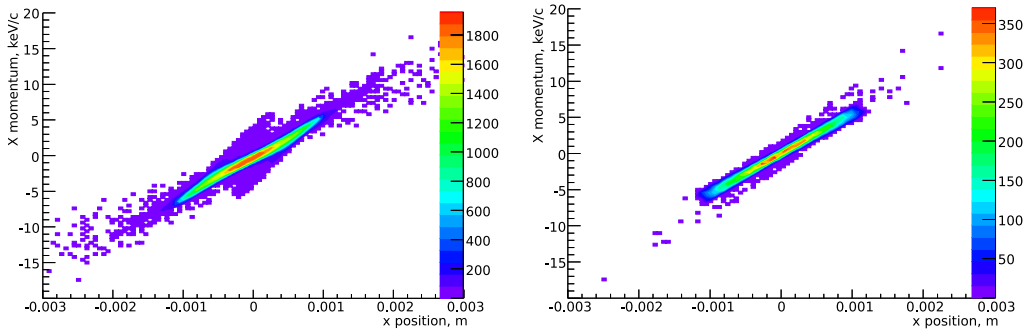


(a): bunch projected




(b): tail part

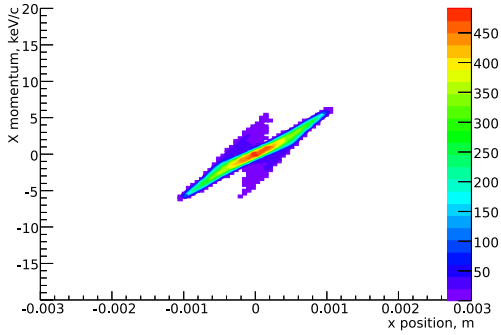


(c): middle part

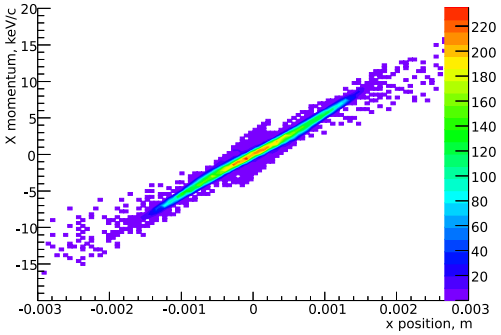


(d): head part

**Figure 2.7:** A simulated (ASTRA) optimized projected phase space distribution of the bunch and of different parts separately. The full bunch emittance is 0.63 mm mrad; tail - 0.45 mm mrad; middle (highest current) - 0.62 mm mrad; head - 0.75 mm mrad.

space distribution of the beam.

Slice emittance diagnostics based on using an energy chirped beam after a dipole for the high-brightness electron beam injector at PITZ is the main topic of this thesis. With the setup described in Chapter 4 one is able to measure the beam slice phase space distributions for the pre-optimized projected emittance with only small change in the accelerator parameters. Such a measurement can certainly help to understand if the beam needs any further optimization to minimize the projected emittance and offers a possibility to minimize the central part slice emittance, that is mainly affected by the non-linear effects. Fig. 2.7 shows a well optimized full beam phase space distribution along with the head, center and tail phase space distributions of the same bunch.

## 2.3 Methods for transverse emittance measurements

The discussion above will be completed in this section with an overview of the emittance measurement techniques which are applied for the slice emittance diagnostics at PITZ.

The two techniques described here are quadrupole and slit scans. Both are based upon the beam size measurements for which a variety of techniques was developed.

### 2.3.1 Beam transverse profile measurements

A beam transverse profile is defined as the charge distribution in the plane perpendicular (XY plane) to the flight direction (Z axis). The distribution is a projection of all the bunch particles on the transverse plane in contrast to a transverse profile section where only particles at a particular Z position are taken into account. The beam intensity is measured as a function of the two transverse coordinates $f(x, y)$.

A beam profile measurement can be conducted using a direct charge measurement device (e.g. micro-strip detectors) or converters to light (e.g. scintillative materials, optical transition radiation OTR and optical diffraction radiation ODR, synchrotron radiation [23, 24], residual gas ionization [25]) in combination with photon detectors. From the structural point of view the detector can be a combination of multiple sensitive elements that allow a single shot measurement. Alternatively position of a single sensitive element can be scanned to reconstruct the spatial distribution. Sometimes the converter position is scanned (e.g. wire scanner, variations of this technique include a laser wire [26]; beam sizes at tens of nanometers scale can be measured using Shintake monitor [27]).

When an electron beam is converted into photons proper imaging to the sensor has to be provided. There are three contributors to the resolution in this case: the converter, the transport, and the sensor.

Common converter screens are based on scintillating material. A scintillator is an insulating material and they can suffer from break through by the collected charge. This is usually avoided by using a conductive substrate (aluminum or silicon). The scintillator thickness is chosen to produce the maximum number of photons per unit of area with the effect of blurring due to the scattering of particles still being negligible [28]. The resolu-

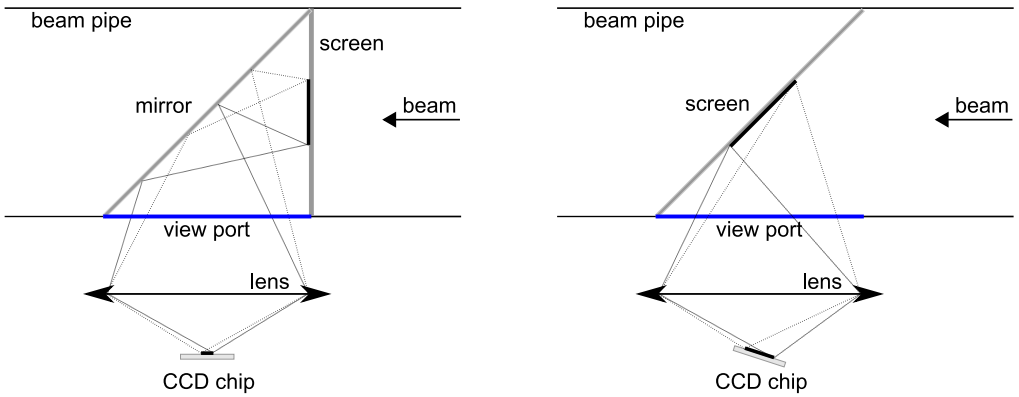


**Figure 2.8:** The 90 (left) and 45 (right) degrees screen geometry sketch. For the 45 degrees geometry the camera is placed according to the Scheimpflug rule (see text, or section 4.4).

tion depends on the thickness, the material type (monocrystal, polycrystal, powder), and the scintillator type (YAG, BGO, ...). Beam parameters like energy or density are also influencing the resolution ( electron scattering in the screen material, saturation [29]). YAG screens can be used in 90 degrees and in 45 degrees geometry (Fig 2.8), although in both cases they destruct the beam.

In the OTR screen the radiation is created directly on the surface. This fact allows to minimize the beam disturbance by using the 45 degree geometry of the screen where the backward radiation is emitted into a cone perpendicular to the beam axis (Fig. 2.9). The OTR method in beam diagnostics is described in [30].

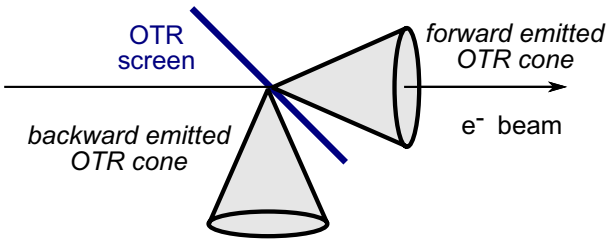


**Figure 2.9:** An OTR screen in 45 degree geometry: the forward emission cone is coaxial with the beam axis; the backward cone is emitted perpendicular to the beam axis.

A single electron crossing the OTR screen causes radiation formation by the mirror charge distributed over a finite transverse area of the screen. Additionally there is a diffraction contribution due to the limited aperture of the read-out system $\theta_{apert}$. As it is shown in [31] the approach results in the beam size resolution limit of:

$$\sigma \simeq \frac{4(\gamma\lambda)^2}{6\ln(\gamma\theta_{apert})}, \tag{2.33}$$

where $\gamma$ is the Lorentz factor; $\lambda$ is the OTR wavelength used for the imaging; the aperture size is expressed in radians. Some comparison between scintillating and OTR screen resolution can be found in [29, 32, 33].

Screen positioning at other angles is possible too and can have advantages for high energy beams [34]. The 90 degree case has the advantage of the parallel layout of the elements. The Scheimpflug rule [35] has to be applied for the 45 degree arrangement to avoid problems with depth of focus, if required. But it can be sufficient to position the camera parallel to the lens if one only measures small transverse distributions within the depth of focus on the axis of the optical system (e.g. quadrupole scan). For more details refer to section 4.4.

### 2.3.2 Single quadrupole magnet scan

Applying the quadrupole scan method one can measure the phase space distribution using the tomographic reconstruction [36]. A simplified approach discussed below allows to obtain only the second order moments of the distribution required for the emittance value calculation. These three parameters do not define a unique distribution, but the model is well applicable for linear phase space distributions. In a photo injector phase space distributions are linear at the cathode and only linear beam transport optics is used. The non-linearities are first of all induced by the space charge and then by the accelerating fields and beam optics imperfections.

If fields of a quadrupole magnet are considered linear then the transport matrix can be derived from Eq. 2.29. A method of emittance measurement can be based on defining the phase space distribution statistical momenta from a set of beam size measurements. The beam is transported from the location where the emittance has to be found ($z_0$) downstream to a screen ($z_1$). The beam size is measured for three known transport matrices. The beam sizes are expressed using the first line of the beam transport matrices

and the required beam parameters:

$$\begin{pmatrix} \sigma_{x1}^2 \\ \sigma_{x2}^2 \\ \sigma_{x3}^2 \end{pmatrix}_{z_1} = \begin{pmatrix} M_{b1}^{11} & M_{b1}^{12} & M_{b1}^{13} \\ M_{b2}^{11} & M_{b2}^{12} & M_{b2}^{13} \\ M_{b3}^{11} & M_{b3}^{12} & M_{b3}^{13} \end{pmatrix} \begin{pmatrix} \sigma_x^2 \\ \langle xx' \rangle \\ \sigma_{x'}^2 \end{pmatrix}_{z_0} . \tag{2.34}$$

To find the emittance one has to solve this system of equations.

For the quadrupole scan technique the transport matrix consists of a quadrupole magnet matrix and a drift space matrix. The full transport matrix is changed by tuning the current of the quadrupole magnet. To keep the conventional notations we need to introduce the quadrupole strength via k from Eq. 2.12 $K \equiv k^2$. According to Eq. 2.10 $K = -q/(v^2 \gamma m_0)$. From the definition of the Lorentz force [21] we derive

$$q = evG \tag{2.35}$$

with $e$ - charge of the electron; $v$ - velocity of the electron; $G$ - gradient of the quadrupole magnet. And therefore

$$K = \frac{eG}{p}. \tag{2.36}$$

Then the quadrupole magnet transport matrix $M_b$ from Eq. 2.28 is equal to:

$$M_p = \begin{pmatrix} cos(\sqrt{K} l_q) & \frac{1}{\sqrt{K}} sin(\sqrt{K} l_q) \\ -\sqrt{K} sin(\sqrt{K} l_q) & cos(\sqrt{K} l_q) \end{pmatrix}, \tag{2.37}$$

where $l_q$ is the quadrupole magnet effective field length [20].

The measurement arrangement includes a drift after the quadrupole. The drift space corresponds to $k = 0$. In this case the transport matrix turns into:

$$\begin{pmatrix} 1 & L_d \\ 0 & 1 \end{pmatrix}, \tag{2.38}$$

where $L_d$ is the drift length. To obtain the beam transport matrix of the system consisting of the quadrupole magnet and the drift space, first, we derive the separate beam transport matrices using Eq. 2.29 and then multiply them.

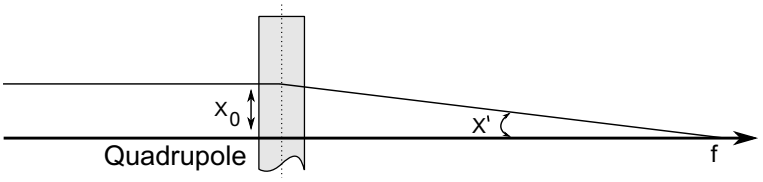


**Figure 2.10:** A paraxial particle is focused by a quadrupole magnet and crosses the on-axis focal point.

**Thin lens model.** A thin lens model is used to explain the basic properties of a quadrupole focusing lens. The assumption of this model is that $\sqrt{K}l_q \ll 1$. The quadrupole is at $z = 0$ position. A paraxial particle is bent and passes the focal point $z = f$ (Fig. 2.10). Then the tangent of the convergence angle $x'$ after the quadrupole is approximated with the angle itself. On the other hand the convergence angle after the quadrupole magnet is defined from its particle transport matrix (Eq. 2.37):

$$\frac{x_0}{f} = \tan x' \approx x' = -x_0\sqrt{K}\sin\sqrt{K}l_q + x'_0\cos\sqrt{K}l_q \approx -x_0 K l_q. \qquad (2.39)$$

Finally the focal length of the thin quadrupole lens is given by:

$$f = \frac{1}{Kl_q}. \qquad (2.40)$$

Using the focal length we can express the beam size at a distant screen ($L_d$ meters downstream from the quadrupole magnet) using a combined transport matrix of the quadrupole magnet and the drift to the screen:

$$\sigma^2_{scr} = (1 - \frac{L_d}{f})^2\sigma^2_x + 2(1 - \frac{L_d}{f})L_d\langle xx'\rangle + L^2_d\sigma^2_{x'}, \qquad (2.41)$$

where $\sigma_{scr}$ is the beam size at the observation screen, $\sigma^2_x$, $\langle xx'\rangle$, $\sigma^2_{x'}$ are second order moments of the beam trace space distribution in the principal plane of the quadrupole magnet. The derivative of the right part of Eq. 2.41 over the focal length equals zero for the minimum size measured at the screen in the quadrupole current scan. This relation allows to calculate the optimum focal length of the quadrupole magnet:

$$\frac{1}{f_{opt}} = \frac{\langle xx'\rangle}{\sigma^2_x} + \frac{1}{L_d}. \qquad (2.42)$$

Substituting the focal length with the optimum value in Eq. 2.41 one obtains the minimum size $\sigma_{scr}^{min}$:

$$\sigma_{scr}^{min} = \frac{L_d \varepsilon}{\gamma \beta \sigma_x}, \tag{2.43}$$

where $\varepsilon$ is the normalized emittance of the beam in the quadrupole magnet principle plane, $\beta$ is a relative velocity, $\gamma$ is the beam Lorentz factor (the energy spread is neglected).

The size at the observation screen is affected by the bunch energy spread due to the quadrupole magnet chromatic effects. A quadratically added momentum spread contribution $\sigma_{err}$ to the measured size can be obtained from Eq. 2.41 by introducing to it a relative momentum spread $\delta p/p$ of the bunch:

$$\sigma_{err} = \sqrt{\frac{2}{3}} \left| \delta p/p \right| \left( \frac{L_d}{f_{av}} \right) \sigma_x, \tag{2.44}$$

where $L_d$ is the drift length between the quadrupole magnet and the screen, $f_{av}$ is the quadrupole magnet focal length for the mean momentum value, $\sigma_x$ is the beam size at the quadrupole magnet principal plane.

Several conclusions can be drawn concerning the quadrupole scan from this model:

- higher energy of the beam with the other parameters being constant results in smaller beam sizes at the screen;
- a smaller minimum beam size value is achieved for shorter distances between the quadrupole magnet and the screen;
- The size in the quadrupole principal plane can be controlled with the optics upstream of it, meaning that the minimum beam size is also proportional to its normalized emittance;
- the quadratically added chromaticity contribution to the beam size is proportional to the relative momentum spread.

### 2.3.3 Slit scan

A bunch phase space distribution can be reconstructed with the following approach. A slit is moved across the bunch. The slit cuts out a portion of the charge small enough that the space charge contribution to the divergence is negligible. After the slit the particles drift some distance $L_d$ and diverge

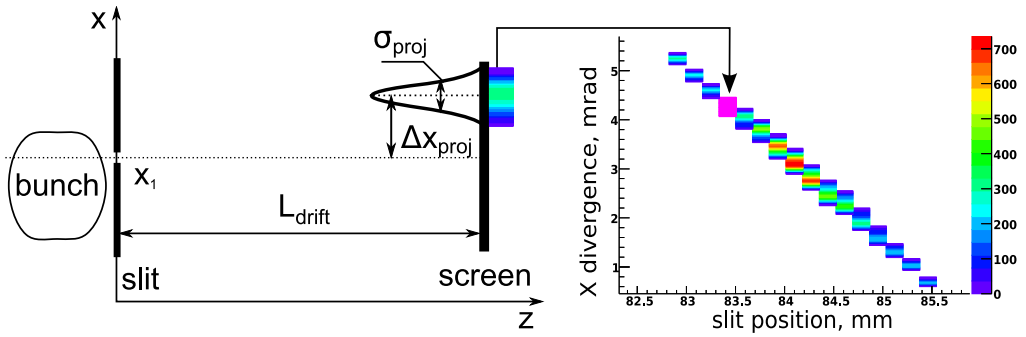


**Figure 2.11:** Slit scan procedure

to a distribution that is significantly larger than the slit opening. The obtained distribution represents a local divergence profile. By shifting the slit across the beam one obtains the divergence distributions for all transverse coordinates. The $x - x'$ correlation is obtained from the divergence distribution position on the observation screen. The phase space distribution is reconstructed by stacking all the distributions together in the trace space (Fig. 2.11).

The slit opening is chosen as a compromise between the space charge induced divergence change and the obtained image intensity. In the perpendicular transverse direction the slit is large enough to let the whole beam pass. The same pattern rotated by 90 degrees is used for the measurements of the beam emittance in the orthogonal transverse plane. The trace space distribution is obtained by scanning the slit position across the bunch. One can also combine many slits at the same beam mask. In this case it is a single shot measurement. The disadvantage is that the slit distances are fixed with the possibility of overlapping of the slit images. Later unfolding of the contribution of different slits requires to fit distributions to the measurement. This usually underestimates the real divergence. At PITZ a single slit scan is preferred because the full divergence distribution is directly measured. It allows to calculate the RMS size of the distribution, and not the size of the assumed distribution, but assumes pulse to pulse stability.

The following equation shows contributions to the beam size at the observation screen after a drift space of length $L_d$, calculated with the transport matrix represented in Eq. 2.29 for *k=0* and $\Delta z = L_d$

$$\sigma_x^2 = \sigma_{x0}^2 + 2L_d < x_0 x_0' > + L_d^2 \sigma_{x'0}^2. \tag{2.45}$$

On the observation screen the beam part that has passed through the slit mask forms a distribution with an RMS size $\sigma_x$. There are three contributions to this value depending on the beamlet properties: $\sigma_{x0}$ - RMS size defined by the slit size, $< x_0 x_0' >$ - position divergence correlation at the mask position, $\sigma_{x'0}$ - divergence. The slit size is kept small compared to the final size on the observation screen so one can neglect it. The second term contains the beamlet correlation that converges to zero at zero slit size. The last term is the divergence spread multiplied by the drift length squared. With a properly chosen drift length the third term strongly dominates in Eq. 2.45 and one can obtain the local divergence spread $\sigma_{x'0}$ from:

$$\sigma_{x'0}^2 = \frac{\sigma_x^2}{L_d^2}. \tag{2.46}$$

The narrow slit opening on Fig. 2.11 is along the x axis. $\Delta x_{proj}/L_d$ is a mean local divergence, while $\sigma_{proj}$ - the beam local divergence spread. To reconstruct the trace space distribution one has to put the projections on a 2D histogram at the coordinates $x_1,\ \Delta x_{proj}/L_d$.

# Chapter 3

# The Photo injector test facility in Zeuthen

The Photo Injector Test facility in Zeuthen (PITZ) is the DESY center for electron source characterization and optimization [8]. Since 2004 two electron guns from PITZ have been installed at FLASH (Free electron LASer in Hamburg) [37], DESY's running facility delivering high brilliance photon radiation down to 4.45 nm wavelength. PITZ is also developing the electron source for the European XFEL project [38]. The required transverse projected emittance value for 1 nC bunches in the injector is 0.9 mm mrad (100% of charge) [39], which was already demonstrated at PITZ [8, 40, 41].

## 3.1 Photo cathode laser system

PITZ requires a state-of-the-art laser system to be able to generate electron bunches with the required properties. The unique laser installed at PITZ [42] produces temporally shaped UV pulses with high repetition rate of 1 MHz. The pulses are organized into bunch trains at 10 Hz repetition rate, where each period can contain up to 800 laser pulses (Fig 3.1).

PITZ is a test facility and therefore the laser system here is also a prototype considered for the European XFEL. The basic part is a Yb:YAG infrared laser with multiple amplification stages and a pair of frequency doubling crystals to obtain UV output. The distinguishing feature of this laser is a temporal pulse shaper. Short oscillator pulses are stacked together to form a temporal flat-top shape with an FWHM duration of up to 22 ps, with rise and fall times of $\approx 2$ ps (Fig. 3.2). At the output the laser system can

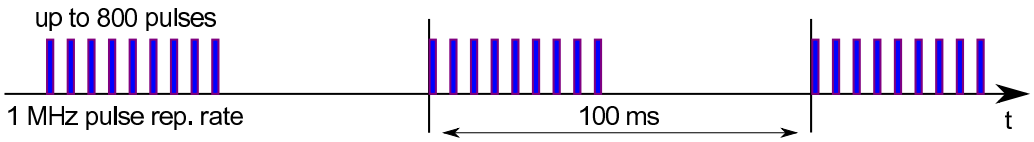


**Figure 3.1:** Time structure of the photo cathode laser pulses

deliver up to 10 $\mu$J per pulse. It is required to illuminate the cathode with up to 0.5 $\mu$J to produce 1 nC bunch charge considering a cathode quantum efficiency down to about 1%. The spot size at the cathode is controlled by a beam shaping aperture (BSA), which is imaged onto the cathode. The laser transverse intensity field in front of the aperture has a very wide gaussian shape, therefore allowing the part passing the opening to be rather homogeneous over the profile. At the BSA part of the laser energy is cut. The fine tuning of the laser energy on the cathode is done with an attenuator.

Because the laser is a critical component for the photo injector performance, stability of all laser parameters is monitored e.g. the transverse profile and intensity diagnostics of the laser beam is shown in Fig. 3.3. Some laser diagnostics is used in a parasitic mode to observe the parameters, other can be used only with the laser beam dumped in the diagnostics section. First of all one has to control the transverse and the longitudinal laser shape. For the transverse shape monitoring there are UV sensitive cameras on the laser table and in the gun neighborhood. There is exactly the same optical path to the cameras near the gun as to the cathode itself to ensure identical imaging. The laser transverse profile can be observed constantly using a quartz splitter and a subsidiary optics beamline. One more camera is situated at the end of another optics line that gets the light from a mirror. The mirror can be remotely moved in and out of the main optics line

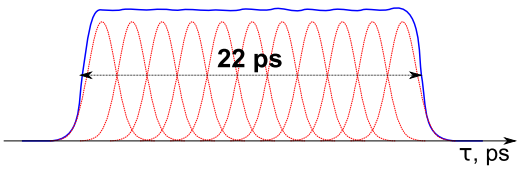


**Figure 3.2:** Typical flat-top temporal laser shape created by stacking short gaussian pulses.

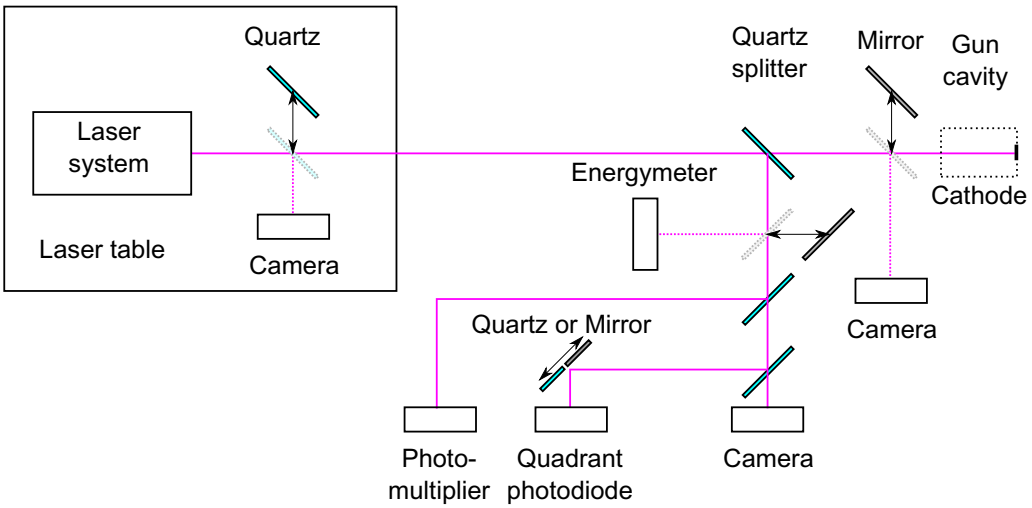


**Figure 3.3:** A scheme of the laser transverse profile and intensity diagnostics.

to the cathode. This allows to measure the beam profile with the smallest distortion.

It is a challenge to measure the longitudinal intensity distribution of picosecond light pulses, especially when they are in the UV range.

At PITZ there are two means of measuring the profile. Typically longitudinal pulse profiles are measured with an optical sampling system (OSS) which was developed as an integrated component of the laser [42]. This system uses a train of e.g. 550 pulses to sample the UV laser pulse longitudinal shape. It is done by a correlation method in a non-linear crystal where a shaped UV pulse meets an original short IR pulse of the oscillator and the difference frequency of both pulses is generated. The relative time between the pulses is scanned and the resulting intensity of the combined pulse of green light reconstructs the local UV pulse amplitude. It is assumed that all probing IR pulses and all sampled UV pulses have the same amplitude. The temporal resolution is about a picosecond (IR pulse duration). Disadvantage of the system is that the laser beam is fully utilized for the measurement and not available at the cathode during the measurement.

A streak camera can be used in parasitic mode for the laser longitudinal profile measurements at PITZ. It delivers a resolution of $\approx 3\,ps$ and is capable to measure the profile of a single pulse.

A standard CCD camera is not fast enough to record the profile of each pulse in the laser multipulse train mode. But the intensity and the pointing stability can still be monitored with 1 MHz. At PITZ a photomultiplier is used for the intensity measurements parallel to the injector operation. The same is true for a quadrant diode that is used to monitor the pointing stability of the laser at the cathode equivalent position. At PITZ the laser transverse shape drifts over time. For this reason a special measurement approach was developed to take the laser transverse profile into account for the quadrant diode measurements [43].

For more details about the laser diagnostics and the influences of the laser properties on the electron beam see [44].

| | |
|---|---|
| Wavelength | 257 nm |
| Temporal shape | flat-top |
| FWHM duration | 22 ps |
| rise and fall times | 2 ps |
| Transverse shape | flat-top |
| Transverse laser RMS spot size | 0.0-0.5 mm |
| Pulse repetition rate | 1 MHz |
| Max number of pulses in a train | 800 |
| Pulse energy | $\leq$10 $\mu$J |
| Train repetition rate | 10 Hz |

**Table 3.1:** Main laser system parameters.

## 3.2 RF gun

Fig. 3.4 shows the 3D model of the gun cavity and the solenoids. The PITZ RF gun is a normal conducting 1.6 cell L-band RF cavity (1.3 GHz). The body of the cavity is made of copper and the inner surface is dry ice cleaned. The dark current is less then 200 $\mu$A at the full power that corresponds to a peak accelerating gradient of 60 MV/m [45]. On the front side a coaxial coupler is placed to feed the power. The cathode is situated on the back side of the cavity and can be replaced with a special exchange system.

The solenoids are used for beam focusing and emittance compensation. The main solenoid creates a focusing field, the bucking compensates the field on the cathode.

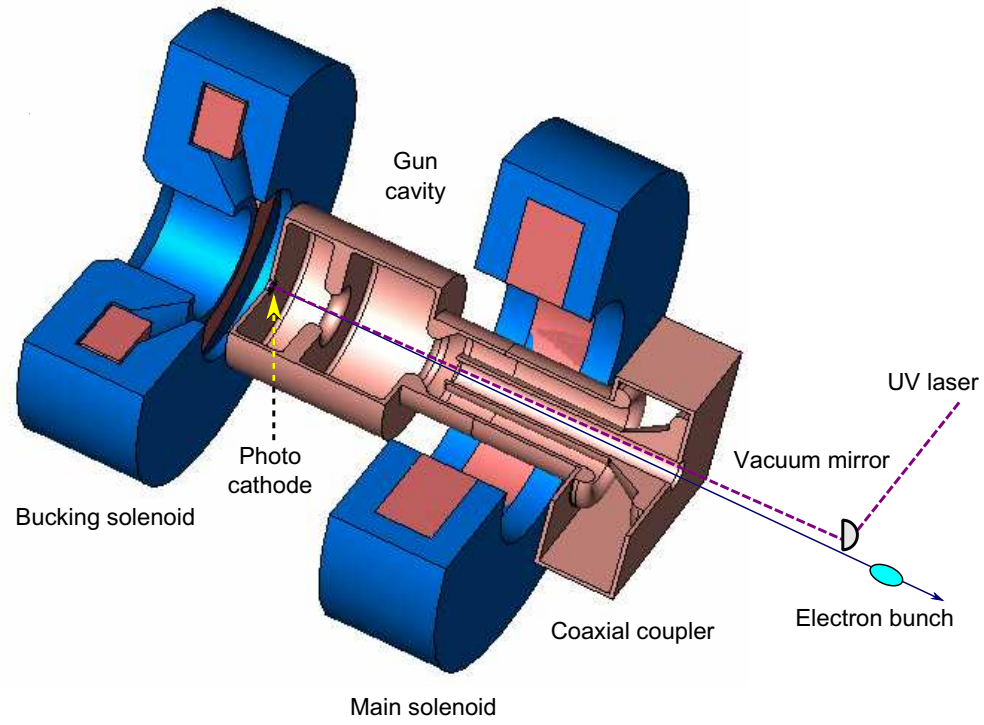


**Figure 3.4:** Electron gun cavity at PITZ

The RF system consists of a 10 MW Klystron and two waveguide lines which later are combined just in front of the coaxial gun cavity coupler. First the RF regulation was based upon two directional couplers in both RF waveguides in front of a T-combiner. This system had a poor phase stability. A unique 10 MW in-vacuum directional coupler together with a new LLRF system was installed at PITZ in 2010 and showed significantly higher efficiency of the feedback regulation and therefore better parameter stability. The new coupler is placed between the T-combiner and the coaxial coupler of the gun. It allows to measure the forward and reflected power directly at the gun input.

The gun cavity has a regulated water cooling system that keeps the cavity in resonance at up to 50 kW average power dissipated in the gun walls. The required temperature stability is $< 0.01\,C^{\circ}$ RMS which is not yet fully reached. The cavity has experimentally shown operation with a peak gradient of 60 MV/m at 700 $\mu$s RF pulse duration.

With booster cavity

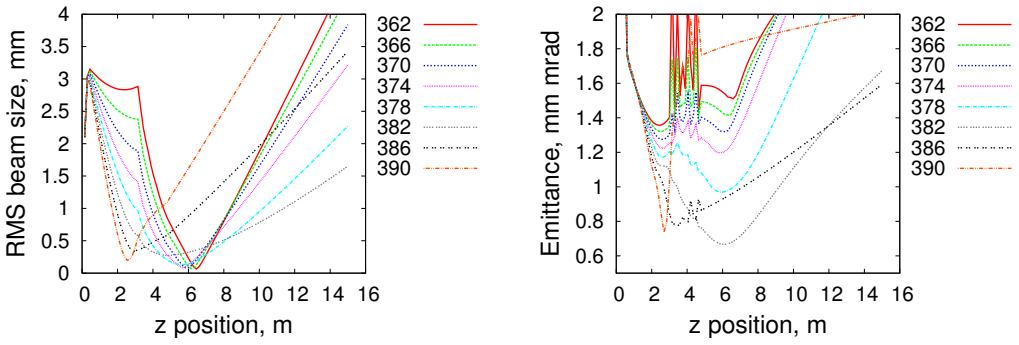


(a)




(b)

Without booster cavity

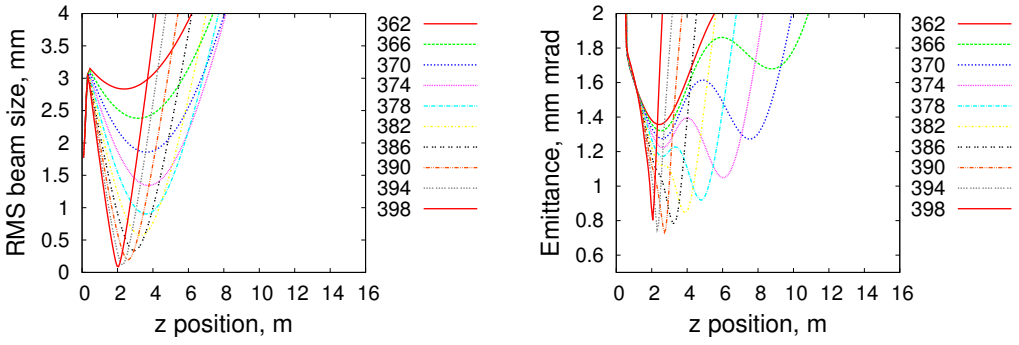


(c)




(d)

**Figure 3.5:** Beam size and emittance versus position from the cathode for different solenoid currents for the optimized PITZ setup (ASTRA simulation: charge 1 nC, flat-top laser profile with rise/FWHM/fall times of 2, 21, 2 ps respectively, transverse RMS laser spot size at the cathode 0.39 mm) are shown in the upper plots. Lower plots represent results for the setup without the booster cavity.

## 3.3 Booster cavity

The beam energy reaches about 6.7 MeV in the gun. Fig. 3.5 shows the beam size and emittance development along the beampipe for the setup with and without the booster module for 1 nC bunch charge. The beam $5\sigma$ size should not exceed the beampipe diameter of $\sim$40 mm. The beam size is kept within

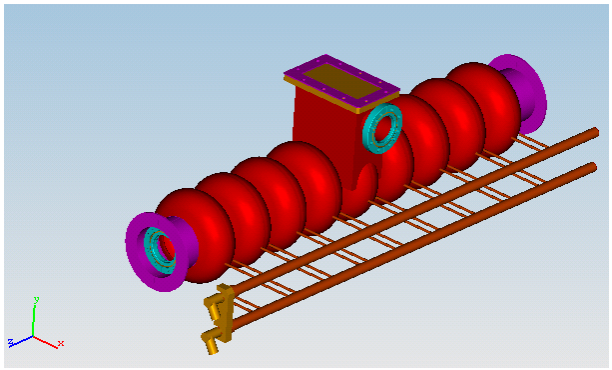

**Figure 3.6:** 3D model of the TESLA cavity at PITZ

that limit for longer distances at different solenoid currents due to a focusing effect and reduction of particles divergence by the longitudinal acceleration. It is important also that the space charge forces decrease as $1/\gamma^2$. The emittance minima are wider along the z axis, therefore measurement elements positioning accuracy requirements are more relaxed.

The PITZ setup contains diagnostics along a 20 m long beampipe. As it can be seen from the figure the beam size explodes and the usable setup length can be rather short if no further acceleration or focusing is applied after the gun. With presence of a second accelerating module it is also possible to generate energy-chirped bunches. The last possibility is extensively used for the slice emittance measurements described in this work.

In the slice emittance measurement process two different booster cavities were involved. The setup was designed for a cut disk structure (CDS) booster, but the full commissioning process was performed with a TESLA type booster. Information about both of the cavities is given below.

### 3.3.1 TESLA

The FLASH accelerator is based upon TESLA type cavities. These are 1.3 GHz superconducting niobium cavities. The same geometry was taken as a basis for the first energy boosting cavity that was installed at PITZ [46], but which was produced out of copper. The cavity has 9 cells, is 1115 mm long, and can reach a peak gradient of about 14 MeV/m for an RF period of up to 50 $\mu s$ restricted by the poor water cooling capabilities of this cavity. The beam energy reached 14.6 MeV after the booster at the RF pulse length.

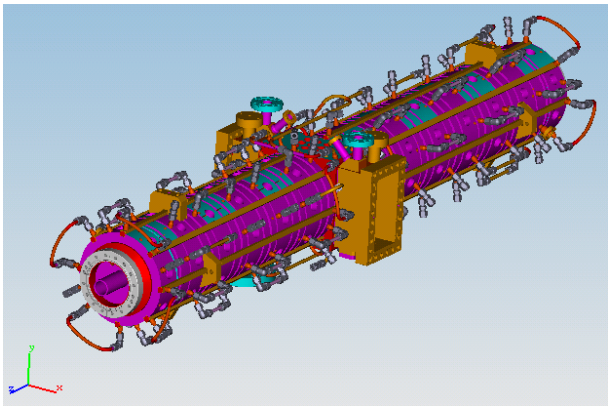

**Figure 3.7:** 3D model of the CDS cavity at PITZ

The cavity has only one RF power input through a slot in the middle cell. This asymmetry produces a dipole field mode in the cavity.

### 3.3.2 CDS

The CDS booster [47] is the successor of the TESLA type booster. The main upgrade is in the cooling system efficiency that allows now to run with the maximum power over the full RF pulse length of 800 $\mu$s. The length of the cavity is about 1.5 m. Among other advantages are a higher accelerating gradient, integrated field probes, which allow direct measurement of the field profile, better stability that can be even more improved via regulation based on the field probes, and symmetric power input ports, which cancel out the dipole mode of the perturbation field. The maximum beam energy reached on the output is $\approx$25 MeV.

## 3.4 Diagnostics

A schematic of the PITZ diagnostics is shown in Fig. 3.8. The scheme can be divided into two main parts: a low energy section before the CDS booster cavity (beam energy up to 6.7 MeV), and the rest of diagnostics in the high energy section (beam energy up to 25 MeV).

The low energy section starts with the gun itself and the main and bucking solenoids around it. There is a screen station next to the gun and the

solenoids that also contains a Faraday cup. Then a spectrometer for the beam momentum distribution measurements follows. Two further screen stations are placed between the spectrometer magnet and the booster input. All together there are four screen stations installed in the low energy section, two of them possess Cherenkov radiators with streak camera readouts for the bunch length and the longitudinal phase space measurements. There are three beam position monitors (BPM), an integral current transformer (ICT), and six beam trajectory correcting dipole magnets (steerers).

The high energy section starts with a BPM, two steerers, a quadrupole doublet, and an ICT. The first emittance measurement system (EMSY1) is situated next after the ICT. More details are available in the next section. A screen station with a streak readout follows EMSY1. There are a BPM, a pair of quadrupole magnets that forms a quadrupole doublet and a steerer between the EMSY1 and EMSY2. The second emittance measurement system is similar to the first. Downstream from EMSY2 there is a 180 degrees dipole, that is used as a high energy spectrometer and also for the slice emittance measurements with an energy chirped beam. Following the beam orbit downstream the straight section one sees a steerer, a couple of screens stations with an ICT in between, and a wire scanner. Next to it one sees a steerer, a quadrupole doublet, many quadrupole magnets and screens which form a matching section and following it a tomography module. At the end of the beam line there are several diagnostics components: a wire scanner, EMSY3, a spectrometer dipole, a screen station, a BPM, an ICT and a beam dump. In the high energy dispersive section after the 180 degrees dipole there is a slit cutting the beam in dispersion direction, a quadrupole magnet, a screen station with the streak readout, another screen station and a beam dump.

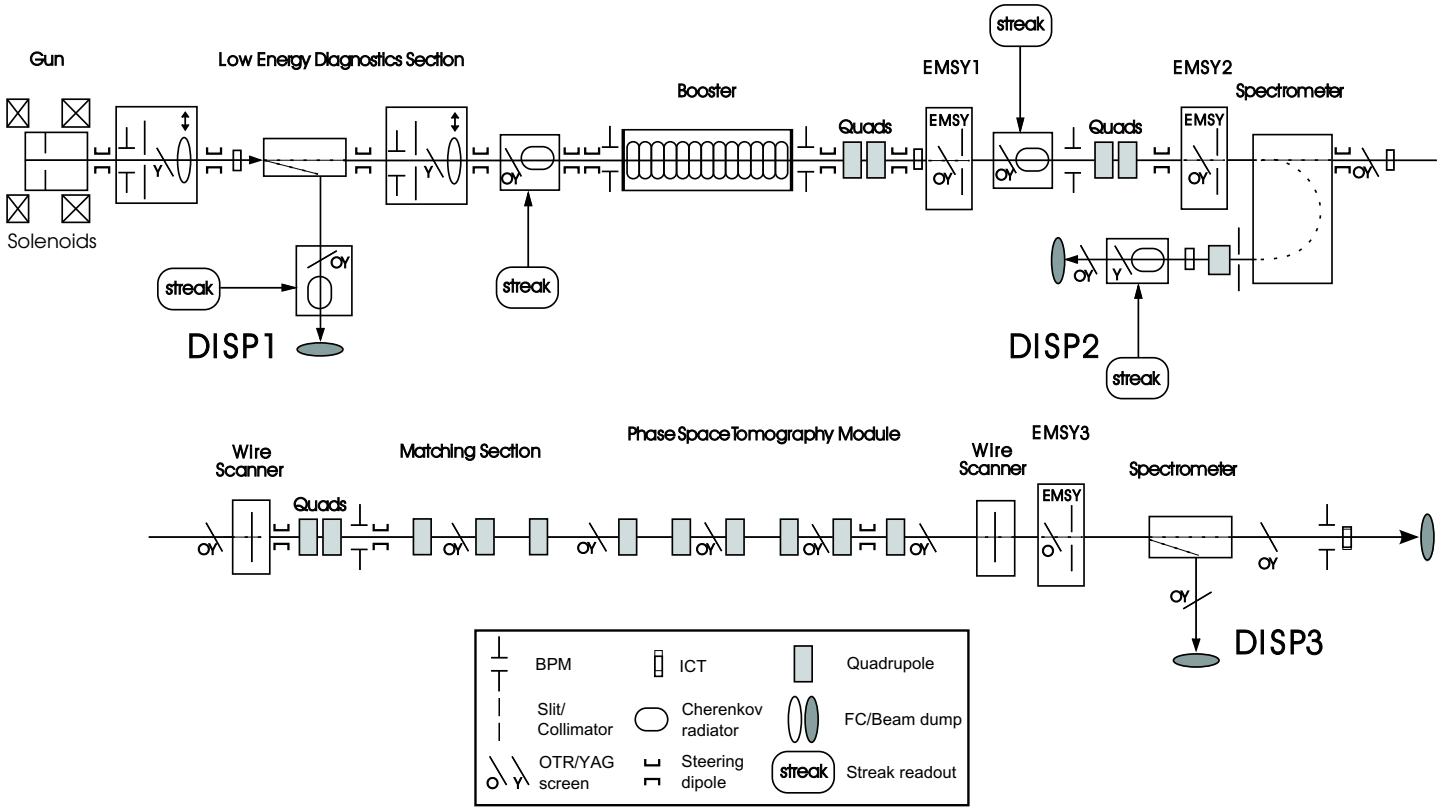


**Figure 3.8:** PITZ test beamline used for the slice emittance investigations

### 3.4.1 EMSY

The Emittance Measurement SYstem (EMSY) was originally the first hardware dedicated for emittance characterization at PITZ [48]. The device is based on the slit scan measurement method of projected emittance (see section 2.3.3). At the position of EMSY two perpendicular actuators and the beamline form an orthogonal system (Fig. 3.9). Each actuator is carrying the slit masks with slit widths of 10 $\mu$m and 50 $\mu$m. The small opening of the slit masks is in the actuator movement direction. The slit that moves horizontally is used for the horizontal (X) beam emittance measurements and analogously for the vertical actuator. Additionally each actuator has a screen (a YAG powder screen or an OTR screen). The EMSY station has also two rotational stages to optimize the charge transmission through the slits.

PITZ has three EMSYs along the beam line after the booster. EMSY2 is involved in the slice emittance measurements and the measurement setup is shown and discussed in details in section 4.1.

### 3.4.2 The first high energy dispersive arm (HEDA1)

The first energy dispersive section of the high energy part was designed as a multi-purpose system. The equipment allows measuring the momentum spectrum with a high resolution, as well as longitudinal phase space measurements and slice emittance measurements using an energy-chirped beam. The list of the diagnostics line components consists of a vertical position filtering slit, a quadrupole and two screen stations with the first of these having a streak camera read-out. All details about the slice emittance measurements with the dipole can be found in section 4.1. Here a short introduction is given only.

#### 3.4.2.1 The dipole

The 180 degrees dipole [49] is used as a dispersive element with a reference trajectory radius $R = 300\,mm$. The dispersion D is 600 mm and is constant along the beamline after the dipole exit. A 2.7 meter long diagnostics beamline of the dispersive section is compactly situated right under the main beamline. Another advantage of this geometry is that the integrated magnetic field experienced by the particles does not depend on the transverse

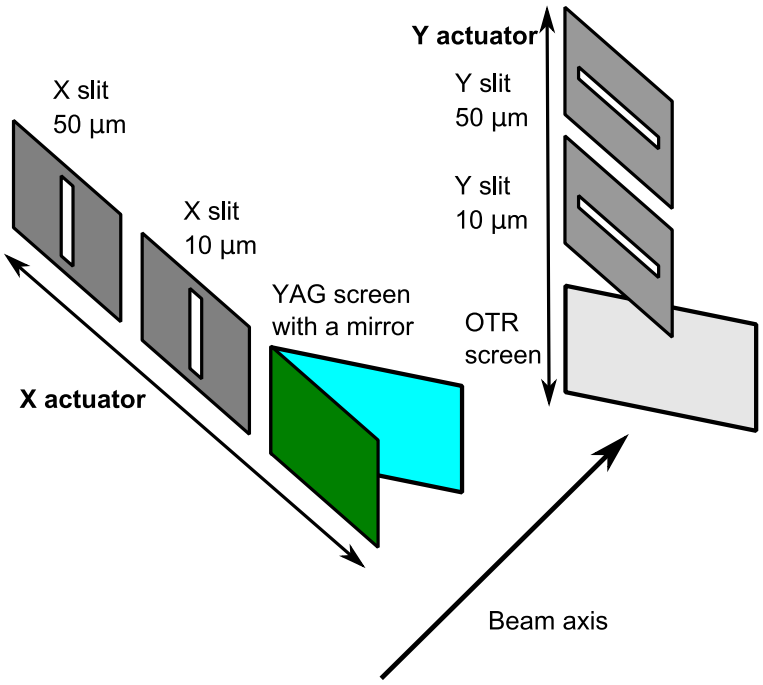


**Figure 3.9:** A sketch of EMSY1 and similarly built EMSY2 actuators in the vacuum vessel: on the horizontal actuator there are a YAG screen positioned orthogonally with respect to the beam axis and a 45 degree mirror, and two slits with a small opening in X; on the vertical actuator there are a 45 degree OTR screen and slits with a small opening in Y. EMSY3 has multislit masks on both actuators instead of the 50 $\mu$m single slit masks.

entrance point within the input beampipe size. More information is given in section 4.1.

#### 3.4.2.2 The momentum filtering slit

A momentum filtering slit is used to cut out a small part of the beam which is spread out laterally by the dipole, thereby selecting a part of the momentum spectrum. The slit has a 5 mm opening in dispersive direction. The slit width is a compromise between the setup resolution and the resolution constancy over a range of solenoid currents. The slit is situated 20 cm downstream from the exit of the dipole.

**Table 3.2**

| Parameter | H1Q3 | D2Q2 |
|---|---|---|
| Bore diameter, mm | 40 | 80 |
| Effective length, mm | 43 | 226 |
| Max. current, A | 12 | 16.6 |
| Max. gradient, T/m | 8 | 2 |

#### 3.4.2.3 Quadrupole magnet

The parameters of the quadrupole magnets, involved in the slice emittance measurements at PITZ, can be found in Table 3.2. H1Q3 is the quadrupole in front of the dipole and D2Q1 corresponds to the magnet in the 180 degrees dipole dispersive section. The magnets calibration results are given in Appendix B.1.

#### 3.4.2.4 Screen stations

In the second dispersive section there are two screen stations: Disp2.Scr1 and Disp2.Scr2. Both are equipped with big YAG:Ce powder screens and OTR screens (an aluminum foil). The YAG screen dimensions are 80 mm by 60 mm and they are positioned with an angle of 45 degrees relative to the beam axis. The OTR screens are 60 mm by 60 mm and are also 45 degrees tilted with respect to the beam direction.

The first screen station possesses a streak camera read-out for longitudinal phase space measurements. It consists of an aerogel Cherenkov radiator and a light transport system (optics line length of 20-25 m) to the streak camera. For more details see [50].

### 3.4.3 Longitudinal beam diagnostics

The longitudinal phase space diagnostics is based on aerogel Cherenkov radiators and a streak camera [51]. The longitudinal phase space measurement can be done in two dispersive sections - in the low energy dispersive section downstream the gun, and in HEDA1. The streak camera [52] sweeps the temporal profile perpendicular to the dispersion direction. 2D images from the camera represent the longitudinal phase space. The topic is described in detail in [50].

### 3.4.4 Tomography module

The transverse phase space tomography module was installed in 2010 and is successfully in use at PITZ since 2011 [36]. The basic structure includes four screen stations and the quadrupole magnets in between placed periodically. The quadrupole magnets are set to get a phase advance of 45 degrees between the screen stations. The advantage of the tomography is the simultaneous measurement of the emittance in both planes, and reconstruction of the phase space distribution.

### 3.4.5 Future diagnostics upgrade at PITZ

PITZ has recently upgraded to the next stage that includes a deflecting cavity and a new multi-purpose high energy dispersive arm (HEDA2).

#### 3.4.5.1 Deflecting cavity

With the help of the deflecting cavity which will be installed upstream of the tomography module several diagnostics can be applied to perform measurements on a temporal fraction of a bunch. These are emittance and momentum spread diagnostics that will turn into slice emittance and slice momentum spread. The cavity itself is a 3 GHz RF cavity with vertical deflection that will provide time resolution down to 200 fs [53].

#### 3.4.5.2 Second high energy dispersive arm (HEDA2)

A third spectrometer will be placed at the end of the setup [54]. The main purposes include the momentum distribution measurements, especially for sets of pulses chosen out of long pulse trains with a help of a kicker magnet, and high resolution slice momentum spread measurements together with the deflecting cavity. The radiation safety requires that the full electron bunch train can only be stopped in a specially designed and shielded beam dump. For this reason the main part of the charge has to be returned to the main beam dump after the dispersive section. HEDA2 is composed of three dipole magnets. The first is the spectrometer dipole, the other two bring the beam back to the straight section in front of the dump (Fig. 3.10).

The beam is deflected with the first dipole from the straight beam line in the horizontal plane (X plane). This part of the dispersive section contains an off-axis screen for the momentum measurements. Because of high energy

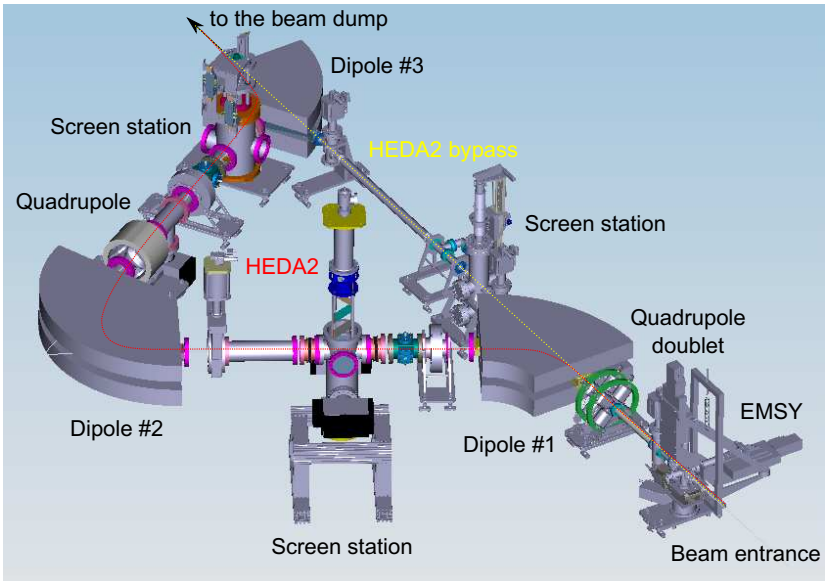


**Figure 3.10:** 3D drawing of the second dispersive section setup

deposition and radiation production one can not direct all the pulses from a full bunch train at up to 800 $\mu$s length to the screen. Instead there is a kicker in front of the dipole in the straight section that produces a vertical kick of 5 mrad. The kicker is fast enough to separate any single pulse from the train. The kicked fraction of the pulse train is deflected towards the screen. The remaining bunches will follow a reference orbit through the second and the third dipole. After that the beam gets back in the straight section and enters the beam dump.

Combining the spectrometer with the deflecting cavity will allow slice momentum spread measurements with a resolution down to 1 keV/c [54]. The deflection is going to be applied in vertical direction, therefore the dispersive section is designed to bend the beam in the horizontal plane. The detailed longitudinal phase space pictures can be obtained at the first screen in the dispersive section: the beam spectrum appears along the horizontal axis, the time along the vertical axis.

In the return path between the second and the third dipoles HEDA2 contains another screen station. With the introduction of a quadrupole between the second and third dipoles it becomes possible to measure the vertical transverse slice emittance at the second screen (in HEDA1 the horizontal transverse slice emittance is measured). There is an EMSY in front of

the first dipole that can be used for comparable transverse emittance measurements using the slit scan technique. The main design parameter was to have a dispersion of 600 mm at the analysis screen as for HEDA1. The momentum filtering slit is included in the first screen station.

# Chapter 4

# Slice emittance measurements using an energy-chirped beam at PITZ

## 4.1 Slice emittance measurement method using an energy-chirped beam

High-gain free electron laser output power is proportional to the bunch current squared [55] and therefore the bunch compression stage is introduced to boost up the peak current. For the multi stage High-Gain-Harmonic Generation (HGHG) scheme of the BESSY FEL one requires longitudinally flat-top shaped electron bunches passing a sequence of radiation undulators, meaning that compression is aimed to boost the current up but keeping the shape generated in the injector (PITZ gun was considered as a source) [56]. The radiating part of the bunch is much shorter than the full length. This allows every next radiation stage to utilize a different "fresh" longitudinal part of the bunch. In this scheme the slice emittance after the compression stays relevant to the situation after the gun.

Fig. 4.1 demonstrates how an initial gaussian electron bunch with FWHM of about 10 ps (solid line indicates the current profile) is squeezed to a 100 fs spike and a much longer tail at FLASH [57]. The bunch transverse emittance (dotted line) has a longitudinal structure after the gun as well as after the bunch compressor. When one investigates the transverse emittance influence on SASE FEL radiation output power only the current spike

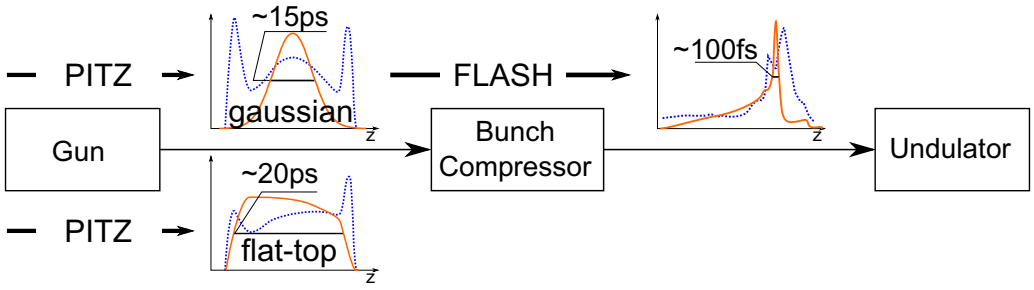


**Figure 4.1:** Schematics shows the electron bunch longitudinal current (orange solid line) and emittance (blue dotted line) profiles after the gun and after the bunch compressor. The upper line of the plots corresponds to a gaussian temporal profile of the cathode laser in the photo injector (current setup at FLASH). The bunch profiles after the gun were simulated using ASTRA, the profiles after the bunch compressor are taken from [58]. The lower plot after the gun shows simulated profiles for a flat-top temporal profile of the laser at the cathode.

charge transverse emittance plays a significant role [55]. A slice emittance diagnostics was integrated into the FLASH setup [58] to study cases under different accelerator conditions. The situation cardinally changed with the installation of a third harmonic cavity to linearize the longitudinal phase space before the bunch compression stage [59]. In this scenario higher peak currents can be achieved and the longitudinal structure of the bunch with its properties, like transverse emittance, should be better conserved in the compression process.

In case of the European XFEL [39] the bunch transverse emittance after the photo injector is already larger than the contribution of the transport downstream to the undulator including compression stage, and therefore the beam studies have to concentrate on the control and minimization of the transverse emittance directly at the injector.

The PITZ facility has exactly the aim to optimize beam conditions to obtain the minimum transverse projected emittance. Projected emittance value is an upper limit of the transverse emittance contribution, because as one experiences from the setup simulations transverse emittance has a longitudinal structure (lower left plot in Fig. 4.1). Applying a slice emittance diagnostics already at the injector can help to take a closer look at the projected emittance compensation process as well as to obtain the transverse emittance structure along the bunch with a certain resolution.

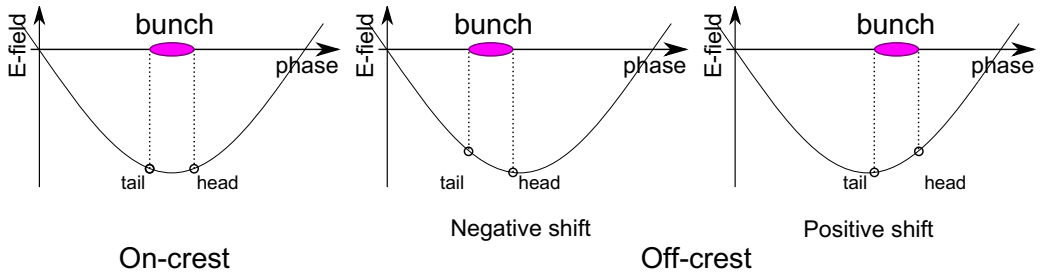


**Figure 4.2:** A sketch explaining the phase relation between a bunch and the booster cavity accelerating field: on-crest corresponds to the maximum mean momentum gain; a negative shift of the field phase results in the bunch head getting higher momentum than the tail; in case of a positive phase shift the tail gets more energy than the head.

Measuring slice emittance enables to analyse the emittance of the particles within a well defined temporal window shorter than the bunch length. It is like cutting the bunch into longitudinal slices (parts) and measuring the emittance of each slice separately. This work is devoted to an implementation of the slice emittance measurement technique downstream the RF gun cavity at PITZ. The method uses an energy chirped beam and a dipole [60].

The slice emittance measurement can be divided into two processes that can overlap in time or follow one after the other:

- separate a fraction of the bunch (a longitudinal slice),
- measure the emittance.

Splitting a portion of the bunch charge that corresponds to a longitudinal slice proceeds in the following way. The longitudinal momentum of the particles is correlated to the longitudinal position within the bunch. This correlation is introduced via an off-crest acceleration in the booster cavity (Fig. 4.2).

With this correlation the longitudinal distribution of the bunch can be turned into a transverse one inside a dipole magnet. After the dipole a momentum range is cut out with a slit that corresponds to a longitudinal slice of the bunch. After that the slice transverse size or the slice beamlet (in slit scans) is measured on a screen downstream. The data is used to obtain the bunch emittance.

Most of the slice emittance diagnostics have this in common: the bunch longitudinal distribution is converted into a transverse one first. Hence only

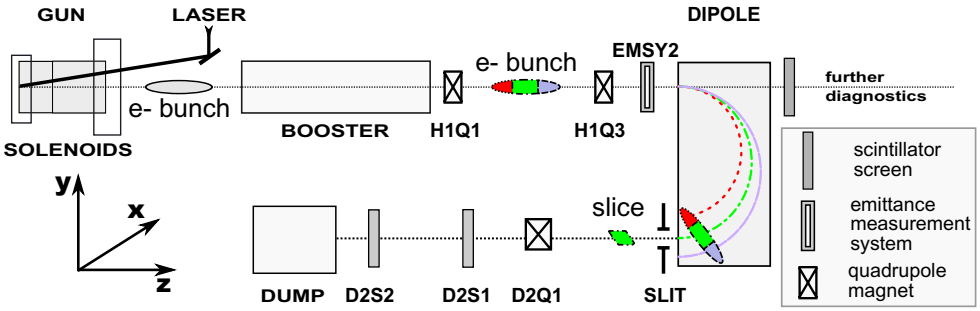


**Figure 4.3:** Simplified schematic of the PITZ slice measurement setup using an energy chirped beam after the dipole.

one transverse component of the slice emittance can be studied at the same time.

At PITZ the slice emittance setup is based upon an offcrest acceleration in the booster cavity, the 180 degrees dipole (HEDA1), which turns the longitudinal distribution into a transverse one, EMSY2 and two quadrupole magnets for the emittance measurements (Fig. 4.3). The dispersion occurs in the dipole along the vertical Y axis and the horizontal X emittance component is measured.

The measurement starts from setting up the electron injector. The cathode laser temporal and transverse shapes are chosen and fixed. The bunch momentum versus gun phase needs to be characterized first and the phase for the measurement adjusted. At this phase the charge is set to a required value by means of the photo cathode laser intensity. The phase of beam maximum momentum gain (on-crest phase) of the booster is found. At this point an off-crest phase is set. There are several considerations one has to take into account when choosing an off-crest phase value for the slice emittance measurement. For diagnostics purposes negative (the minimum momentum spread phase has a positive phase offset) phase offsets are used in general. In this way the bunch head gets more energy gain than the tail. An opposite phase offset leads to bunch compression and only then to an expansion. Anyhow slice emittance measurements are also possible in this mode. A stronger off-crest mode introduces larger momentum spread with a lower mean momentum (Fig. 4.4). The off-crest phase is chosen to optimize the time resolution (see section 4.3). A counterargument for going too much off-crest is a wider momentum spread that is reducing the individual slice intensity and introducing broader energy spread within a slice. Running at

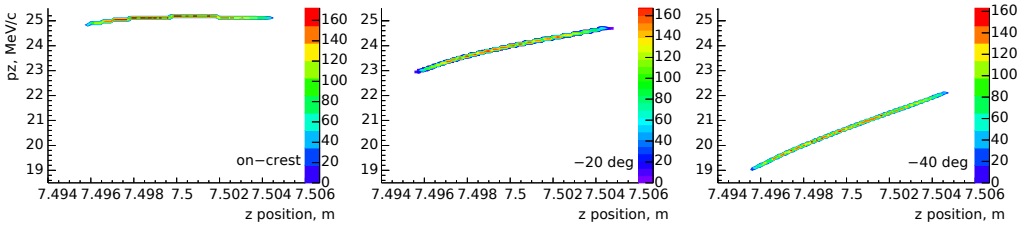


**Figure 4.4:** The simulated beam longitudinal phase spaces for a set of booster phases. The evaluation is done for a 1 nC bunch, 20 ps FWHM long laser pulse at the cathode, rise and fall times are 2 ps.

off-crest phases is not the standard regime of operation, still the minimum slice emittance does not change significantly according to simulations with the space charge tracking using ASTRA [61] (Fig. 4.5). All the simulations in this thesis assume the solenoid calibration given in Appendix A.1.

The dipole turns the energy-chirped bunch momentum distribution into a transverse one. A slit at the dipole output separates a portion of the bunch charge that corresponds to a certain momentum range and therefore a specific longitudinal slice. The momentum calibration of the slit with the dipole current is done for a reference trajectory, when a particle enters the dipole on axis with zero angle with respect to it. If the trajectory is different one needs to introduce a correction that can be derived using the

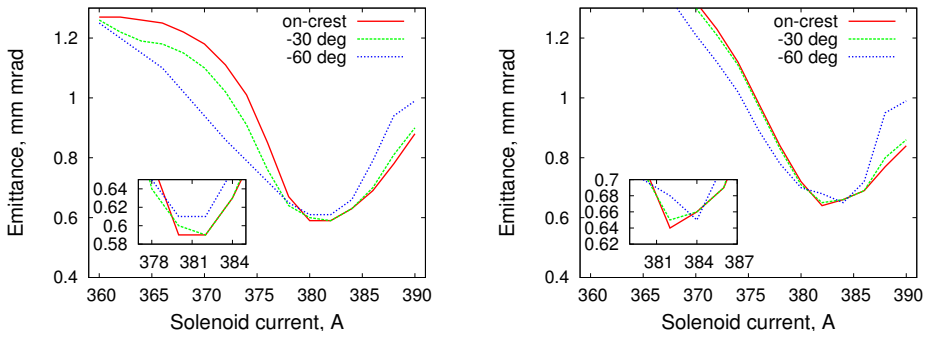


(a): av (b): pc

**Figure 4.5:** Slice emittance solenoid scan with different booster off-crest phases. (a) Average slice emittance. (b) Emittance of the peak current slice.

dipole transfer matrix from [14] (vertical deflection):

$$\begin{pmatrix} x \\ x' \\ y \\ y' \\ \frac{\delta p}{p} \end{pmatrix} = \begin{pmatrix} 1 & s & 0 & 0 & 0 \\ 0 & 1 & 0 & 0 & 0 \\ 0 & 0 & \cos\left(\frac{s}{R}\right) & R\sin\left(\frac{s}{R}\right) & R(1-\cos\left(\frac{s}{R}\right)) \\ 0 & 0 & -\frac{1}{R}\sin\left(\frac{s}{R}\right) & \cos\left(\frac{s}{R}\right) & \sin\left(\frac{s}{R}\right) \\ 0 & 0 & 0 & 0 & 1 \end{pmatrix} \begin{pmatrix} x \\ x' \\ y \\ y' \\ \frac{\delta p}{p_0} \end{pmatrix}_e , \quad (4.1)$$

where $R$ - the designed trajectory radius, $s$ - the trajectory arc length, the index 'e' denotes the entrance parameters of the particle.

The particle momentum is defined by the $y$ position at the slit. There is a drift $L$ between the dipole exit and the slit. Multiplying the matrices and applying the 180° rotation angle of HEDA1 dipole $s/R = \pi$ one gets

$$\begin{pmatrix} x \\ x' \\ y \\ y' \\ \frac{\delta p}{p} \end{pmatrix} = \begin{pmatrix} 1 & s+L & 0 & 0 & 0 \\ 0 & 1 & 0 & 0 & 0 \\ 0 & 0 & -1 & -L & 2R \\ 0 & 0 & 0 & -1 & 0 \\ 0 & 0 & 0 & 0 & 1 \end{pmatrix} \begin{pmatrix} x \\ x' \\ y \\ y' \\ \frac{\delta p}{p_0} \end{pmatrix}_e . \quad (4.2)$$

The vertical axis does not change its direction after the bend. A particle with $p = p_0$ has

$$\Delta y = y_e + L y'_e, \quad (4.3)$$

where now $\Delta y$ can be used as a correction for the beam position and divergence at the dipole's entrance. In real life we deal with bunches of particles and the reference screen cannot always be put into perfect position, and there is no possibility to set a screen exactly at the dipole entrance. Lets assume two screens around the dipole in the straight section. There is no steering applied in between the screens. The dipole entrance is $L_1$ away from the first screen, the screen-to-screen distance is $L_2$. L is, as before, the drift length from the exit of the dipole to the slit. The beam center positions on the screens then are $y_1,\ y_2$. Assuming straight trajectories of the particles we obtain:

$$y'_e = \frac{y_2 - y_1}{L_2}, \quad (4.4)$$

$$y_e = (y_1 + y'_e \cdot L_1). \quad (4.5)$$

Now we can obtain the correction from Eq. 4.3 in terms of the measured positions and known distances:

$$\Delta y = y_1 + \frac{y_2 - y_1}{L_2} \cdot (L_1 + L). \quad (4.6)$$

The beam vertical position after the slit has to be corrected by subtracting the value from Eq. 4.6 before it is recalibrated into momentum.

The field flatness of the dipole is better than 1/1000 over trajectories within a range $\pm 40\,mm$ around the reference trajectory ($R = 300\,mm$) [62]. Therefore a simple proportion can be used to estimate the transverse distribution size at the dipole exit:

$$y_{RMS} = \frac{p_{RMS}}{\overline{p}} 2R. \tag{4.7}$$

The momentum RMS spread reaches e.g. 7 percent of the mean momentum value with -60 degree in the booster. That corresponds to a transverse RMS size of 42 mm at the dipole exit.

There are two approaches available to measure emittance with this setup: the slit scan technique with the slit mask in front of the dipole, and the quadrupole scan method using the quadrupole magnet in the dispersive section or the quadrupole in front of the dipole. Fig. 4.6 shows equivalent straight distances for each case of the measurement.

Both procedures are repeated for each slice that is chosen by setting a certain dipole current. The inner scan procedure changes the EMSY slit position or the quad current and saves the profiles from the screen.

**Slit scan with EMSY2.** EMSY2 is situated about 1.5 m downstream from EMSY1 (nominal location for projected emittance measurements) right in front of the dipole. The horizontal slit mask position is scanned along the X axis. The portion of charge that passes the slit has strongly reduced transverse space charge interaction along X. Due to a significant difference in the trajectory length of the particles within the dipole the bunch length is additionally stretched, and hence the space charge becomes relaxed even more.

Scanning in a wide range of beam RMS divergences (i.e. wide range of gun solenoid currents) requires a certain horizontal field of view at the observation screen. For the optimum operation with 1 nC one needs to expect X RMS beam sizes at the screen up to 3 mm at the Disp2.Scr2 position for a solenoid current of 390 A (Fig. 3.5a assuming about 9.7 m equivalent position of the screen). On the other hand resolution has to be taken into account. The slit mask projection to the screen at the solenoid current 390 A has an average RMS horizontal size of down to 100 $\mu$m. The largest beamlet size is obtained for the beam size focus on the slit mask. Based on an interplay of

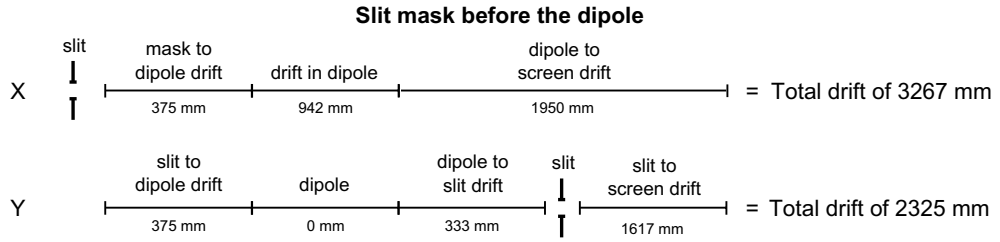


(a): EMSY2

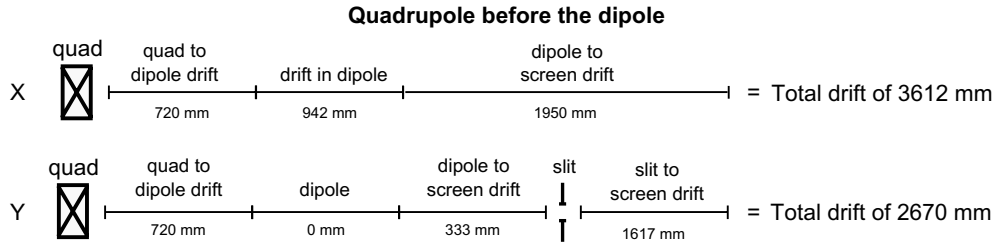


(b): H1Q3

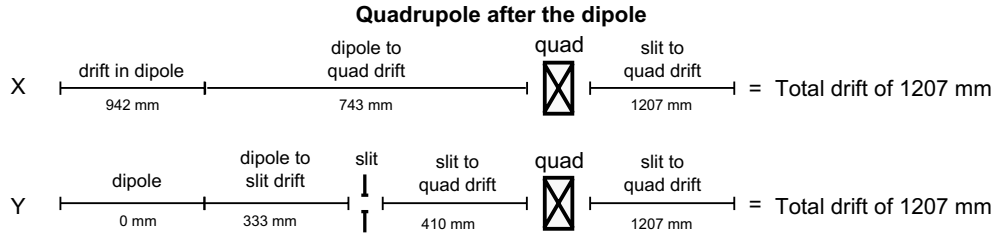


(c): D2Q1

**Figure 4.6:** Equivalent straight beamlines representation for emittance measurement using: (a) EMSY in front of the dipole; (b) the quadrupole in front of the dipole; (c) the quadrupole after the dipole (the 180° dipole is treated as a drift space for X transverse dynamics).

these effects one has to choose a magnification that allows to capture a wide enough view angle in horizontal plane and still resolves an expected beam size of about a hundred micrometers.

The slit imaged by the beam onto the observation screen moves with the mask. The beamlet position shift on the screen $\Delta x_{beamlet}$ with the slit step from a position $x_1$ with a local average divergence $x'_1$ to $x_2$ with a divergence $x'_2$ is defined as

$$\Delta x_{beamlet} = x_2 - x_1 + (x'_2 - x'_1) * L_{drift}, \tag{4.8}$$

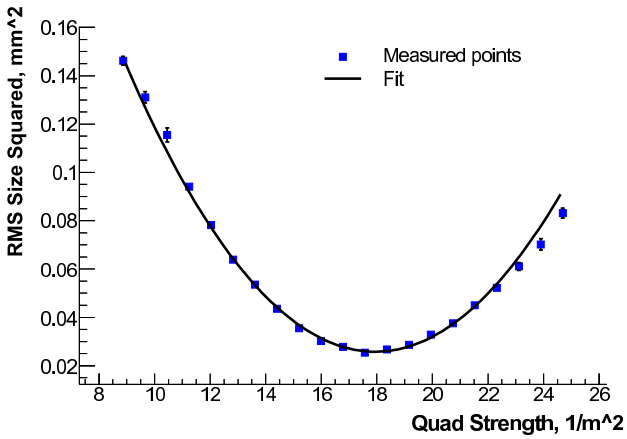


**Figure 4.7:** A measurement example with a post-processing fit.

where the last term represents the correlated divergence and can be both positive and negative.

**Emittance scan using a quadrupole before the dipole.** A quadrupole doublet is located in the straight section about a meter upstream from the dipole and one can measure slice emittance using a single quadrupole from the doublet.

For quadrupole scan measurements emittance value is obtained by fitting the beam size as a function of the quadrupole strength. The squared beam size dependence on the quadrupole strength $k$ is a parabola like function (Fig. 4.7) that is fitted using three RMS beam parameters $\sigma_x^2$, $< xx' >$, $\sigma_{x'}^2$ which define an equivalent RMS ellipse. In general the fitting problem is formulated below using transport matrices of the quadrupole and of the drift space to the screen and a fitting parameter vector $\{\sigma_{x0}^2, < xx' >_0, \sigma_{x'0}^2\}$:

$$\begin{pmatrix} \sigma_{x1}^2 \\ \sigma_{x2}^2 \\ \sigma_{x3}^2 \\ \dots \end{pmatrix} = \begin{pmatrix} A_1 & B_1 & C_1 \\ A_2 & B_2 & C_2 \\ A_3 & B_3 & C_3 \\ \dots & \dots & \dots \end{pmatrix} \begin{pmatrix} \sigma_{x0}^2 \\ < xx' >_0 \\ \sigma_{x'0}^2 \end{pmatrix}, \tag{4.9}$$

where the matrix elements are according to the description in section 2.3.2:

$$A_i = \cos^2\phi_i - 2\sqrt{K_i}L_d \sin\phi_i \cos\phi_i + L_d^2 K_i \sin^2\phi_i, \tag{4.10}$$

$$B_i = (\tfrac{2}{\sqrt{K_i}} - 2L_d^2\sqrt{K_i}) \cos\phi_i \sin\phi_i + 2L_d(\cos^2\phi_i - \sin^2\phi_i), \tag{4.11}$$

$$C_i = \tfrac{1}{K_i} \sin^2\phi_i + \tfrac{2L_d}{\sqrt{K_i}} \cos\phi_i \sin\phi_i + L_d^2 \cos^2\phi_i \tag{4.12}$$

with $\phi_i = \sqrt{K_i} \cdot l_{quad}$, $\mathrm{K_i}$ is the quadrupole strength for the $\mathrm{i^{th}}$ beam size measurement, $l_{quad}$ is the quadrupole effective field length , $L_d$ is the drift length between the quadrupole and the screen. The system of equations is well determined for the case of three measurements with different quadrupole currents. More than three measurement results turn the system into a overdetermined one and allow to estimate the uncertainty of the parameters.

The MINUIT package [63] is used to find a fit for a set of experimental data using the least squares approach.

A disadvantage of this setup with the quadrupole before the dipole is that in the meter long drift between the quadrupole and the slice choosing slit (70 cm before the dipole, 30 cm after) the vertically defocused beam growth in size and the total vertical size is dependent on the quadrupole current. Therefore the slice content changes within the scan.

Each slice has a different mean energy value, and therefore a different energy normalization factor in Eq. 2.4. A way to treat the modified divergence is to plot the slice orientation in trace space in terms of normalized values. Assuming that $\beta \approx 1$ and putting Lorentz factor $\gamma$ under the square root in the emittance formula one obtains:

$$\varepsilon_{norm} = \beta\gamma\sqrt{\sigma_x^2\sigma_{x'}^2 - \langle xx' \rangle^2} \approx \sqrt{\sigma_x^2(\gamma\sigma_{x'})^2 - \langle x(\gamma x') \rangle^2} \tag{4.13}$$

and all quantities in the equation are describing the particular slice (e.g. $\gamma$ is an average for the slice because we are neglecting the slice energy spread, which is of the order of a percent). Distributions of slices are shown in trace space already with a normalized divergence to exclude the effect of off-crest acceleration. No coupling is assumed between the vertical and horizontal plane.

**Quadrupole after the dipole.** The major part of the procedure is similar as described in the previous paragraph. The advantage of this setup is that the quadrupole is positioned in the dispersive section 40 cm downstream the momentum filtering slit, hence the charge content participating in the measurement is constant during the scan. Though due to the space restrictions the drift length to the screen is only 1.207 m and results in a smaller waist RMS size (ASTRA simulations: with TESLA booster down to 40 $\mu m$, with CDS booster down to 25 $\mu m$). For the experimental data see section 5.2.2.1.

**Emittance on-crest and off-crest at different locations.** Conditions of the slice emittance measurement in the scheme discussed above are not nominal due to the introduced energy chirp in the booster cavity, whereas the phase on-crest is used for the projected emittance optimization. A set of simulations using ASTRA with space charge interactions was performed to get an estimate of the effect on projected and slice emittance. The simulation assumes optimized beam conditions for a 1 nC beam, a homogeneous laser spot with an RMS size at the cathode of 0.39 mm, and a flat top temporal profile of 21 ps FWHM. The beam is accelerated on-crest in the gun and in the booster cavity first on-crest acceleration is chosen as well and then -30 degrees off-crest phase is used. The results are presented in Fig. 4.8. All the plots are showing projected or slice emittance as a function of solenoid current at different locations along the beamline: EMSY1, quad for the slice emittance before the dipole (H1Q3), at the slit mask for the slice emittance at EMSY2, and at the quadrupole in the dispersive section (D2Q1). The average slice emittance values (shown in Fig. 4.8) are obtained by splitting the beam into 10 slices and computing a weighted average of those. Fig. 4.8(a) indicates the projected emittance of the beam accelerated on-crest in the gun and the booster cavity. The corresponding results, but with the booster -30 degree off-crest phase are shown in Fig. 4.8(b). The values are slightly higher than for the previous case. The lower row of plots shows the average slice emittance of the beam accelerated on-crest in the gun: on-crest in the booster cavity (Fig. 4.8(c)) and with the -30 degrees off-crest booster phase (Fig 4.8(d)). For both the slice and the projected emittance values there is no significant change due to the off-crest phase. Remarkable though is that the minimum average slice emittance does not significantly change along the beamline in the given range. The minimum occurs at the solenoid current of 380-382 A. It points to the fact that the growing minimum projected emittance along the setup is caused by the increased slice mismatch.

The average slice emittance value does not change when changing the booster phase to -30 degrees off-crest. But if one looks at the slice orientation in phase space there are certain differences (Fig. 4.9). The mismatch factor[1] is calculated between the same longitudinal slices in on-crest and in off-crest acceleration modes. The beam is divided into 6 slices with the same particle content for both cases of the booster acceleration with the on-crest

[1]Comparing two phase space distributions in terms of the second order statistical momenta can be done using the so called mismatch factor [17]. If phase space distributions are given in terms of RMS size $\sigma_x$, covariance $\langle xx' \rangle$ and RMS divergence $\sigma_{x'}$ one can

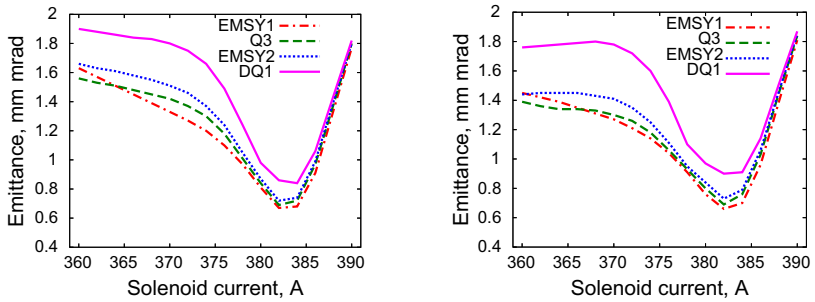


(a): on-crest projected (b): off-crest projected

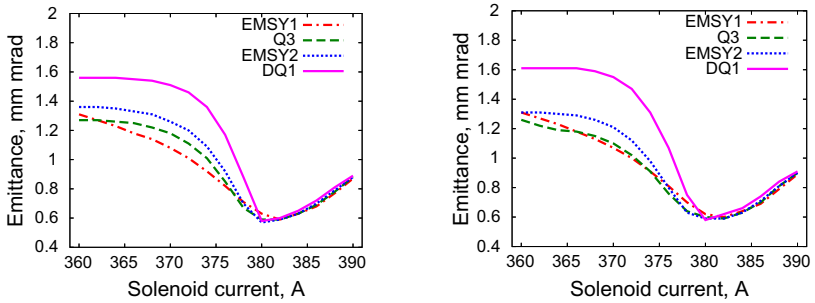


(c): on-crest slice (d): off-crest slice

**Figure 4.8:** Emittance as a function of the solenoid current at different emittance measurement locations: plot (a) shows projected emittance of the on-crest accelerated beam in the gun and the booster; (b) shows projected emittance of the beam accelerated -30 degrees off-crest in the booster; plot (c) shows average slice emittance of on-crest accelerated beam in the gun and in the booster; plot (d) shows average slice emittance of the beam accelerated -30 degrees off-crest in the booster.

and off-crest phases. The slice arrangements are depicted in phase space (Fig. 4.9(b)).

Here the conclusion is drawn that the minimum slice emittance value that is measured with the slice emittance measurement setup in three dif-

calculate the mismatch factor F of any two phase space distributions :

$$F = \frac{\left(\sigma_{x_1}^2 \sigma_{x_2'}^2 + \sigma_{x_2}^2 \sigma_{x_1'}^2 - 2\left\langle xx' \right\rangle_1 \left\langle xx' \right\rangle_2\right)}{2\varepsilon_1 \varepsilon_2} \tag{4.14}$$

with F=1 means the distributions are fully matched. If F > 1 the distributions are mismatched. Larger F values correspond to a stronger mismatch.

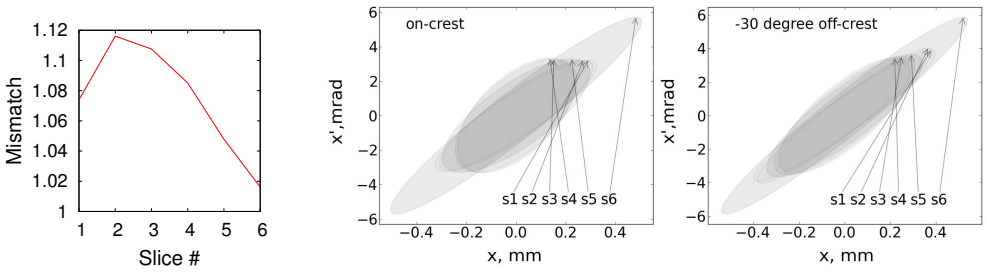


**Figure 4.9:** (a) mismatch factor between the same longitudinal slices of an on-crest and of an off-crest beam; (b) this difference in phase space.

ferent locations is within the expected measurement error of 10% equal to the slice emittance values expected in the case of the beam on-crest acceleration in the booster cavity. Still the slices' phase space distributions might differ, that is why the phase space obtained from the slice emittance measurements with the beam accelerated at off-crest phases in the booster can reconstruct and optimize the relative slice orientation only to a certain level - the best matching of all the beam slices can be found, but the individual slice properties can differ from the on-crest case.

## 4.2 The dipole current calibration into time

The outcome of the slice emittance measurement is emittance as a function of the dipole current. One is interested, however, to obtain the beam slice emittance as a function of time. The dipole current convertion to time is done in two stages. First, the dipole current is calibrated into momentum units. This calibration is derived from the current to field calibration and the dipole transform matrix (Eq. 4.2). The next transformation is between the momentum and time. The beam longitudinal phase space is a map for this transformation, as already mentioned. A direct measurement of the longitudinal phase space in the dispersive section was planned using the aerogel Cherenkov radiator and a streak camera. Since the system was not in operation and no calibration could be obtained during the period of the slice emittance measurements presented in this thesis.

It is also possible to use the beam momentum scan versus the booster phase for the calibration. In Fig. 4.10 the bunch momentum is shown versus

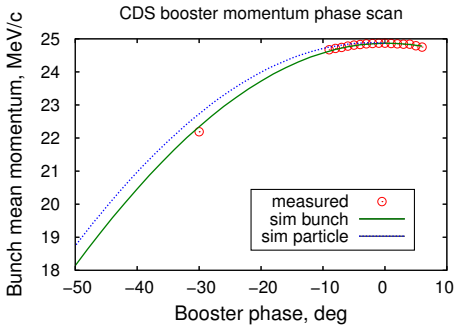


**Figure 4.10:** Bunch mean momentum versus the booster cavity phase for a single particle simulation (blue dotted line), 1 nC bunch simulation (green solid line), 1 nC measurement results (red circles).

the CDS booster phase. The dotted curve represents a single particle simulation, the solid line shows a simulation with a bunch that is generated at the cathode using a laser pulse of 21 ps FWHM duration. The circles show the measurement results.

A correlated momentum spread introduced to a bunch in the slice emittance measurement is much larger than the momentum spread of the bunch before the acceleration in the booster cavity. The momentum of the outcoming particles is determined by the entrance phase in the booster. The dependence was not measured and needs to be simulated (see Fig. 4.10 for the difference between the phase scans of a single particle and of a bunch). The measurement is in principle possible using the shortest laser pulse that can be produced. The dependence is fitted by a second order polynomial function:

$$\mathrm{p_z}(\psi) = \mathrm{a}\psi^2 + \mathrm{b}\psi + \mathrm{c}, \tag{4.15}$$

where a, b and c are the fitting parameters. The deviation from the phase scan curve does not exceed 2% and it can be analytically inverted into the phase as a function of the longitudinal momentum. The corresponding time of the cavity entrance is calculated assuming that the zero time corresponds to the off-crest phase $\psi_{off}$:

$$t[ps] = \frac{(\psi[deg] - \psi_{off}[deg]) \cdot 10^3}{360 \cdot f[GHz]} \tag{4.16}$$

with $f$ - the booster driving field frequency. A particle following a reference trajectory in the dipole with a radius of curvature $R$ in a magnetic field $B$

has a longitudinal momentum $p_z$. The magnetic field dependence on the dipole current is parameterized with a linear function in a proper range of the hysteresis curve. The transverse components of the momentum are considered to be negligible in comparison with the longitudinal one. Then the latter can be expressed as a linear function of the dipole current $I_{dip}$:

$$p_z = qB/R = (s \cdot I_{dip} + q) \tag{4.17}$$

with calibration constants $s$ and $q$.

One needs to solve of Eq. 4.15 to obtain $\psi$ as a function of $p_z$. The result is placed to Eq. 4.16 and taking into account Eq. 4.17 one obtains time as a function of the dipole current:

$$t = \frac{10^{12}}{360 \cdot f} \left[ \frac{-b + \sqrt{b^2 - 4a\,(c - 90(s \cdot I_{dip} + q) - p_c)}}{2a} - \psi_{off} \right], \tag{4.18}$$

where the coefficient before the square brackets turns the wave phase in degrees into time in picoseconds; $a$, $b$ and $c$ are the fit parameters of the phase scan curve $p_z(\psi) = a\psi^2 + b\psi + c$; $s$ and $q$ are coefficients of a linear calibration of the dipole current [A] into the magnetic field [Gs] $B = e \cdot I + f$; $p_c$ is a momentum shift correction that corresponds to the position offset at the dipole's exit slit obtained in Eq. 4.8; $\psi_{off}$ stands for the off-crest phase used in the experiment, one needs this to introduce the origin shift to match the time axis zero to a particle entering the cavity accurately at the off-crest phase.

All the measurement results in Chapter 5 are presented with this type of calibration. The calibration non-linearity is considerable especially for lower off-crest phases in the booster. And therefore the slice duration changes stronger along the bunch for those phases.

## 4.3 Temporal resolution of the setup

There are several contributions to the slice emittance setup temporal resolution. A contribution that is controlled by the setup design is the width of the slit at the dipole exit. Other contributions depend on the beam parameters such as the longitudinal phase space distribution and the vertical beam size and the divergence at the dipole entrance. The slit contribution needs to be kept dominating to have similar setup resolution for different

beam conditions. This section draws up a simple model that allows to estimate the setup temporal resolution in terms of the slit width, and the beam properties that can be measured.

As seen above slices are cut out from the beam vertical transverse distribution after the dipole. Let's imagine a perfect case when the beam has an infinitely small transverse size at the dipole entrance, the slit at the dipole exit is infinitely narrow and only the particles with a unique momentum value are picked out. Their longitudinal positions might still be spread out (Fig. 4.11a). Particle scattering or penetration through the slit mask is not taken into account. If the particles that have passed through the slit are backtraced to the dipole entrance, their longitudinal distribution does not need to have hard edges. The smearing originates from a longitudinal position spread for a certain momentum value that is a property of the longitudinal phase space distribution. Therefore the method encounters a fundamental limit of the resolution that is dependent on the bunch longitudinal phase space distribution. This contribution is reduced by the stronger off-crest acceleration. The longitudinal distribution shape may vary and it is appropriate to use RMS values to characterize the setup resolution. The longitudinal resolution contribution is then $t_{locRMS}$ (Fig. 4.11(a)).

Another case: the vertical transverse position distribution of the monoenergetic particles at the dipole input will be treated as a momentum spread at the dipole output (Fig. 4.11(b)). This effect leads to a situation when particles of neighboring longitudinal slices are passing the slit at the same time due to a transverse position offset at the dipole entrance. In practice the resolution is defined by a convolution of the slit acceptance window and the vertical beam profile at the entrance of the dipole. As a simplification, that confirms to be in a good agreement with the simulations, one can take the quadratical sum of the RMS size of the convoluted distributions.

A simple approach to estimate the temporal resolution due to the slit width and the vertical beam size as the equivalent momentum spread is:

$$t_{slit} = \left( \left( \frac{w_{slit}}{2\sqrt{3}} \right)^2 + \sigma_y^2 \right) \cdot \frac{\overline{p}}{2R} \cdot \frac{t_{RMS}}{p_{RMS}}, \tag{4.19}$$

where $w_{slit}$ - is the width of the slit at the exit of the dipole; $p_{RMS}, \overline{p}$ are the momentum spread and the average momentum respectively; $t_{RMS}$ is the RMS bunch duration; $R$ - is the dipole design trajectory radius that equals to 0.3 m. The slice profile across the slit is considered uniform and therefore

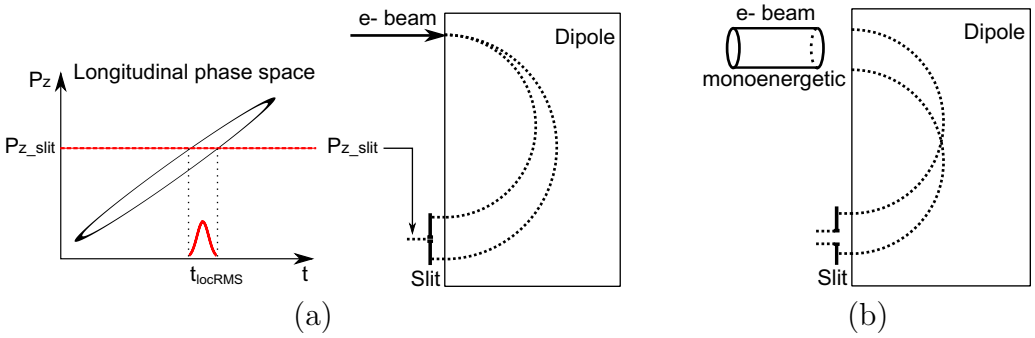


**Figure 4.11:** The three main contributions to the limited time resolution of the measurement method are shown. The sketch (a) demonstrates a transversely infinitely small beam that enters a dipole. At the dipole exit one obtains a pure longitudinal momentum spectrum. An infinitely narrow slit allows only a monoenergetic beam through. But it still maps a finite size particle longitudinal distribution. The sketch (b) shows a monoenergetic beam of certain transverse extension entering the dipole. At the dipole exit the beam size is interpreted as a momentum distribution. In a real case with a beam containing different momentum particles the time resolution is limited by mixing particles with different momentum values at the same transverse position of the output slit. The third contribution to the limited resolution is the slit itself contributing by its finite width.

the factor $1/(2\sqrt{3})$ indicates the relation of the slit width with the profile RMS size.

The slices are not equal in the momentum spread.

$$(\Delta p)_{slice} = \frac{w_{slit} \cdot p_0}{2R} \tag{4.20}$$

with $p_0$ is the momentum value of a particle on the reference orbit (R=0.3 m); changing the dipole current we tune $p_0$, other components stay constant resulting in a different slice momentum width along the spectrum. Difference of the slice in the bunch head and in the tail results in:

$$\delta(\Delta p)_{slice} = \frac{w_{slit}}{2R} \cdot (p_h - p_t), \tag{4.21}$$

where $p_h$, $p_t$ are momenta of the bunch head and tail, respectively. For the 5 mm slit that is 5/600 of the full bunch momentum span or less than a

percent. One should not forget that the slice widths in terms of time along the bunch can be significantly different due to non-linearity of the bunch longitudinal phase space.

The longitudinal RMS resolution of the setup $\tau$ is expressed via combining uncorrelated contributions of local longitudinal phase space position spread and the one described in Eq. 4.19:

$$\tau = t_{RMS}\sqrt{\left(\frac{z_{locRMS}}{z_{RMS}}\right)^2 + \frac{(w_{slit}/(2\sqrt{3}))^2 + \sigma_y^2}{(2R\frac{p_{RMS}}{\overline{p}})^2}} \tag{4.22}$$

or the relative resolution $\zeta$

$$\zeta = \frac{\tau}{t_{RMS}} = \sqrt{\left(\frac{z_{locRMS}}{z_{RMS}}\right)^2 + \frac{(w_{slit}/(2\sqrt{3}))^2 + \sigma_y^2}{(2R\frac{p_{RMS}}{\overline{p}})^2}}. \tag{4.23}$$

The value of $1/\zeta$ defines how many slices can be measured which do not overlap within their RMS widths.

The first term under the square root is significantly smaller compared to the rest of the contributions for the off-crest phase shift in the booster larger than 10 degrees. The rest of the contributions depends only on the slit width $w_{slit}$, vertical beam size $\sigma_y$ and the ratio of the longitudinal momentum spread $p_{RMS}$ and the mean momentum value $\overline{p}$. The formula is applied for the momentum spectrum obtained when the PITZ setup is simulated with ASTRA and the result is compared to a similar simulation, but where the particles which pass through the slit are traced back and the resolution is reconstructed (Fig. 4.12a). The values obtained by the formula are in a good agreement with the resolution expected from the simulated measurement except the phase on-crest, where almost the whole beam passes the slit and the consideration about the uniform slice profile at the slit is not any more applicable.

Fig. 4.12(b) shows the relative resolution $\zeta$ as a function of the booster phase and of the solenoid current. From this plot one can see that for the phases higher than -20 degrees the resolution is not so sensitive to the solenoid. The relative beam momentum spread there is still small and the slit width contribution is higher than the vertical beam size, in opposite to a phase range between -20 and -60 degree where the beam size with higher solenoid current is the dominant contribution to the resolution.

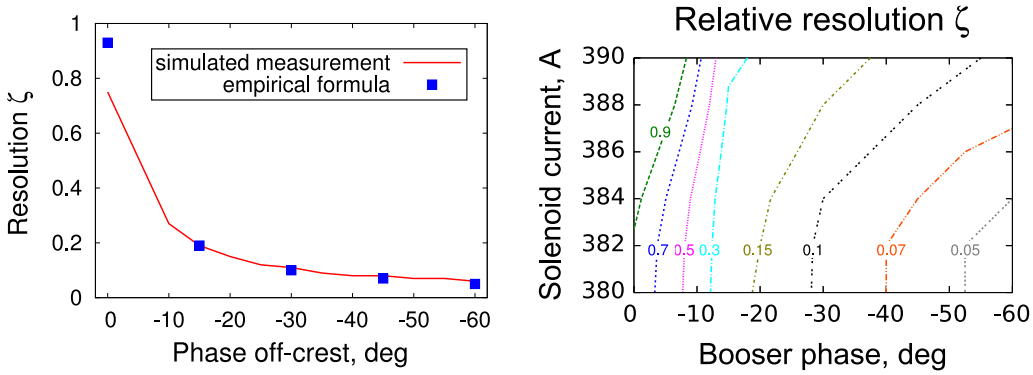


(a) (b)

**Figure 4.12:** Plot (a) shows relative longitudinal resolution as a function of the booster phase. The solid line is obtained from a measurement simulation using ASTRA; the points represent values obtained from the formula 4.23. Plot (b) shows the resolution as a function of the booster phase and the solenoid current.

In this section an empirical formula for the absolute and relative longitudinal resolutions of the slice emittance measurement setup was proposed. The relative resolution is well in agreement with the results of the simulated measurement. The example presented here is the case for 1 nC bunch charge. Lower charges can be focused more tightly and therefore the beam size contribution is reduced.

## 4.4 Optical read-out system design considerations

The beam profile on the screen is obtained via a CCD camera. The imaging is produced by a single achromat lens or by an achromat objective. Originally the camera for slice emittance measurements was chosen to be JAI RM-2030GE [64] with 1920x1080 pixels and a pixel size of 7.4 $\mu$m by 7.4 $\mu$m. The screens at the slice emittance measurement station have a tilt of 45 degrees with respect to the beam axis.

Applying the slit scan to a divergent beam requires a wide horizontal field of view at the beam observation screen. The beam RMS size after the slit mask is expected to be as small as 100 $\mu m$, and the depth of focus needs

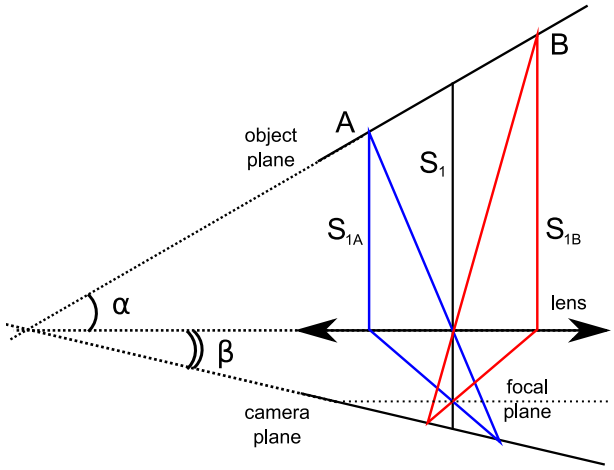


**Figure 4.13:** A scheme of optics arrangement obeying Scheimpflug rule

to be about five millimeters. In the quad scan measurement the beam is kept in the center of the screen, and the minimal beam RMS size in the focal point is $\approx 20\,\mu m$. For this type of measurement depth of focus is not a problem. Higher resolution is more important. The requirements for the two different measurement methods (slit and quad scans) are not compatible. A possible way to cover both needs is to use switchable optics.

During the commissioning process a test optical setup was used. It consisted of a Prosilica GC1350 [65] camera with 1360x1024 pixels and an objective with an adjustable focal length in the range of 50-108 mm. The objective was manually adjusted for the certain type of the measurement chosen. This measurement suffers from the depth of focus issue for the wide view field used in the slit scan.

This commissioning setup was not sufficient, therefore a new read-out scheme was designed. It includes two remotely switchable lenses. The first lens has higher demagnification, meaning also a wider field of view. This property corresponds to the needs of the slit scan. The second lens possesses a smaller demagnification factor and allows to resolve smaller beam sizes as required for the quad scan routine.

To overcome the depth of focus problem and to obtain the full surface of the screen sharp at the camera image, the Scheimpflug rule [35] was used to design the read-out optics. Fig. 4.13 demonstrates the geometry of the

**Table 4.1:** The switchable lens optical properties

| Property | Slit scan | Quad scan |
|---|---|---|
| Focal distance, mm | 120 | 180 |
| Magnification | -0.22 | -0.5 |
| Camera angle, degrees | -13 | -30 |
| Vertical field of view, mm | 64 | 28 |
| Horizontal field of view, mm | 36 | 16 |
| Optimized aperture radius, mm | 18 | 12 |
| PSF 80% integral energy radius, $\mu$m | 28 | 15 |
| 20% MTF, $\mu$m | 40 | 25 |

arrangement according to the rule. The rule can be expressed in a simple formula:

$$\tan\beta = M\tan\alpha, \tag{4.24}$$

where $M$ is the magnification factor on the optical axis. In our case $\alpha = \pi/4$.

The rule is applied to design a switchable optics system with two zoom lenses. The camera has two rotational states in the technical design, and switching can be done remotely. The full distance from the screen to the camera JAI RM-2030GE is 810 mm. The optimum lens aperture was optimized for both lenses using the OSLO EDU package [66]. The resulting design parameters are summarized in Table 4.1.

OTR radiation has a preferred direction of emission. The distribution function is cylindrically symmetric and depends only on the zenith angle $\theta$. The angular distribution of the emitted intensity for a relativistic electron incident on a perfect conducting plane is described by [30]:

$$I(\theta) \sim \frac{\theta^2}{[\theta^2 + \gamma^{-2}]^2}. \tag{4.25}$$

Taking the derivative of the expression one finds that the maximum of the intensity corresponds to the angle $\theta = \pm 1/\gamma$. Another property that has a practical use is the integrated intensity within the solid angle $\Omega$ corresponding to the zenith angle $\theta_0$. The integration of 4.25 gives the relative integral

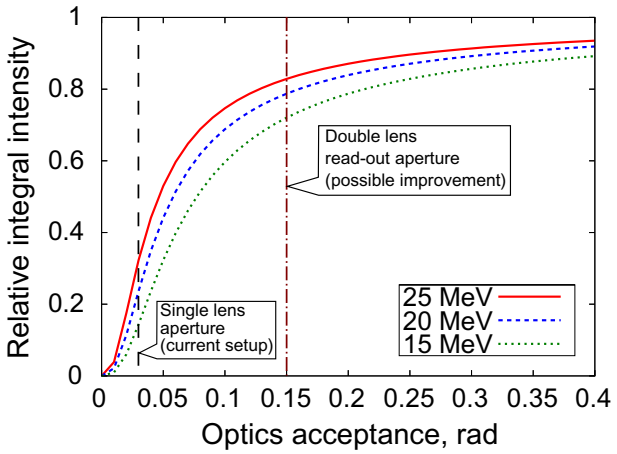


**Figure 4.14:** OTR screen intensity dependence on the read out optics acceptance angle.

intensity:

$$i = \frac{\int_0^{\theta_0} I(\theta)}{\int_0^{\infty} I(\theta)} = \frac{2}{\pi}\left[\arctan\gamma\theta_0 - \frac{\theta_0}{\gamma\left(\theta_0^2 + \gamma^{-2}\right)}\right] \tag{4.26}$$

An example of the value calculated for three different energies is presented in Fig. 4.14. This property depends on the energy of the particle. Based on Eq. 4.26 the read out optics aperture can be optimized to get the best possible intensity with a reasonable resolution. The current PITZ read-out system at the slice emittance screen was optimized for the resolution at the YAG. There is a special interest in getting more intensity from the OTR screen. A possible upgrade would be to implement a double achromat lense arrangement that increases the aperture and the intensity collected from the OTR screen (Fig. 4.14).

**Camera calibration factor.** The camera calibration process happens in situ using a calibrating pattern included in the optical beamline. The pattern is tilted 45 degree the same way as the screen and it consists of several squares of a known size (Fig. 4.15) and is uniformly back illuminated. Let's assume a square side with a size $L$ that is measured from a camera image to be $N_\perp$ pixels along the axis perpendicular to the tilt axis of the grid. The calibration factor $\kappa_\perp$ is:

$$\kappa_\perp = \frac{L\cos\frac{\pi}{4}}{N_\perp}, \tag{4.27}$$

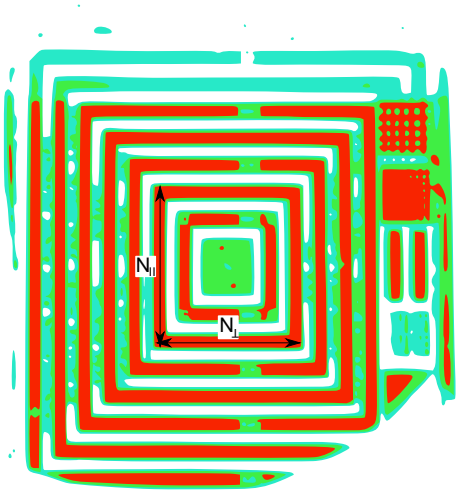


**Figure 4.15:** Grid pattern image as seen by the camera at the observation screen location. The pattern is tilted equivalent to the screen

where one has to include the fact that the beam transverse size is $\cos\frac{\pi}{4}$ times smaller than the beam profile appearing at the screen due to the screen tilt of $\frac{\pi}{4}$ in respect to the beam axis. It is important to mention that the calibration factor in the direction parallel to the screen axis of rotation $\kappa_{\parallel}$ is not affected by the screen and camera rotations and therefore is not equal to $\kappa_{\perp}$. The ratio of both is used as an accurate estimate for the camera tilt $\beta$ (see Fig. 4.13):

$$\cos\beta = \frac{\kappa_{\perp}}{\kappa_{\parallel}}. \tag{4.28}$$

## 4.5 Image processing

Beam profile images on the screen are captured with a digital 12 bit camera. The Prosilica GC1350 camera was used for the commissioning of the setup. In its final version with the switchable lenses another camera was implemented: JAI RM-2030GE. Both are digital CCD cameras without active cooling for normal room conditions. Some details of the specification can be found in Table 4.2. The CCD chip pixels that are not exposed to visible light still collect the signal generated by thermoproduction of electron-hole pairs, radioactive radiation impact and other sources, e.g. dark current. Additionally there is no possibility to completely block the light from the

**Table 4.2:** Camera properties

| Camera type | Prosilica GC1350 | RM-2030GE |
|---|---|---|
| Max bit depth | 12 | 12 |
| Resolution | 1360x1024 | 1920x1080 |
| Pixel size, $\mu m$ | 4.65 | 7.4 |
| Interface | GigE | GigE |
| Frame rate, fps | up to 20 | up to 32 |
| Manual black level | no | yes |

infrastructure environment. If the laser does not hit the gun photo cathode the image contains the dark current signal of the CCD chip, some light from the environment, and the dark current of the accelerator at the screen. All together they are considered as the background image and captured with the laser shutter closed. The background is later subtracted from the image of the screen containing the signal of photo electrons.

The remaining random noise has to be discriminated from the useful signal by means of filtering. The filters that are used for the image processing are based on intensity and space and time domain spectrum discrimination. The noise mostly contains higher spatial frequency contributions. Several additional filters are applied to filter the x-ray spikes, reduce camera specific and time dependent bias patterns. The filters were developed specificly for the needs of the slice emittance diagnostics. An example of the image filtering is presented in Fig. 4.16.

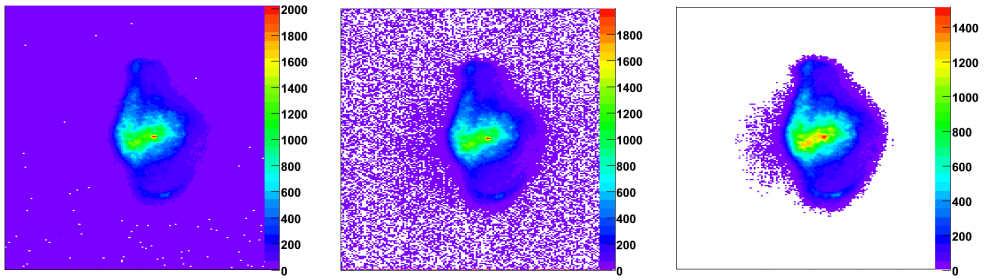


(a) (b) (c)

**Figure 4.16:** Image processing algorithm: (a) original image from a camera; (b) average background is subtracted from the image; (c) the image after the noise cleaning procedure

### 4.5.1 Bias frame and thermal noise

The CCD chip pixels are equivalent in their properties. Still due to the serial read out scheme of the CCD camera the bias frame can become inhomogeneous. The bias frame also depends on the camera settings like gain and black level. The accumulated radiation dose might also lead to higher dark current due to damaged pixels or the read-out electronics.

Before the signal is converted into digital format the signal range can be linearly adjusted to the constant input range of an ADC. There are two parameters that are controlling the range transformation: the gain corresponds to the stretching of an amplitude range, the black level is the offset of the range.

The gain allows to increase the captured details of the acquired digital signal in a certain situation. It has to be considered that the pixel signal is quasi-analog. The capacity of the pixel potential well is 40k electrons for the JAI camera. To digitize a low signal of 100 photo electrons it is sufficient to use 7 bits of the internal ADC. There is no need to adjust the signal to the higher dynamic range. It can be done though, no additional information is obtained. The signal spectrum will have gaps, because an electron higher pixel signal will correspond to ADC output digital code increment larger than one. Also some smoothing can happen due to the electronics noise, which is independently added from the amplifier.

The black level is an additive signal transformation. The dark current changes with temperature and the average dark signal of the pixels is changing. In this case the absence of light results in a certain signal higher than zero. Lets neglect the fluctuations first to understand the effect of black level. In a measurement the light signal is added to the electronic dark current signal. The sum must not exceed the upper limit of the ADC range. Therefore presence of any charge in the pixel which is not photo produced reduces the dynamic range of the signal. Hence a constant shift depending on the conditions can be applied to couple the base level of the dark image to the lower limit of the ADC range. If the dark current signal fluctuates then the shift has to be smaller. It must not lead to a situation where the incoming signal is lower than the ADC lower limit, because these pixel values are converted to zeros and consequently the fluctuation amplitude is faked.

In stable conditions one needs to adjust the black level only once, when setting up the system. If changing the gain leads to a shift of the noise distribution then a look up table has to be established to change the black level corresponding to the gain level. Most of the cameras have an automatic

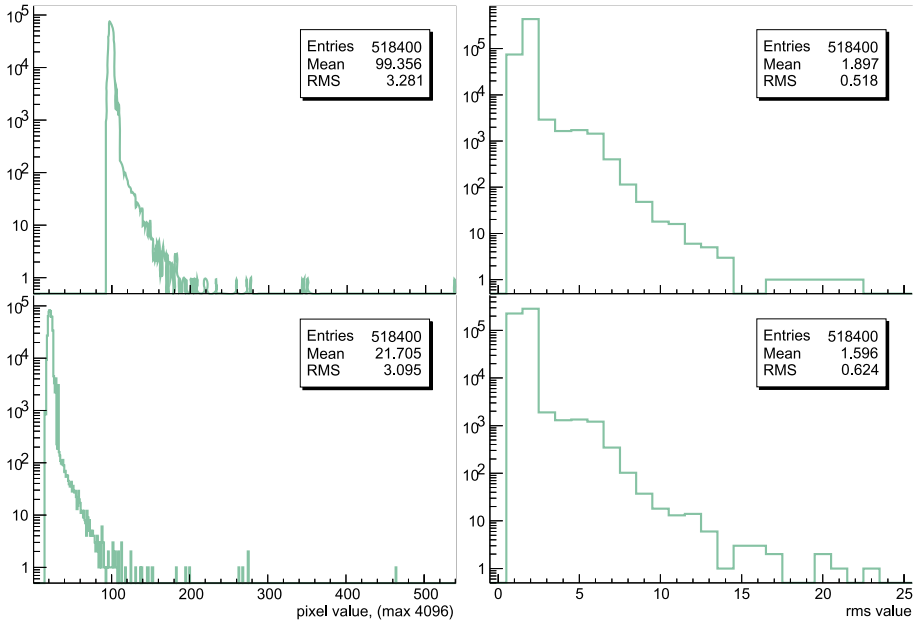


**Figure 4.17:** Dark current characteristics of the JAI RM-2030GE obtained using an array of 100 black frames at room temperature without any sources of radiation: on the left the average noise and on the right the RMS distributions of the pixel values are shown. The two rows correspond to different black level values with the same gain setup.

black level as an option (Prosilica GC1350 has only automatic black level control).

In figures 4.17 and 4.18 the dark current distributions of the discussed cameras are given as an example. 100 black frames were collected from the camera and each pixel's average and RMS values were evaluated. The left column always displays the average dark current signal distribution of the pixels, and the right one shows the RMS dark current signal distribution of the pixels. Fig. 4.17 presents the JAI noise distributions for two different black levels with the same gain. As one can see the change leads to a pure shifting of the average dark current signal distribution, while the RMS dark current signal distribution stays nearly constant. The Prosilica camera characteristics are shown in Fig. 4.18(a). The camera has an automatic black level control only. The experience shows that the accumulated radiation damage of the on board electronics of the camera leads to a malfunctioning of the adjustment. Fig. 4.18(b) shows the same noise characteristics for a

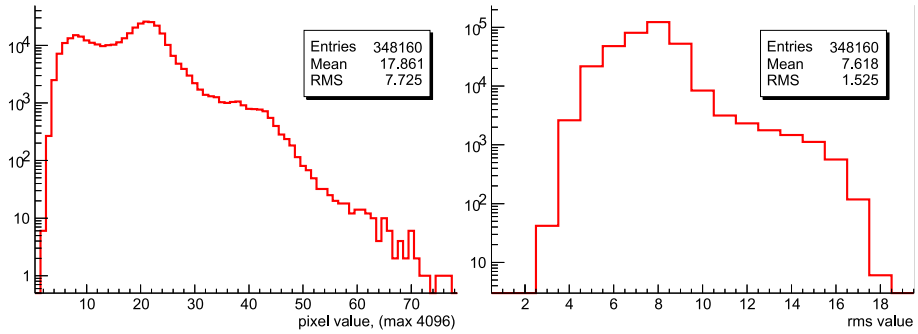


(a): new camera

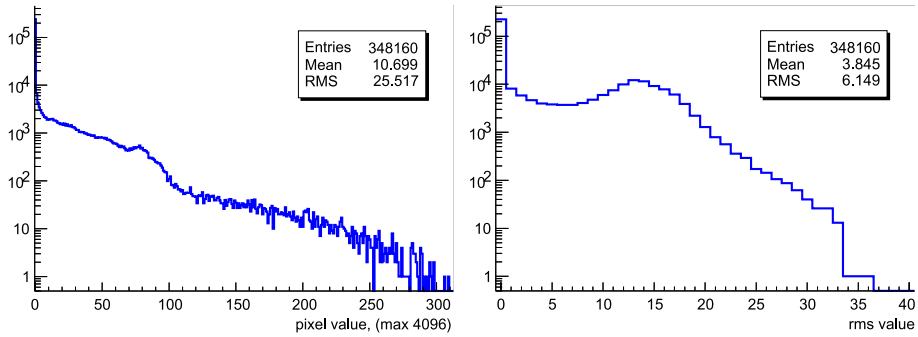


(b): radiation damaged camera

**Figure 4.18:** Dark current characteristics of the Prosilica GC1350 obtained using an array of 100 black frames at room temperature without any sources of radiation : on the left the average noise and on the right the RMS distributions of the pixel values are shown. (a) The noise characteristics of a new camera of this type. (b) The noise characteristics of a camera of this type that was for 2 months exposed to the radiation in the tunnel. The radiated camera adjusts the lower threshold of the ADC range not correctly. As a consequence intensity of most of the pixels is zero all the time, despite the overall normal photosensitivity

heavily irradiated camera (no estimate of the dose can be done). Two thirds of the pixels deliver zero average and zero RMS dark current signal. Nevertheless the chip stays photo sensitive, meaning when exposed to intensive light not a single pixel shows zero values. The drawback of using such a camera is the low photo signal discrimination.

### 4.5.2 Image filter benchmark

In order to proceed with the data analysis one needs to extract a beam distribution from an image 2D array. The task is not straight forward as we know that the intrinsic camera noise overlaps with the photo signal all over the chip. The procedure of useful signal separation is called noise filtering. As any separation of comparable signals it is destructive and still due to the statistical nature of the noise does not guarantee that no noise is left in results. Normally a bunch distribution on the screen has much higher peak intensity than the noise, and any distribution that completely fits within the chip has edges where the intensity drops to zero. Especially these regions are very sensitive to the noise cleaning procedures.

In order to give a description of the image filter the following simulation is set up. An artificial signal is introduced in the form of a gaussian profile along the horizontal axis with a uniform distribution along the vertical axis. The noise is uniformely distributed over the chip, and its amplitude is considered to have a gaussian distribution with a mean value $N$ and an RMS $\sigma_n$ of the distribution. Applying a filtering procedure one can estimate the reduction of the signal distribution RMS size as a figure of merit.

In this section we test a set of filters that was used for slice emittance data analysis. The principle of noise discrimination resembles the one used in [11]. A signal pattern with the RMS size of 10 pixels was used. The filter is sensitive to the signal to noise ratio, that is used here as a peak value:

$$SNR = \frac{P_{max}}{\sigma_n}, \tag{4.29}$$

where $P_{max}$ is the maximum pixel value of the signal distribution. The number of frames is another parameter that changes the result significantly. The test was done for two sets of image and bias frames: 5 and 10 frames. The number of the signal and the number of background frames is equal. The results can be seen in Fig. 4.19 and tells what is the relative reduction of the gaussian horizontal profile size after a set of filters is applied. The cut depends on the amplitude separation between the noise and the signal, and to show this, the cut is plotted against the signal to noise ratio.

The resulting behavior is important to take into account when processing the scan data. The peak intensity of the beam distribution decreases towards the edges of the distribution. For instance the central beam part passing the EMSY 50 $\mu$m slit and being detected at the screen 360 cm downstream has an $SNR \approx 240$ (the peak intensity is adjusted to the camera value$\approx$ 4000)

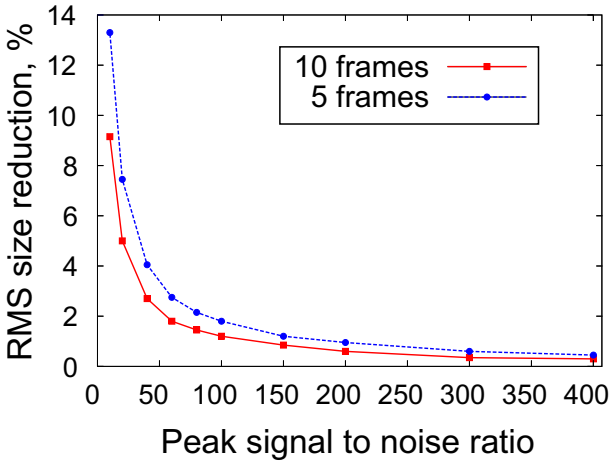


**Figure 4.19:** The result of the described filter benchmark test

and the periphery part of the full beam has only an $SNR \approx 30$. The corresponding cuts are 1% and 6% at five frames. The preparation for the quad scan instructs to adjust the beam intensity in the focus on the screen to the maximum of the camera range. The scan current range is chosen to get the waist size doubled at the edges. The linear estimation is well justified in practice and it results in the SNR reducing by half to $\approx 120$, which means that the cut in the scan changes from 1% in the center to 2% towards the edges of the scan.

In conclusion, the image processing approach tested here is used as a basis for slice emittance measurements. The filter does distinguish between noise and signal by amplitude discrimination. This results in a cut of measured distribution tails that is a function of the peak signal to noise ratio in the proposed model. The cut varies for the slit scan in a range between 1% and 6%. For the quad scan this range lies between 1% and 2%.

# Chapter 5

# Results of simulations and measurements

This chapter presents simulation studies and results obtained using the slice emittance diagnostics described above. The setup was initially studied using simulations. Three parameter (laser spot size at the cathode, the solenoid current, the booster gradient) scans were performed to find the emittance minima for various bunch charges. The measurement results are divided into two main parts. The first describes the commissioning of the slice emittance setup. The second part contains the measurements, which were done to test the feasibility of the slice emittance diagnostics for a set of bunch charges. The same size of the laser spot on the cathode and a moderate booster phase off-crest shift were used to compare the measurements with different bunch charges. Still for 100 pC one had to reduce the laser spot size and off-crest phase shift to obtain a reasonable signal to noise ratio. Corresponding measured projected emittance values are given as a reference for every slice emittance measurement. Two measurements with the same setup were performed using the quadrupole and slit scan measurement techniques. None of the measurements was tested for reproducibility.

## 5.1 Slice emittance studies using ASTRA

A high-brightness photo injector has to extract the maximum bunch charge possible for a given cathode laser pulse duration. A compromise between the growing bunch charge and growing emittance has to be considered. Therefore particle dynamics is strongly space charge dominated in the first cen-

timeters of the cavity before particles reach relativistic velocities. Particularly along this short distance the bunch phase space distribution is distorted and the emittance is diluted. There is no direct measurement that could monitor the process as it happens. The first diagnostics can be installed about a meter downstream from the cathode. At the PITZ setup projected emittance diagnostics is located almost at six meters downstream. It lets us measure and optimize the resulting bunch emittance that combines the degradation of individual slice emittance due to a non-linear space charge impact and the compensation of the slice phase space distributions mismatch via a solenoid focusing, but these contributions to the emittance budget can not be studied separately via projected emittance measurements.

One of the beam dynamics codes that supports particles' trajectory evaluation in external electro-magnetic fields and the bunch space charge field is ASTRA [61]. Most of the design calculations at PITZ are based upon this code. This particle-in-cell simulation software solves the differential equations of motion of super-particle propagation in cylinder symmetric external electro-magnetic fields with 2D (cylinder symmetry) and 3D (cartesian coordinates) routines for the space charge field calculation.

The PITZ setup in ASTRA is composed of three on-axis fields: the gun RF filed, the solenoid constant magnetic field, the booster cavity RF field (Fig. 5.1). The fields are defined by the maximum field gradient values and the initial phases for RF fields. The gun gradient is chosen to be 60 MV/m, the CDS booster cavity gradient is varied to match the resulting maximum mean momentum of the bunch at its output and the range is from 15 to 22 MV/m. The phases are set separately to get the maximum mean momentum of the bunch first after the gun and then after the booster. These phases are taken as reference zero values.

Emittance can be directly calculated using a 6D ($\{x, y, z, p_x, p_y, p_z\}$) particle distribution generated by ASTRA as a result of tracing the beam to a specific z coordinate. Another way is to establish a simulated measurement setup. A simulated measurement requires that every process relevant to the real emittance measurement should be reconstructed in simulations. For a simulation of a slice emittance measurement with an energy-chirped bunch it means tracking the bunch through the booster cavity in an off-crest phase, turn it in the dipole, use one of the quadrupole magnets or a slit mask, collect beam sizes at a screen as a function of the quadrupole current or the slit mask position and then obtaining the bunch emittance.

Projected emittance is minimized by varying the solenoid current and the

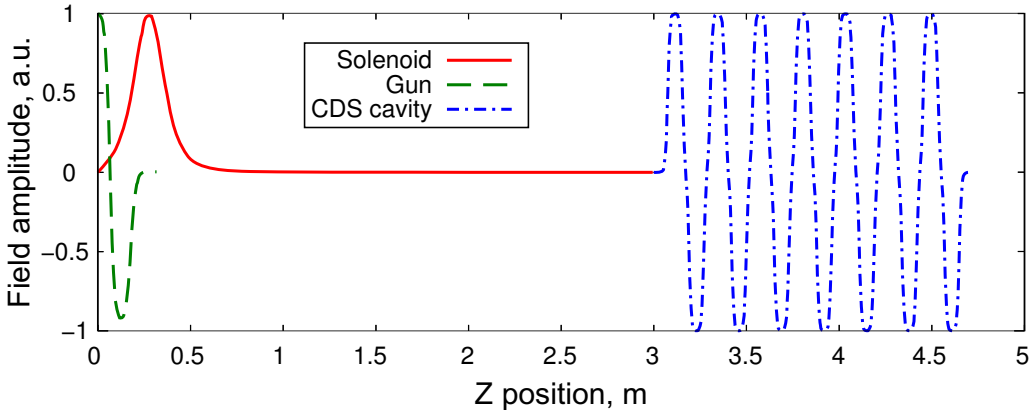


**Figure 5.1:** PITZ setup external electro-magnetic field map for ASTRA simulations.

laser spot size at the cathode. EMSY1 is the station closest to the position of the minimum projected emittance along the setup [11] that is why further optimization is performed at this location.

This section has two subsections devoted to PITZ setups one with the TESLA booster and the other with the CDS booster. All simulations are done assuming 0.55 eV energy of the electrons escaping from the cathode.

### 5.1.1 Optimization with TESLA booster

The main optimization is done for 1 nC bunch charge generated with a laser pulse of 21 ps FWHM duration and 2 ps rise and fall times. Temporal and transverse laser pulse shapes are flat-top. The gun is simulated with a peak field gradient of 60 MV/m and accelerates the bunch to a momentum of 6.6 MeV/c. The booster peak field gradient is fixed to 15 MV/m which results in a total bunch mean momentum of 14.3 MeV/c. The projected emittance is optimized at the EMSY1 position by varying the laser spot size at the cathode (RMS values are used unless specified) and the main solenoid current. Results are presented in Fig. 5.2(a). The total emittance has a smooth minimum along the laser spot size axis formed by the emittance value increase due to the growing thermal emittance contribution on one side (larger laser spot sizes) and by the growing space charge contribution on the other.

The minimum emittance along the solenoid current axis occurs at the

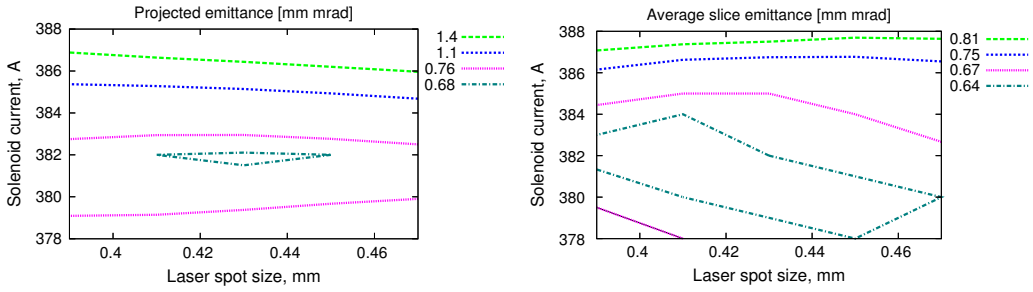


(a) (b)

**Figure 5.2:** Beam projected emittance optimization for a bunch charge of 1 nC at EMSY1 with the TESLA booster using ASTRA.(a) The plot shows the projected emittance as a function of the laser spot size on the cathode and the solenoid current for a booster gradient of 15 MV/m; (b) the same for the average slice emittance.

best compensation of the slice mismatch and of the non-linear space charge deformation (see section 2.2). In the presented case the minimum emittance value of 0.67 mm mrad occurs with the laser RMS spot size of 0.43 mm and the solenoid current of 382 A. The corresponding beam size, projected and central slice emittance evolution along the beam line are shown in Fig. 5.3(a). The bunch emittance and current temporal profiles are displayed in Fig. 5.3(b).

Fig. 5.2(b) presents the average slice emittance scan in the same space of parameters as for the projected emittance. The average slice emittance value $\varepsilon_{av}$ is calculated by splitting the bunch into 9 slices of equal length and averaging the emittances $\varepsilon_i$ of the slices weighted by the corresponding particle content $w_i$:

$$\varepsilon_{av} = \sum_{i=1}^{9} w_i \varepsilon_i, \tag{5.1}$$

and $\sum_{i=1}^{9} w_i = 1$.

The minimum value is 0.63 mm mrad and it is possible to obtain the value within a 2% deviation for all spot sizes in the presented range. The optimum solenoid current lies in a range between 378 and 384 A, depending on the laser spot size.

A bunch average slice emittance must be smaller or equal to the projected

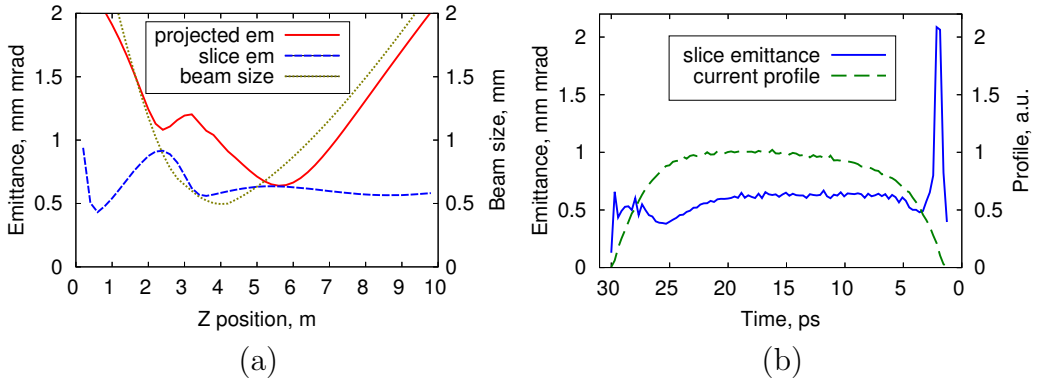


**Figure 5.3:** Setup with TESLA cavity: (a) beam size, projected and central slice emittance values along the setup for the optimum laser spot size of 0.43 mm and the solenoid current 382 A; (b) the slice emittance and the current along the bunch at EMSY1 location.

emittance because it excludes the phase space distribution mismatch of the slices. In the best case when the slices are well matched the emittance values coincide. As seen from the simulation the difference between the optima of the averaged slice and projected emittance values is about 6% showing that the minimum projected emittance is close to the full compensation.

The slice emittance minimum is flatter than the projected emittance minimum. The slice emittance minimum shifts down along the solenoid current axis for larger spot sizes at the cathode. The dependence of the optimum solenoid on the spot size indicates that the slice emittance value is affected by compensation of non-linear effects. The projected emittance value is additionally affected by the slice mismatch. The two effects are included in the projected emittance and together they form the minimum along the solenoid weakly dependent of the laser spot size, pointing out that non-linear distortion is a minor effect when compared to the slice mismatch.

### 5.1.2 Optimization with CDS booster

The setup with the CDS booster is optimized based on a criterium of projected emittance minimization. Following an existing layout of the experimental setup known as PITZ1.8 projected emittance was simulated for longitudinally [1] and transversely flat-top shaped laser pulses.

[1] 2 ps rise and fall times, 21 ps FWHM duration.

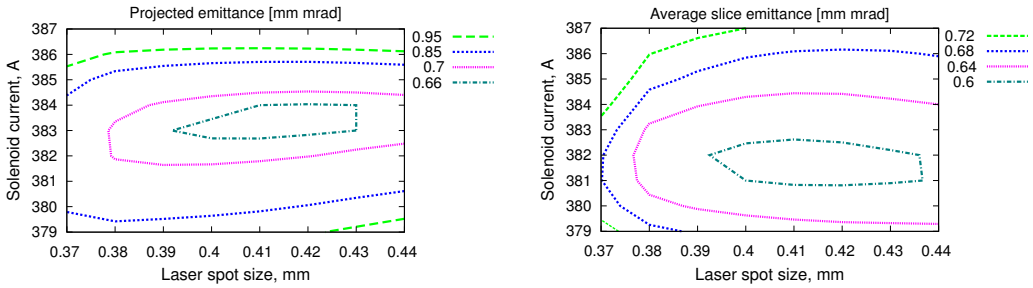


(a) (b)

**Figure 5.4:** Projected emittance optimization for 1 nC at EMSY1 with CDS booster using ASTRA. (a) The plot shows the projected emittance as a function of the laser spot size on the cathode and the solenoid current for a booster gradient of 21 MV/m; (b) the same for the average slice emittance

.

The optimization parameters include the laser spot size on the cathode and the solenoid current. The maximum achieved bunch mean momentum after the booster is 25 Mev/c, which corresponds to a peak booster gradient of 21.1 MV/m in the simulation setup. The beam projected emittance is obtained at the EMSY1 location. The results are shown in Fig. 5.4 in the same manner as for the TESLA booster results.

The optimum projected emittance value of 0.65 mm mrad is achieved at the spot size of 0.41 mm and the solenoid current of 383 A. The value is slightly lower than for the TESLA case. Fig. 5.5 shows the bunch size, projected and central slice emittance values along the setup (z coordinate) for this optimized case.

In order to understand the dependence of the minimum projected emittance on the booster cavity gradient another set of simulations was done. For each value of gradient a scan over the laser spot sizes at the cathode and the solenoid current was conducted. Only the minimum value of the solenoid scan is presented in Fig. 5.6. Within 2% deviation the minimum projected emittance value can be achieved for each gradient value in the scan range.

The average slice emittance (as defined by Eq. 5.1) minimum of 0.59 mm mrad is found at the laser spot size of 0.41 mm and the solenoid current 382 A (Fig. 5.4(b)). This value is 8% lower than the projected emittance. There is about two amperes difference between the projected and the slice minima.

The nominal bunch charge at PITZ is 1 nC. Following a recent trend

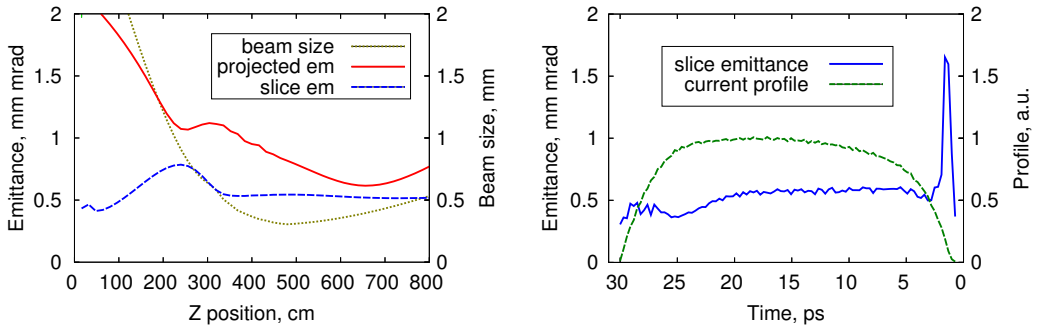


(a) (b)

**Figure 5.5:** Setup with CDS cavity: (a) beam size, projected and central slice emittance values along the setup for the optimum laser spot size of 0.41 mm and the solenoid current 383 A; (b) the slice emittance and the current along the bunch at EMSY1 location.

of accelerator driven FELs to operate at lower charge levels [2] additional simulations were done for 100, 230 and 500 pC. The laser pulse shape and the hardware setup up to EMSY1 were kept the same. The emittance values were optimized by varying the laser spot size on the cathode and the solenoid current. Results of the simulations are presented in Fig 5.7.

The minimal projected emittance values obtained in the simulation are 0.20, 0.27 and 0.44 mm mrad for 100, 230 and 500 pC, respectively. Corresponding minimum average slice emittance values are 0.14, 0.20 and 0.37 mm mrad.

It is interesting that the slice emittance minimum is slightly shifting up

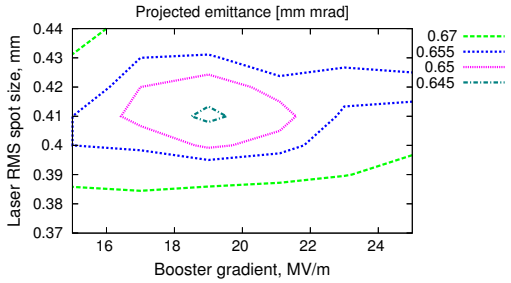


**Figure 5.6:** Minimum projected emittance of the solenoid scan as a function of the booster gradient and of the laser spot size at the cathode

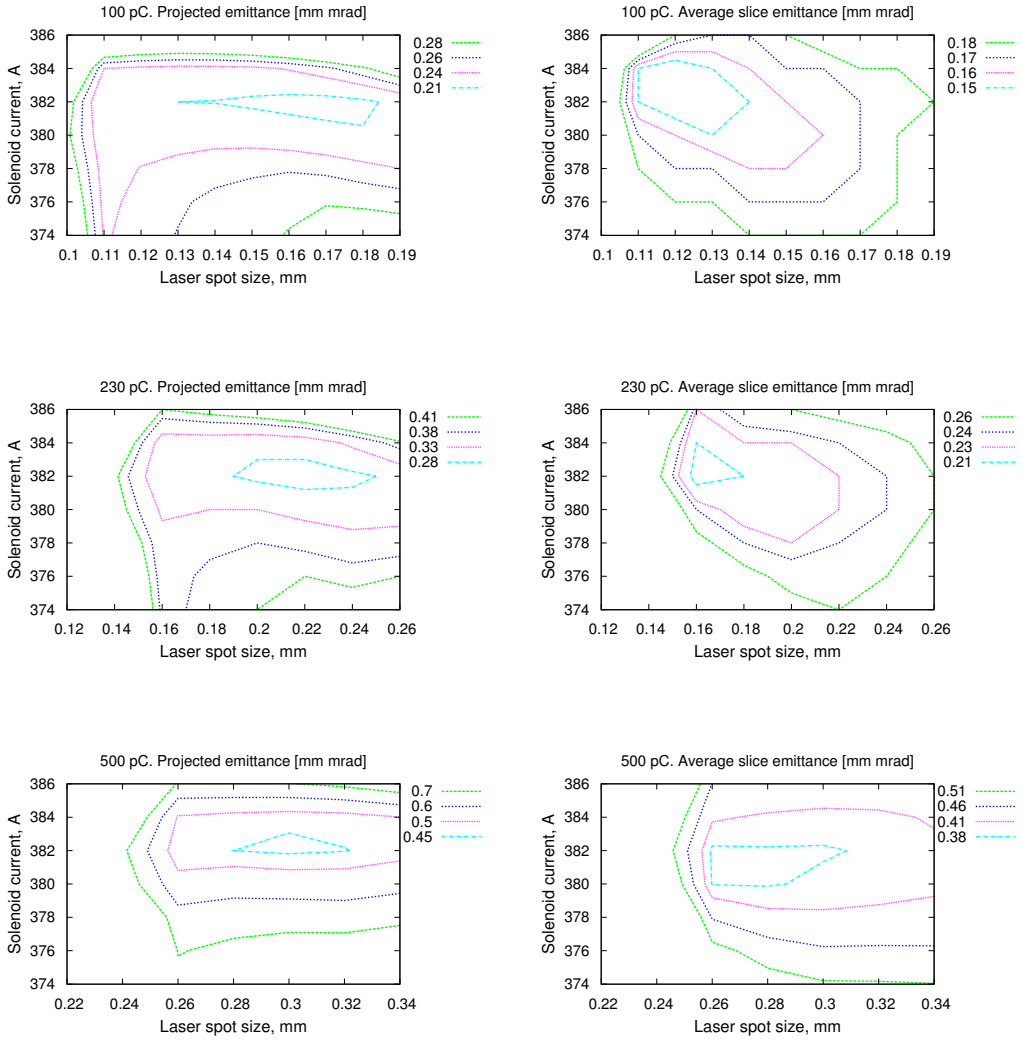


**Figure 5.7:** Projected and average slice emittance scans over the laser spot size at the cathode and the solenoid current ranges for the following charges: first row is 100 pC; second row is 230 pC; the last row is 500 pC

along the solenoid current axis relative to the projected emittance minimum for lower bunch charges.

### 5.1.3 Simulation of a quadrupole scan with the CDS booster

This simulated measurement is based on ASTRA and a dipole tracing software (linear approximation, no space charge). A schematic representation of the simulation procedure is shown in Appendix C.1. A bunch of particles is first traced through the setup to the location of the quadrupole in front of the dipole (see Fig. 4.6(b)). The quadrupole current is changed in a loop and multiple distributions of the particles passing the quadrupole with various gradients are generated. The particles of every distribution are traced further with ASTRA cylinder symmetric space charge fields until the dipole entrance.

In order to take the horizontal space charge impact into account a copy of each distribution at the dipole's entrance was created. The copy distributions undergo a tracking through the dipole with different dipole currents without space charge interaction. This distribution is only used to distribute the particles among the slices. The horizontal beam dynamics is reproduced with the original distribution. At the dipole exit a slice distribution is generated for each dipole current.

The original distribution meanwhile is tracked by ASTRA (3D space charge routine) along a straight section of a length equivalent to a trajectory inside of the dipole. In this case one neglects a vertical elongation of the bunch due to its dispersion. The horizontal space charge impact is thus stronger than in the dipole leading to an overestimation of the space charge contribution. At the position equivalent to the dipole exit the distribution is cut corresponding to the slice splitting, obtained with the copy distribution.

Finally the beam size is obtained as a function of the quadrupole current for each slice. The emittance is obtained using the standard processing procedure for slice emittance measurements. The results are shown in Fig. 5.8. The red line shows the slice emittance reconstructed in the simulated measurement using the quadrupole in front of the dipole. The simulation allows to split the beam into sharp longitudinal slices at the quad position directly and to calculate the original slice emittance. These slice emittance values are drawn with the green dashed line.

The simulated measurement and the directly calculated slice emittance are in close agreement at -50 degrees off-crest. The longitudinal resolution of the slice emittance measurements depends on the beam size at the dipole entrance. The beam size has a minimum at a solenoid current value of 384 A

in the simulation and the best agreement, as expected, can be observed at this current.

The emittance reconstruction using a linear quadrupole magnet model confirmed to be sufficient. The reconstructed slice Twiss parameters were compared to those at the quadrupole magnet entrance and showed mismatch factors within 1-1.2.

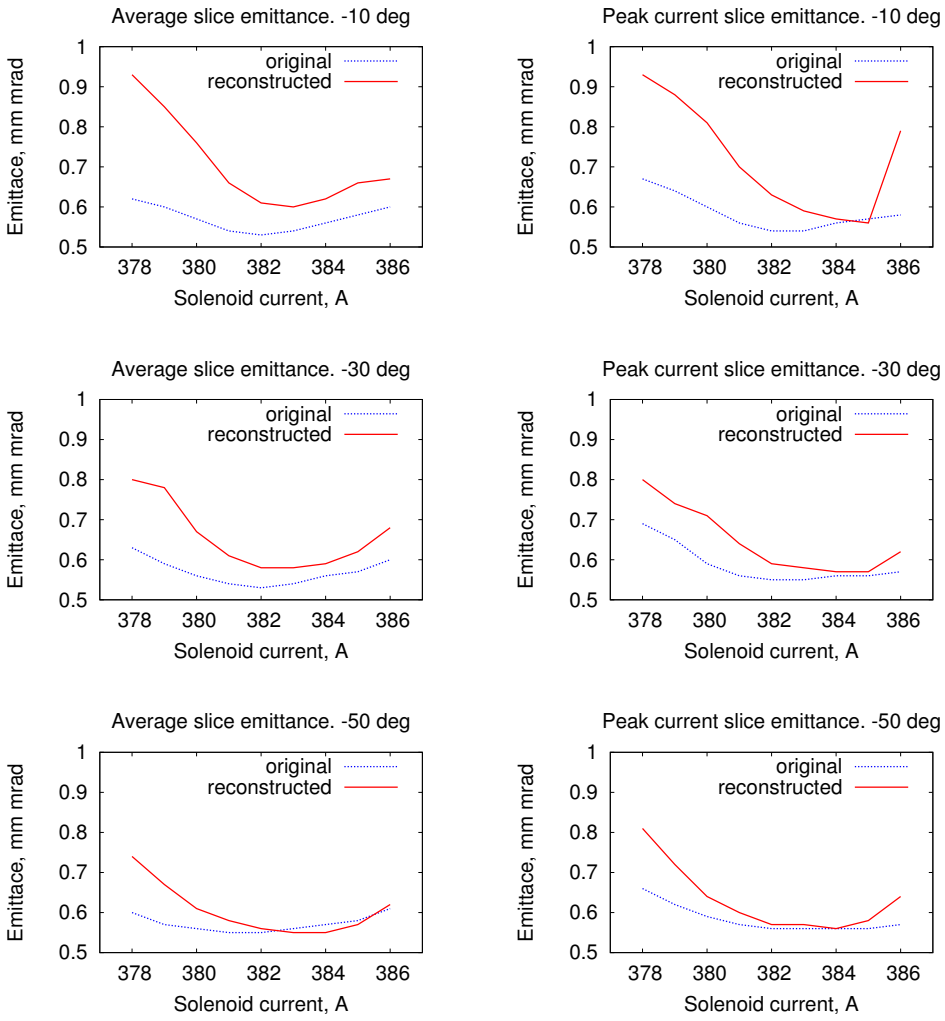


**Figure 5.8:** ASTRA simulation results showing the 1 nC bunch average slice emittance (left column) and the emittance of the maximum current slice (right column) as a functions of the solenoid at different off-crest phases. The blue dotted lines show the original slice emittance. Red solid lines represent results of the emittance reconstruction obtained in the simulated measurement.

### 5.1.4 Simulation studies summary

Summing the information obtained in this section one can conclude:

- All the above quoted emittance values contain 100% of the particle ensemble as defined in Eq. 2.4.
- The beam projected emittance minimum value was found in 2D parameter space of the laser spot size and the solenoid current in the studied range. The gun phase is fixed to 0 degree (phase of maximum mean momentum).
- TESLA: for the 1 nC bunch charge the minimum projected emittance is 0.67 mm mrad; the minimum average slice emittance is 0.63 mm mrad and is 6% lower.
- CDS: for the 1 nC bunch charge the minimum projected emittance is 0.65 mm mrad; the minimum average slice emittance is 0.59 mm mrad and is 8% lower.
- CDS: the optimized emittance value for the 1 nC bunch charge varies within 2% for the booster gradients in a range from 15 to 25 MV/m.
- CDS: emittance optimization was performed also for 0.5 nC, 0.23 nC and 0.1 nC. The minimum projected emittance values are 0.44, 0.27 and 0.20 mm mrad respectively. The minimum average slice emittance values are 0.37, 0.20, and 0.14 mm mrad, respectively.
- CDS: the slice emittance minima are shifted along the laser spot size and the solenoid current respectively to the projected emittance minima. This indicates a relation between the linear and non-linear transverse dynamics of the bunch.
- CDS: the results of the slice emittance simulated measurement show a good agreement for the peak current slice emittance value at -30 degrees off-crest in the booster, with -50 degrees off-crest in the booster both the average and the peak current slice emittances agree at a solenoid current of 384 A which corresponds to the smallest beam size at the dipole entrance (best longitudinal resolution).

**Table 5.1:** Measurement setup settings

| | Laser | | | | Gun | | | Booster | |
|---|---|---|---|---|---|---|---|---|---|
| Measurement # | laser RMS spot size, mm | rise, ps | FWHM, ps | fall, ps | Momentum, MeV/c | Charge, nC | Solenoid current, A | Momentum, MeV/c | Phase off-crest, degrees |
| 1 | 0.29 | 2.4 | 23.6 | 3.1 | 6.68 | 1.00 | scan | 14.6 | -50 |
| 2 | 0.37 | - | 13.2 | - | 6.58 | 1.00 | scan | 14.2 | -50 |
| 3a | 0.37 | 2.2 | 23.2 | 1.6 | 6.66 | 1.00 | 388 | 19.1 | -40 |
| 3b | 0.37 | 2.2 | 23.2 | 1.6 | 6.66 | 0.50 | 377 | 19.1 | -40 |
| 3c | 0.37 | 2.2 | 23.2 | 1.6 | 6.66 | 0.23 | 372 | 19.1 | -40 |
| 3d | 0.37 | 1.6 | 22.9 | 1.3 | 6.70 | 0.11 | 360 | 19.3 | -40 |
| 4 | 0.18 | 1.9 | 21.4 | 2.8 | 6.68 | 0.10 | scan | 25.1 | -20 |
| 5 | 0.30 | 1.9 | 21.1 | 2.6 | 6.70 | 0.23 | scan | 24.8 | -30 |
| 6 | 0.30 | 1.9 | 21.4 | 2.6 | 6.68 | 0.50 | scan | 24.9 | -30 |
| 7 | 0.30 | 1.9 | 21.4 | 2.6 | 6.68 | 1.00 | scan | 24.9 | -30 |
| 8 | 0.30 | 1.9 | 21.9 | 1.8 | 6.68 | 1.00 | scan | 24.9 | -30 |

## 5.2 Measurement results

Eight sets of experimental data are presented in this section (Table 5.1). The first three sets belong to the commissioning stage, the following four measurements are done using quadrupole scans for 0.1, 0.23, 0.5 and 1 nC. The last measurement set is a slit scan measurement with 1 nC. All results are represented with several types of plots:

- Slice emittance as a function of time. The plot is usually combined with the bunch current profile that indicates the charge distribution along the bunch taking the width of slices into account.
- Reconstructed trace space (only slit scan).

- Equivalent RMS ellipse phase space distributions of slices (only quadrupole scan).

- Emittance versus bunch charge fraction (only slit scan). The plot describes how the emittance value changes if one discriminates all charge outside a certain contour of equal charge density of the trace space distribution.

The laser temporal and transverse shapes which were used in the measurements are collected in Appendix D.1.

Error bars of emittance values include the statistical error of the measurements. Each emittance measurement using the quadrupole scan technique includes at least 10 different settings of the quadrupole current. For every measurement point 10 frames are taken within 1 second (10 Hz repetition rate). The complete quadrupole scan can take up to several minutes. If the system jitter period is tens of seconds the different scan points deviate from the correct curve although the spread of the beam sizes measured for a single quadrupole current is negligible.

Normally the scanning procedure collects more points than is needed for a fit. Combining the measured points into subsets and fitting them separately results in a set of emittance numbers. The statistical error in the measurements below indicates the emittance RMS value.

### 5.2.1 Slice emittance setup commissioning

The measurements described in this part were done with the TESLA booster and without the slit at the dipole exit. Instead the bunch slice splitting was done at the image processing stage by defining a vertical region of interest on the screen. In this approach the particle content of a slice does not stay constant during the current scanning of the quadrupole magnet. The first measurement presented here is done with a flat-top laser temporal profile of about 24 ps FWHM (see Appendix D.1). The second measurement was done with a gaussian laser temporal profile with an RMS duration of about 6 ps (see Appendix D.2). The emittance was measured for a selection of three solenoid currents around the focus on the EMSY2 screen in front of the dipole.

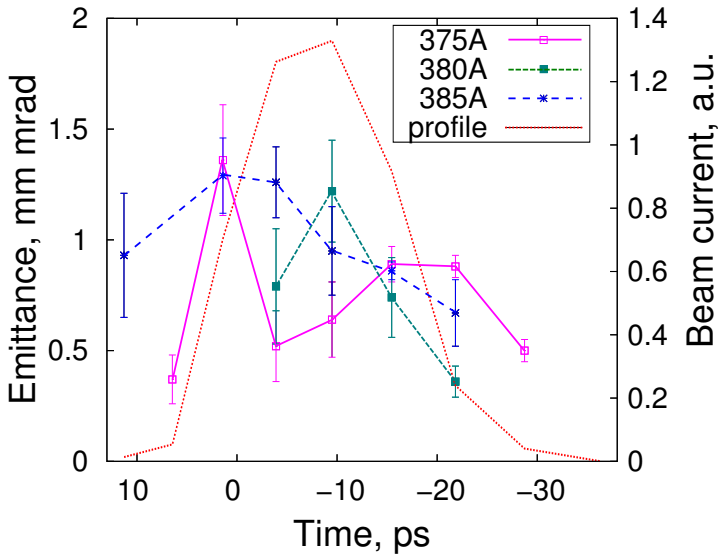


**Figure 5.9:** Measurement # 1. Slice emittance measurement results for 1 nC and an RMS laser spot size of 0.29 mm, temporal flat-top

#### 5.2.1.1 Measurement # 1. Flat-top laser pulse temporal profile with 1 nC charge, with an RMS laser spot size of 0.30 mm. Quadrupole scan

This slice emittance measurement is done following the settings of a recent projected emittance measurement. The lowest measured projected beam emittance in the X plane at the EMSY1 location was 1.00±0.03 mm mrad and in the Y plane was 1.16±0.03 mm mrad ($I_{sol}$ = 384 A, the gun phase is set -6 degrees off-crest) [67]. The measured laser pulse FWHM duration is 23.65 ps with rise and fall time of 2.4 and 3 ps, respectively . The measurement is done with -50 degrees off-crest phase shift at the booster using the quadrupole in front of the dipole (H1Q3). 45 pulses per train were used (maximum possible).

The slice emittance was measured for the three solenoid current values of 375 A, 380 A and 385 A. In Fig.5.9 the results of the measurement for three different solenoid currents are presented. Equivalent RMS phase space ellipses are shown in Fig.5.10. Several slice emittance values are missing due to improper measurement results (no minimum in the beam size scan). The error of most measured emittance values exceeds 20%. One of the reasons for the large error can be in a poor phase stability (the gun phase jitter RMS

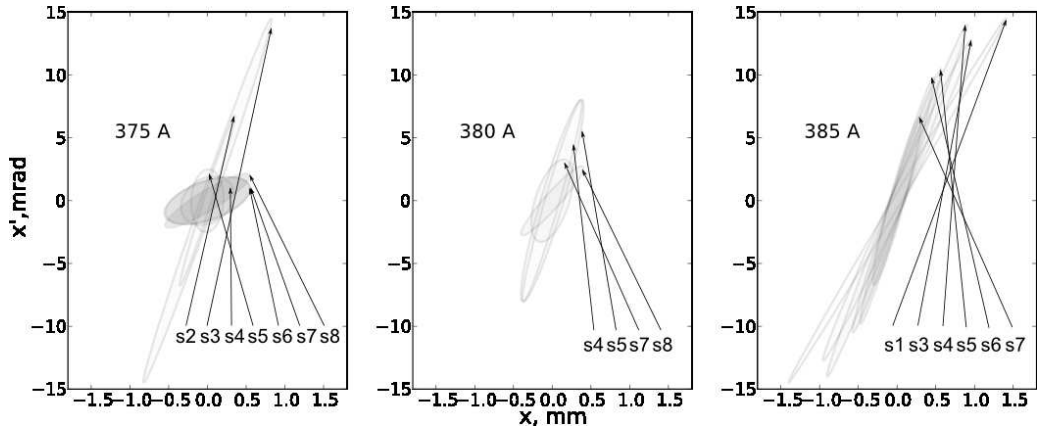


**Figure 5.10:** # 1. Equivalent RMS ellipse distributions in phase space for 1 nC and an RMS laser spot size of 0.30 mm, temporal flat-top

spread of 2-3 degrees) that was observed at PITZ in that run period [45]. On the other hand the commissioning objective was to test the suggested measurement procedure. That has shown several weaknesses. At this point one needs to head on a more qualitative measurement to be able comparing the slice emittance with the projected emittance.

#### 5.2.1.2 Measurement # 2. Gaussian laser pulse temporal profile with 1 nC, with an RMS laser spot size of 0.37 mm. A quadrupole scan and a slit scan measurement

This slice emittance measurement is also done following the settings of a recent projected emittance measurement. The beam measured projected X and Y emittances equal to 1.32 and 1.53 mm mrad, respectively. The values were obtained for the solenoid current of 374 A.

The RMS temporal duration of the laser is ≈6 ps (FWHM 13.2 ps), with RMS laser spot sizes of 0.37 mm. The gun phase was -6 degrees relative to the phase of the maximum momentum gain. The beam momentum after the booster on-crest was 14.3 MeV/c, the measurement was conducted using -50 degrees off-crest phase in the booster for the three solenoid currents of 368 A, 371 A, 375 A. The solenoid current 371 A corresponds to the minimum size at the second slit mask after the booster which is close to the dipole entrance. The beam emittance was measured using the dispersive section quadrupole magnet (D2Q1). Seven slices were measured for each solenoid

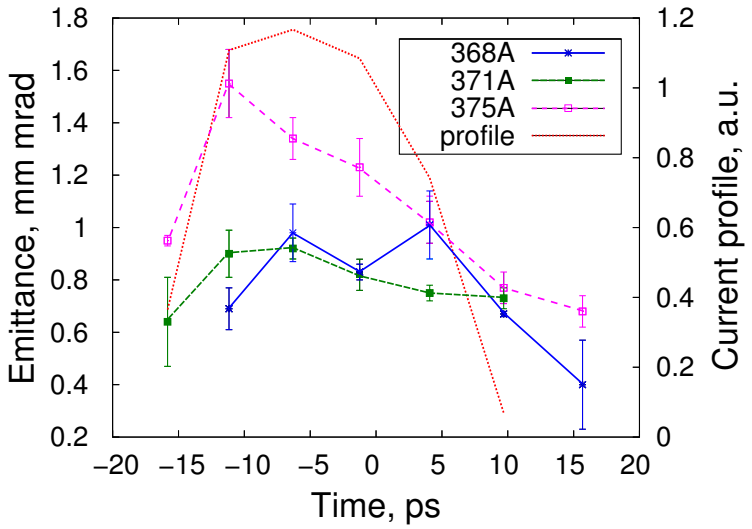


**Figure 5.11:** # 2. Slice emittance measurement results for 1 nC and the laser spot size of 0.37 mm, temporal flat-top

current. The closer quadrupole distance to the screen allows to focus the bunches tighter and therefore the intensity is higher. The measurement was done using 5-10 bunches in the train.

In Fig. 5.11 the slice emittance is represented as a function of time. There are two measurement points missing on the edges of the bunch. It happened due to slight energy drift which result in the bunch leaving the area of interest making the quadrupole scan data incomplete.

Similar to the flat-top case the equivalent ellipse phase space distributions are presented for the set of solenoid currents in Fig.5.12.

Starting with the solenoid current 375 A (1 A higher than that of the minimum projected emittance) showed that the beam is strongly overfocused at the position of the quadrupole, meaning that the emittance should be overcompensated. Further two measurements were done using lower solenoid currents approaching the beam focus at the quadrupole entrance.

For the focus on EMSY2 (371 A) a slit scan measurement was performed in similar conditions as the quadrupole current scan. The number of pulses was increased to its maximum value of 45. The results of the quadrupole and slit scans are compared in Fig. 5.13. Additionally the top plot demonstrates an ASTRA simulation of the beam conditions in the experiment. The simulated slice emittance though is calculated by splitting the beam

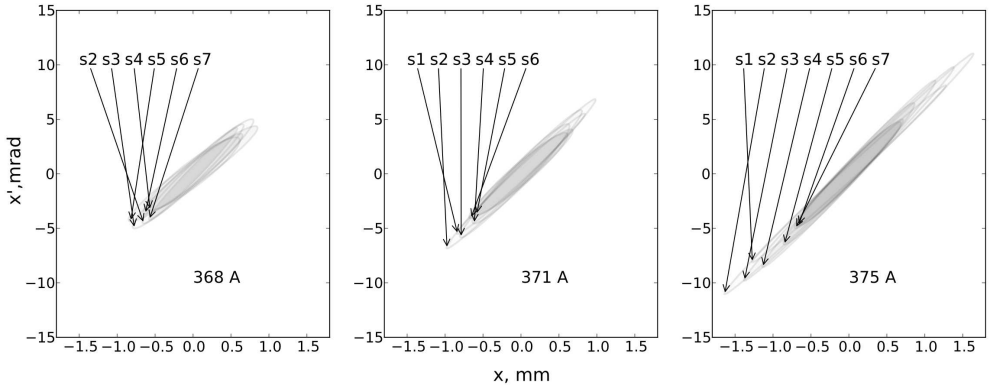


**Figure 5.12:** # 2. Equivalent RMS ellipse distributions in phase space for 1 nC and the laser spot size of 0.37 mm, temporal gaussian

into 20 longitudinal slices, two edge slices are left out due to a small number of particles contained in those.

Easy to notice that the beam in simulations has wider momentum spread, it means the original bunch is longer. The slice emittance for the case of a gaussian laser temporal shape has an emittance bump in the middle and emittance spikes on the edges. The structure is not clearly observed in the measurement results. One reason for this is that the RMS time

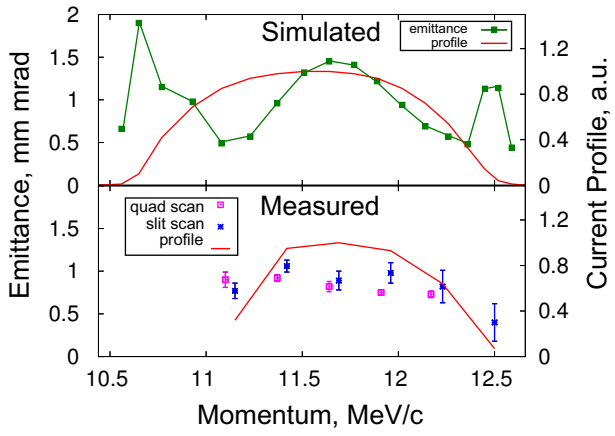


**Figure 5.13:** Gaussian laser temporal shape, 1nC. Comparison of the quad scan results and the slit scan results with a simulation for a similar setup using ASTRA.

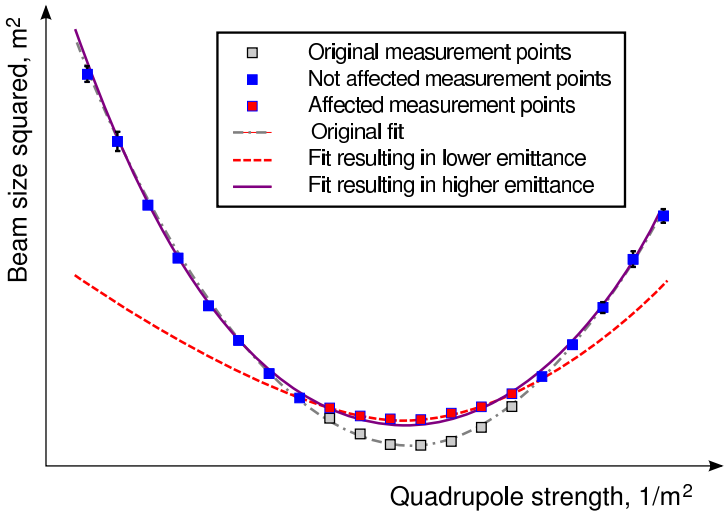


**Figure 5.14:** A quadrupole scan data set affected by the measurement setup resolution or by space charge. If one fits the distorted set using the full range the obtained emittance value is higher than the original one. If the fit is done only in the vicinity of the affected points the obtained emittance is lower than the original value.

resolution was about 1 ps. The simulated emittance spikes appear at the low intensity edges and, even if the signal is enough to perform a measurement, the contribution of the edges within the resolution is very small.

The slice emittance measurement has shown improved statistical error. The only difference in the measurement procedure was that the quadrupole which is closer to the observation screen was used hence one would expect to obtain a tighter focusing of the bunch. This improvement can result from the resolution issue which has shown to be more pronounced as described below in 5.2.2.1. The measured emittance values are around 1 mm mrad which are lower than it is expected from the simulation with respect to comparable projected emittance values. This might point to systematical errors which are included in the results of both types of measurements, the quadrupole and slit scans, but the reasons are different.

The quadrupole scan will certainly return inaccurate emittance results if the beam size in the waist vicinity is measured to be larger than in a linear model (distortion by the space charge). One can expect both an underestimation or overestimation (see an example in Fig. 5.14). After the shutdown with the new CDS booster the beam size in the waist got even

smaller and the problem became more pronounced.

The beam emittance is underestimated in the case of a slit scan measurement as well. The slit scan does not allow to measure the the tails of the phase space distribution due to a vanishing signal to noise ratio. One has to take into account that the central beamlet maximum signal to noise did not exceed a value 10. The systematical underestimation is then caused by a full discrimination of the outer beamlets as well as the individual beamlet size underestimation due to the low signal part discrimination of the beamlet spatial distribution.

Summarizing this measurement one needs to underline some unclear points in the results:

- the measured slice emittance is smaller than the expected value from the simulations (projected emittance is the same within the error bars). Both measurements can include systematical errors due to the screen saturation for the quadrupole scan measurements and due to the low intensity for the slit scan measurements;

- the measurement statistical error got lower although the only difference is that the quadrupole after the dipole was applied.

#### 5.2.1.3 Measurement # 3. The slice emittance setup testing with the CDS booster. Quadrupole scan

The new run period of 2010 was started with a new gun cavity [41] and with the CDS booster cavity [47] installed. With installation of the CDS booster the maximum beam energy increased to $\approx 25$ MeV. In the booster conditioning phase one could perform the slice emittance measurements only with lower booster gradients. The booster was not fully conditioned and did not allow to make a reliable emittance optimization. The measurements were done to test the method and corresponding tools and to check the signal level for lower bunch charges. A 5 mm wide slit was installed at the dipole exit for cutting out a slice (from this moment on the software splitting of the slices was not applied anymore).

At this period a set of measurements was done for different bunch charges of 1 nC, 500 pC, 230 pC, 110 pC to check that the signal is sufficient for the slice emittance measurements. The laser RMS spot size was 0.37 mm. The measured laser pulse profiles are shown in Appendix D.3. The off-crest phase was settled to -40 degrees. The dispersive section quad was used to maximize

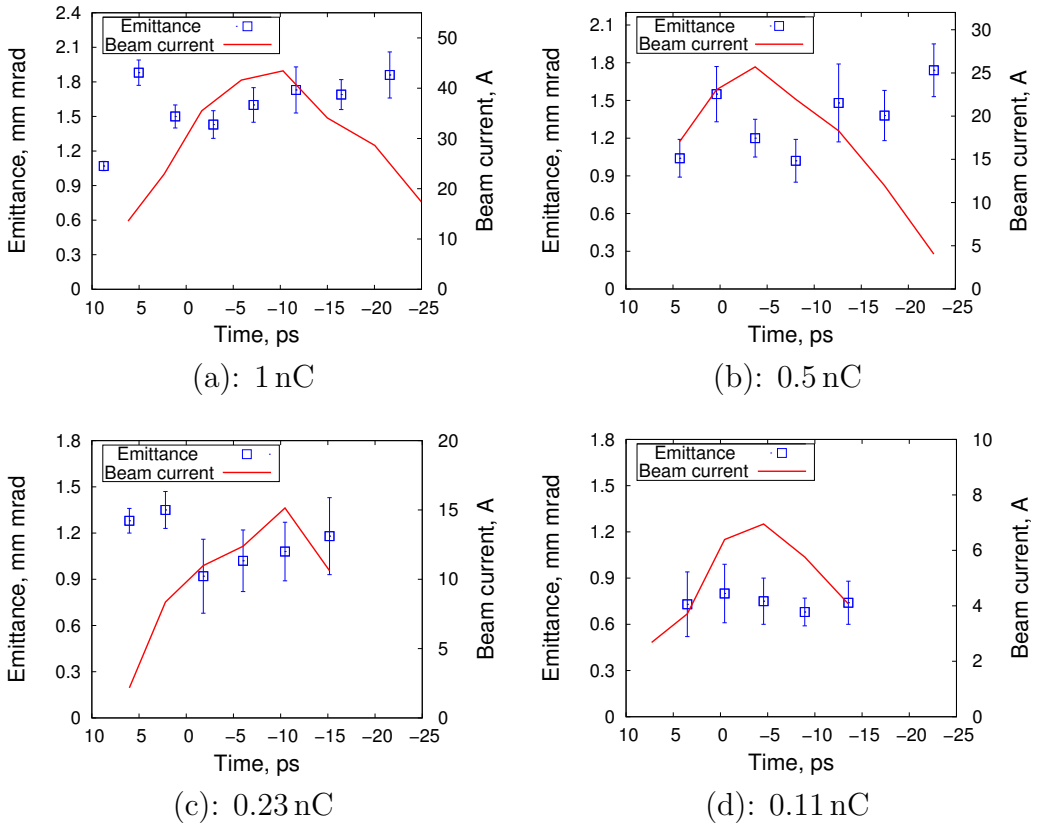


**Figure 5.15:** # 3. Slice emittance measurement results for different bunch charges and an RMS laser spot size of 0.37 mm, temporal flat-top

the signal. As the result only 3-5 pulses were used for 1 nC bunches and 20 pulses for 110 pC bunches. In order to be able to measure all charges within 2 measurement shifts the measurements were done with a single solenoid setting that focuses the beam on EMSY2

The overall beam conditions were poor since no standard optimization of the setup had been done yet. The measured horizontal (X) projected emittance of 1 nC bunch was measured to be ≈1.9 mm mrad. The slice emittance measurement results are presented in Fig. 5.15

In the quadrupole scans the minimum beam size measured for the charge of 1 nC was 62 $\mu$m. We have to keep in mind that in comparison with the previous measurement the particles' energy is higher, hence the particles divergence is reduced and the beam waist size in the scan decreases. The

normalized emittance though is higher and this may increase the beam waist size. The minimum beam sizes of about 60 $\mu$m are suspected to occur at the limit of the screen resolution due to saturation (see below).

This set showed that measurements with a bunch charge down to 110 pC are possible with the dispersive section quadrupole. The criterium here was the signal to noise ratio which showed to be about 200 for the waist point and is fully sufficient. On the other hand the minimum measured RMS beam size is limited at about 60 $\mu$m for 1 nC bunches. The minimum beam size measured with 110 pC went down to 50 $\mu$m which means that the effect might be dependent on the charge density. A description of the experiment intended to study this effect follows this section.

Once the slit at the dipole's exit is installed the time calibration can be applied. Also the beam current profile can be evaluated and results in a peak current of 43.5 A for the 1 nC bunch, 25.7 A for the 0.5 nC bunch, 15.1 A for the 0.23 nC bunch, and 7.0 A for the 110 pC bunch.

The slice emittance measurement might contain a systematic error caused by the limited resolution effect. In order to understand the beam size resolution limitation one needs another independent method of the beam size measurements. The OTR screen at the same position with YAG has shown to deliver extremely low intensity and no reasonable comparison could be done.

### 5.2.2 Slice emittance measurements using quadrupole scan

At the beginning of 2011 the cathode laser beam line was upgraded, new read-out optics for slice emittance was installed together with a new camera. The PITZ setup optimization started from scratch. First all the components were adjusted according to the standard optimization procedures and then the measurements of slice emittance were started. At the beginning a problem was observed that is described below.

#### 5.2.2.1 Quadrupole scan in HEDA1

The quadrupole in the dispersive section compared to the quadrupole in front of the dipole should deliver similar emittance results within a certain solenoid current range (see Fig. 4.8). The emittance values obtained with the dispersive section quadrupole are systematically 4-5 times higher. In

order to study this effect measurements of emittance were performed using both quadruple magnets in the same conditions.

First, the measurement was done using 250 pC bunch charge and -20 degrees off-crest in the booster using the quadrupole in front of the dipole (H1Q3). The main solenoid was first scanned to find the minimum emittance value of the central slice and then a detailed scan of four slices was performed at the solenoid current (393 A for this measurement). Then a measurement for the same conditions was done with the quadrupole in the dispersive section (D2Q1). In Fig. 5.16(a) the measured emittance of different slices is shown as obtained from the quadrupole scans with two different quadruples.

The main difference is that D2Q1 is located closer to the screen and the size of the focused beam is smaller than for H1Q3 (see section 2.3.2). To study the disagreement one can evaluate the beam size at the screen for the D2Q1 quadrupole scan using the beam parameters obtained from the H1Q3 scan. From the measurement with H1Q3 the beam parameters are obtained in front of the D2Q1 quadrupole. Then the beam is traced using linear beam optics and matrix formalism. The space charge was not observed to have a significant impact in simulations, although it does not exclude the effect in the experiment. The result shows that the expected beam RMS size in the waist should go down to about 30 $\mu m$ (Fig. 5.16(b)), but the measured size is 76 $\mu m$. For comparison the RMS beam size in the waist measured scanning H1Q3 quadrupole is about 140 $\mu m$.

The resolution can be limited due to different effects such as YAG screen saturation that was reported for an electron beam focused on a YAG:Ce screen [29]. The critical charge density found for a 100 MeV beam was 0.04 pC/$\mu m^2$. In case of the experiment at PITZ described above the density was not exceeding 0.0004 pC/$\mu$m$^2$ and YAG:Ce powder screens of 100 $\mu$m thickness are used at PITZ (a crystal of 250 $\mu$m thickness in the original publication [29]).

Another effect was reported in [33]. There was a YAG:Ce powder screen, 50 micrometers thick, and it showed a contribution of 140-180 $\mu$m to the RMS size resolution. The energy was 15 MeV and bunch charge 250 pC. The beam was focused with a quadrupole to produce the smallest possible size in the horizontal plane. The beam size measurements using a YAG screen are compared to OTR screen (50 pulses are integrated to achieve a comparable intensity with the YAG screen and a single pulse).

Also the optical read-out system was simulated and the expected optical resolution is better than 30 $\mu m$. The minimum RMS size that was measured

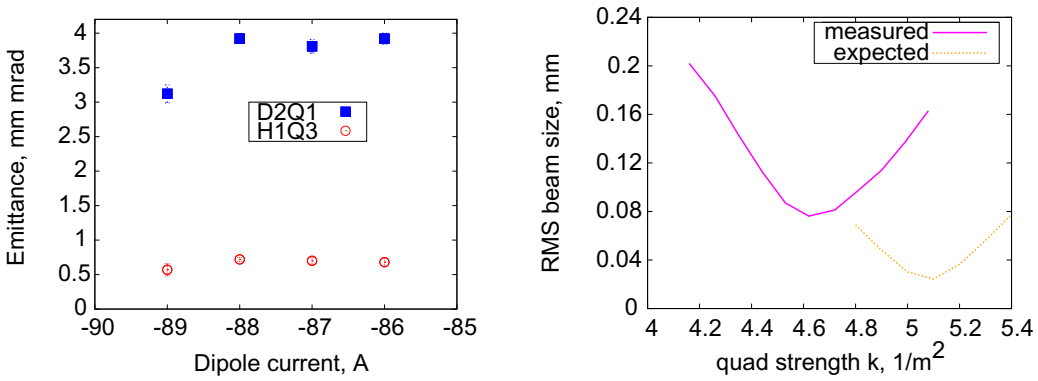


(a) (b)

**Figure 5.16:** (a) emittance measurement results are shown for the same conditions with two different quadruples: D2Q1 - in the dispersive section; H1Q3 - before the dipole. (b) presents the beam size at the same observation screen as measured during the quadrupole scan with D2Q1 and as predicted from the H1Q3 measurements.

with the screen is $\approx 60\,\mu m$. The OTR screen installed at the same position did not show enough intensity to obtain any reasonable data for comparison.

The bunch momentum spread contributes according to Eq. 2.44 about $10\,\mu$m quadratically to the measured beam size with $\sigma_x \approx 1$ mm, $\delta p/p \approx 1\%$, and the ratio of the drift length and the focal length is 1 ($\langle xx' \rangle = 0$).

Further investigation is needed to find the reason of the resolution limitation. As shown in Fig. 4.14 there is still room for improvement of the OTR intensity by a factor of 2-3 via enlargement of the acceptance aperture. Availability of the OTR screen gives an advantage of a direct comparison to a detector that was not observed to have any resolution limiting effect at this level of beam sizes. Another instrument that does not suffer YAG screen and optics read-out issues is a wire scanner. The one of the wire scanners in the PITZ straight section can be involved to exclude some of the resolution limit reasons mentioned above.

The conclusion is that the quadrupole in the dispersive section is inapplicable due to the observed resolution limitations. The limitation can be relaxed for certain setup conditions when the beam is not so sharply focused e.g. the solenoid should focus the beam at the quadrupole magnet entrance, respectively the beam emittance optimization can not be performed in the full range of the setup parameters.

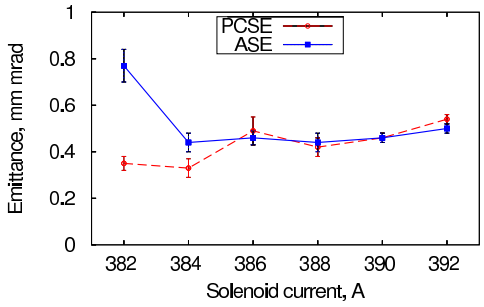


**Figure 5.17:** Slice emittance solenoid scan with 100 pC bunch charge. For PCSE and ASE see the text.

The results presented in the following section are obtained using the quadrupole H1Q3 in front of the dipole.

#### 5.2.2.2 Measurement # 4. Flat-top laser pulse temporal profile, 100 pC bunch charge, with an RMS laser spot size of 0.18 mm

This measurement was performed for 0.18 mm laser spot size on the cathode with 100 pC of the bunch charge. The laser pulse profiles are presented in Appendix D.4. A projected emittance measurement delivered 0.25 mm mrad for a similar setup settings with on-crest phase in the booster [41]. The beam was accelerated -20 degrees off-crest in the booster. The quadrupole in front of the dipole was used for the emittance quadrupole scan (H1Q3).

In the measurement the image of the focused beam showed peak signal to noise ratio of ≈30 which corresponds to an expected 4% underestimation of the beam size measurements (see Fig. 4.19, 50 pulses integrated within the exposure time).

In order to find the optimum solenoid current for the measurement a scan was performed (Fig. 5.17). Two quantities were used to study slice emittance as a function of the solenoid current. The peak current slice emittance (PCSE) corresponds to the emittance of the slice with the maximum average current (the slices have different duration and using only the slice charge would not be fully correct). The average slice emittance (ASE) is obtained by finding a weighted mean of the emittance of all the slices. The values are behaving the same way in the right part of the solenoid scan. For the lower solenoid currents the center slices (peak current slice belongs

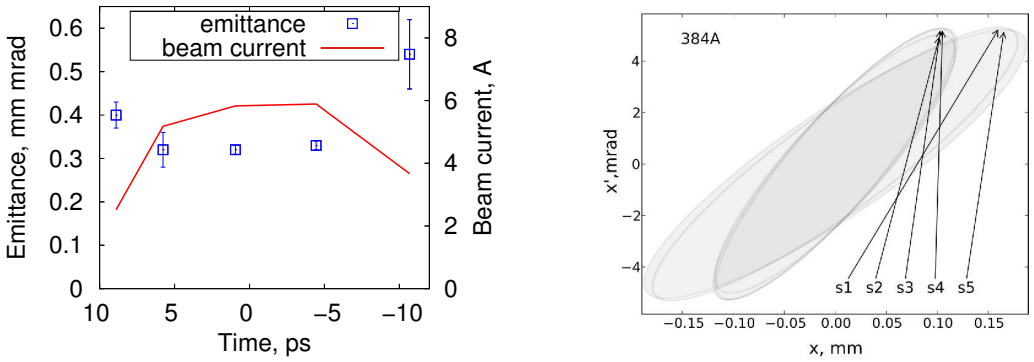


(a): slice emittance (b): slice orientation

**Figure 5.18:** The measurement result for a bunch charge 100 pC, laser spot size 0.18 mm, $I_{main} = 384$ A

to this part) emittance decreases while the emittance of the edge slices increases and pulls the average value up. The scan starting solenoid current is 392 A. Following the decrease of the emittance of the peak current slice the minimum point was found at 384 A. A detailed quad scan was conducted for five dipole currents at this solenoid current (Fig. 5.18(a)).

The peak current slice emittance was measured to be $0.33 \pm 0.01$ mm mrad. The same values within the errorbars were measured for the other two central slices. The outer slices showed higher values at the level of $0.54 \pm 0.08$ mm mrad for the head slice and $0.40 \pm 0.03$ mm mrad for the tail slice (see Fig. 5.18). The slice average emittance equals to $0.37 \pm 0.03$ mm mrad.

The higher values of emittance on the edges of the bunch are sensitive to the rise and fall times of the laser temporal shape in the ASTRA simulations. In Fig 5.19 one can see that a longer rise/fall time causes higher emittance at the edges. The tail is additionally influenced by a previously emitted charge and the charge density is not fully defined by the laser pulse shape and therefore the effect is more complex. The reason for higher emittance is in the changing charge density along the bunch that leads to a slice mismatch at a very short scale (much shorter than the setup resolution, meaning that the measurement delivers a "projected" value). In Fig. 5.19(b) one can see the slice mismatch within the slice number ten itself. The complete slice number ten emittance is 0.45 mm mrad. Subslices have emittances in the

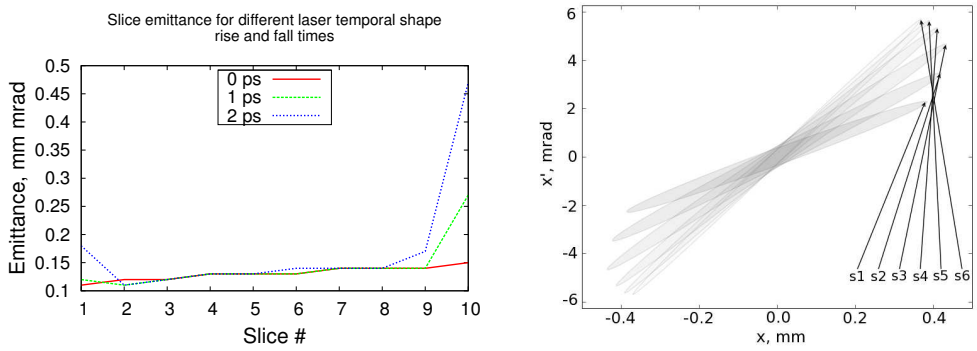


(a) (b)

**Figure 5.19:** (a) slice emittance simulation using ASTRA for three different rise and fall times of the laser temporal profile. The first slice corresponds to the bunch tail. (b) slice number ten (head) is split into 10 slices again and the phase space distributions of the six trailing of them are shown in terms of equivalent ellipses.

range of 0.11-0.19 mm mrad. The shorter the rise and fall time the smaller the number of particles (weight) that form high emittance edge slices.

One of the reasons of the slice emittance exceeding the projected emittance can be in a different number of pulses in the train used for the measurements. The projected emittance was measured with 10 pulses and the slice emittance measurement was performed with 40 pulses per train. The slice emittance measurement collects more short period machine parameter fluctuations [68]. The transverse laser profile is far from a flat-top in this measurement. The flatness of the profile was better for the projected emittance measurement.

The projected and slice emittance optima appear at different solenoid currents. The projected emittance value at the slice emittance optimum solenoid current of 384 A was 0.38 mm mrad. The slice emittance value at the projected emittance optimum solenoid current of 390 A was 0.41 mm mrad (both the average slice emittance and the peak current slice emittance). The simulation showed a difference of 16% with the absolute value of the projected emittance 0.25 mm mrad versus 0.16 mm mrad of the slice emittance with an RMS laser spot size of 0.18 mm and the solenoid current of 382 A.

The minimum projected emittance for 100 pC bunch charge, 0.22 mm

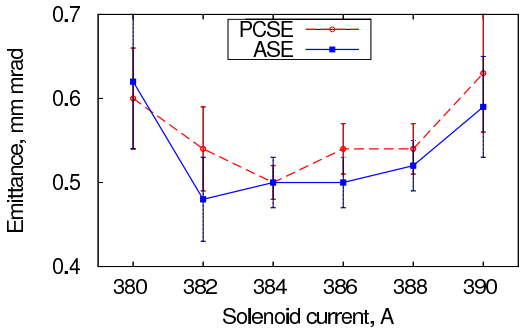


**Figure 5.20:** Slice emittance solenoid scan with 230 pC bunch charge.

mrad, was measured with an RMS laser spot size of 0.12 mm and a solenoid current of 390 A. In the simulation the optimized projected emittance of 0.21 mm mrad at the laser spot size of 0.17 mm, 382 A solenoid current.

#### 5.2.2.3 Measurement # 5. Flat-top laser pulse temporal profile, 230 pC bunch charge, with an RMS laser spot size of 0.3 mm

The laser shape is a flat-top profile with 1.87 ps, 21.08 ps, 2.57 ps corresponding to rise, FWHM, fall times. The transverse RMS laser spot size at the cathode is 0.30 mm. The longitudinal and transverse shapes can be looked up in Appendix Appendix D.6.

The gun phase is set to a value corresponding to the maximum beam mean momentum after the gun. With the setup the mean momentum reaches 6.7 MeV/c and the RMS spread is about 20 keV/c. The booster phase is adjusted first to the maximum mean momentum gain. With this phase the beam mean momentum equals 24.87 MeV/c and the momentum spread is about 100 keV/c. The phase is shifted to -30 degrees. The quadrupole in front of the dipole (H1Q3) was applied for the emittance measurement. The intensity is an issue and we used 50 pulses in a train and the signal to noise ratio was 43, the beam size systematic error for the case studied in section 4.5.2 would be 2-3%. The solenoid current scan was performed to find the minimum slice emittance value and the result is shown in Fig. 5.20. Three slices are measured for each solenoid current. The average slice emittance has a minimum at 382 A and the peak current slice emittance is minimal at 384 A. The detailed measurement was done only for

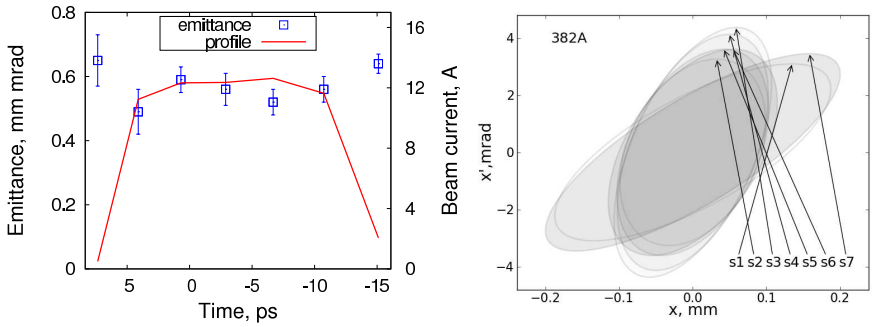


(a) (b)

**Figure 5.21:** Measurement results for a 230 pC beam, laser spot size 0.30 mm, $I_{main} = 382$ A.

the solenoid current of 382 A.

The best average slice emittance was measured for 382A. A detailed dipole scan was done with a smaller step resulting in 7 slices. The resulting emittance is presented in Fig. 5.21. The left plot shows the emittance as a function of time. The peak current slice emittance equals to 0.52±0.04 mm mrad, while the average slice emittance over all slices is 0.55 ±0.05 mm mrad. The right plot represents the slices' RMS equivalent ellipses in phase space. One can see that five slices in the middle are oriented much in the same way. The edge slices have similar orientation too but relatively to the middle part they are rotated. These slices correspond to the laser temporal profile rise and fall times and have different charge density, hence the phase space distribution undergoes different evolution along the setup.

Earlier projected emittance measurements with this aperture for 250 pC have obtained the minimum X emittance of 0.52 ± 0.02 mm mrad with the solenoid current of 388 A (fast scan of the slice emittance resulted in 0.52 ± 0.03). The solenoid current of the slice emittance minimum, 382 A, delivered the projected emittance of 0.59 mm mrad. Similar to the measurement with 100 pC the optimum slice emittance solenoid current is lower than the one for the projected emittance. As it can be seen in Fig. 5.22 the slice emittance minimum does not correspond to the best matching of the slices which happens for 390 A according to the measurement result. This might be an indication of the beam slice emittance reaching its minimum due to

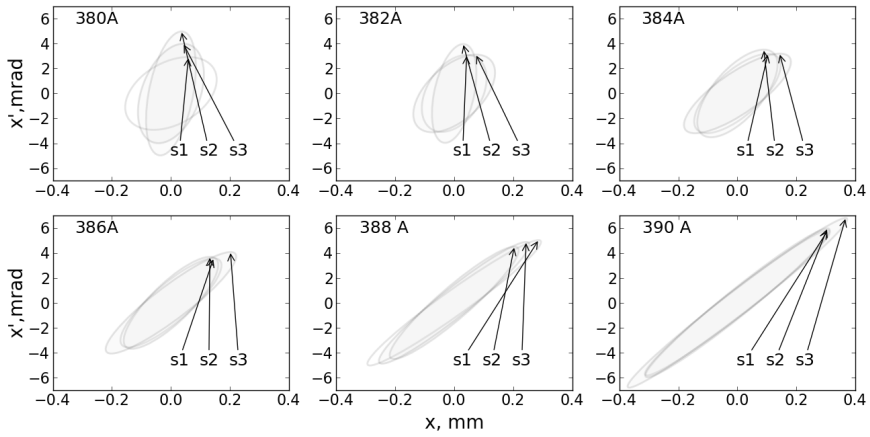


**Figure 5.22:** Slice equivalent ellipses in phase space for 230 pC.

non-linear processes at a different solenoid current when compared to the solenoid current for the best compensation of slice mismatch due to variable forces applied along the bunch. The projected emittance is affected by both and therefore will get its lowest value in between these two minima.

The effect was observed in simulations with much smaller difference in the solenoid current of the projected and slice emittance optima. There the shift depends on the bunch charge and can change the sign. For example in the simulation results demonstrated in section 5.1.2 the slice emittance has minimum at a higher solenoid current for 100 pC bunch charge, and at a lower solenoid current for 500 pC bunch charge. The larger difference in the experiment can be explained by the non-uniform laser spot at the cathode involving more non-linear effects.

The minimum measured slice emittance value is 0.52 $\pm$ 0.04 mm mrad at a solenoid current of 382 A and it is rather flat within the range 382-388 A of the solenoid current. The minimum projected emittance is 0.52 $\pm$ 0.02 mm mrad at a solenoid current of 392 A, but gets up to 0.59 mm mrad at the solenoid current of 382 A. In the simulation the absolute value of the projected emittance 0.33 mm mrad against 0.25 mm mrad of the slice emittance.

One needs to mention that the minimum projected emittance, 0.34 mm mrad, was measured with the RMS laser spot size of 0.18 mm and 379 A solenoid current. The simulation predicts the optimized projected emittance of 0.28 mm mrad for the laser spot size of 0.22 mm and 382 A solenoid

current. The slice emittance was not measured for this laser spot size.

Summarazing the variety of emittance numbers we conclude:

- Both the simulations and the projected emittance measurements predict the minimum slice emittance at smaller laser RMS spot sizes than 0.3 mm.
- The solenoid current value of the projected emittance minimum is shifted with respect to the slice emittance minimum. As it can be seen from the slices trace space orientation the projected emittance minimum is achieved at the best matching of the slices. It means if one obtains the minimum slice emittance and the best matching at the same solenoid current the projected emittance will be reduced for this laser spot size.
- The difference between measured and simulated projected and slice emittance values is not well understood. The numerical model includes only a flat-top longitudinal and homogeneous transverse laser profiles. The effect of profile modulations on the projected emittance was studied in simulations and has shown significant influence [44]. Simulations consider only a single bunch and that's why no parameter jitter is included. Another reason for the discripancy could be in an extremely simplified emission model. The simulations were done assuming a constant kinetic energy of the emitted particles and an isotropic emission from the cathode.

#### 5.2.2.4 Measurement # 6. Flat-top laser pulse temporal profile, 500 pC bunch charge, with an RMS laser spot size of 0.3 mm

A flat-top laser temporal shape with 1.94 ps, 21.35 ps, 2.64 ps corresponding to rise, FWHM, fall times was generated for this measurement. The transverse RMS laser spot size at the cathode is 0.30 mm in both x and y directions. The longitudinal and transverse shapes can be looked up in Appendix D.5.

The gun phase is set to maximum mean momentum of the beam. With this setup the mean momentum reaches 6.68 MeV/c and the RMS spread is about 20 keV/c. The booster phase is adjusted first to maximum mean momentum gain. With this phase the beam mean momentum equals 24.82 MeV/c. After that the phase is shifted to -30 degrees.

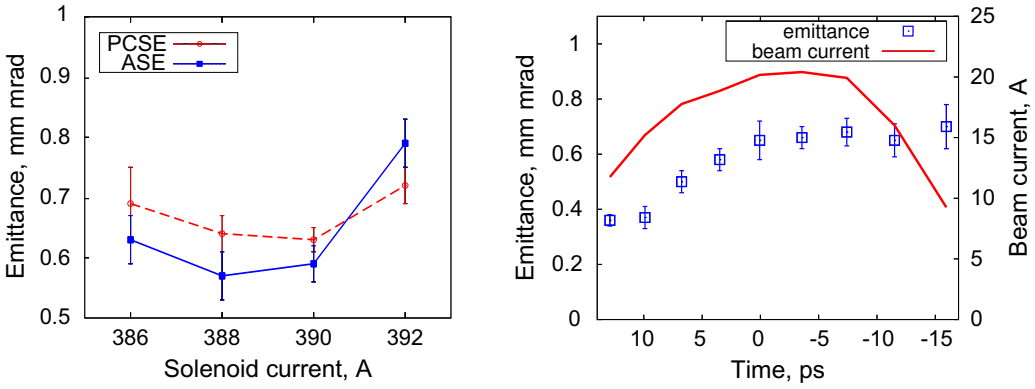


**Figure 5.23:** The measurement result of 500 pC, laser spot size 0.30 mm, $I_{main} = 390$ A.

The measurement is conducted using the quadrupole in front of the dipole (H1Q3). In the slice emittance solenoid optimization (Fig. 5.23(a)) a minimum is found at a solenoid current of 390 A. A detailed scan is performed with this solenoid current, the result is shown in Fig. 5.23(b). The peak current slice emittance equals to $0.66 \pm 0.04$ mm mrad, the average slice emittance is $0.59 \pm 0.05$ mm mrad.

Slice phase space orientations are presented in Fig. 5.24 for several main solenoid currents. Lets follow the change of the orientation with the solenoid current. With 386 and 388 A the slices look well aligned but the individual emittance values (area of the ellipse) are higher than for the next plot of 390 A. At 390 A one obtains the smallest slice emittance but the slice

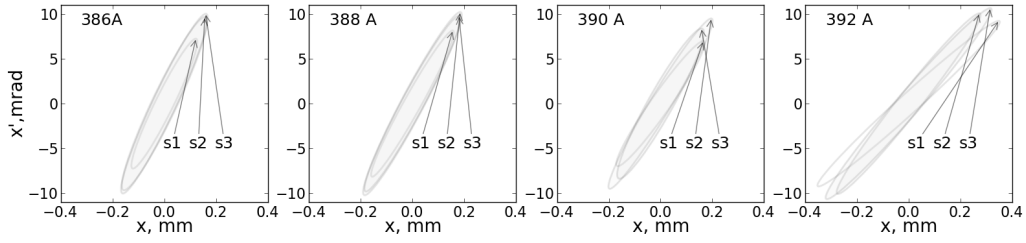


**Figure 5.24:** The solenoid scan resulting slice orientation 0.5 nC, laser spot size 0.3 mm.

orientation is apparently mismatched and gets even worse with 392 A (over-focusing). A similar behavior was already shown for in the scope of the beam dynamics simulations 5.1.2. For the measurement in the previous section the minimum slice emittance occurred for a lower solenoid current than the current of the best slice alignment.

Beam projected emittance measurements were not done with this bunch charge. In simulations the projected emittance minimum equals 0.43 mm mrad for this laser spot size at the solenoid current of 382 A. The slice emittance equals to 0.37 mm mrad. The slice emittance is significantly higher than the thermal emittance for this laser spot size (0.25 mm mrad) due to a growing role of the non-linear transverse space charge interaction. Keeping the same laser spot size at the cathode (thermal emittance) for different bunch charges one obtains the characteristics of the space charge contribution to the bunch slice emittance. The measurements are presented in the order of growing bunch charge. The same laser spot size was used for 230 pC, for 500 pC and for 1 nC (see next section). For 230 pC bunch charge with this laser spot size thermal emittance is totally dominant and therefore one needs to reduces the laser spot size to move toward the optimum slice emittance. 500 pC bunches have already a significant contribution of the non-linear space charge to the slice emittance and the optimum can occur for smaller as well as for larger laser spot sizes.

#### 5.2.2.5 Measurement # 7. Flat-top laser pulse temporal profile, 1 nC bunch charge, with an RMS laser spot size of 0.3 mm

First a projected emittance measurement with 1 nC bunch charge was done at EMSY1, which has shown the smallest value in X plane of 0.94 mm mrad for the laser RMS spot size of 0.3 mm, and the solenoid current 392 A. The same conditions were kept to measure slice emittance. The results are presented on Fig. 5.25. The peak current slice emittance value is $0.88 \pm 0.05$ mm mrad. The average slice emittance calculation results in $1.04 \pm 0.12$ mm mrad.

The simulation of the setup has shown that the maximum possible charge that can be extracted from the cathode with this small laser spot size is about 800 pC. The minimum RMS laser spot size which still allows to extract the full charge at 60 MV/m is 0.39 mm (no field induced emission included). In the projected emittance optimization using simulations for 1 nC beam the minimum was found to be 0.65 mm mrad with the RMS laser spot size of

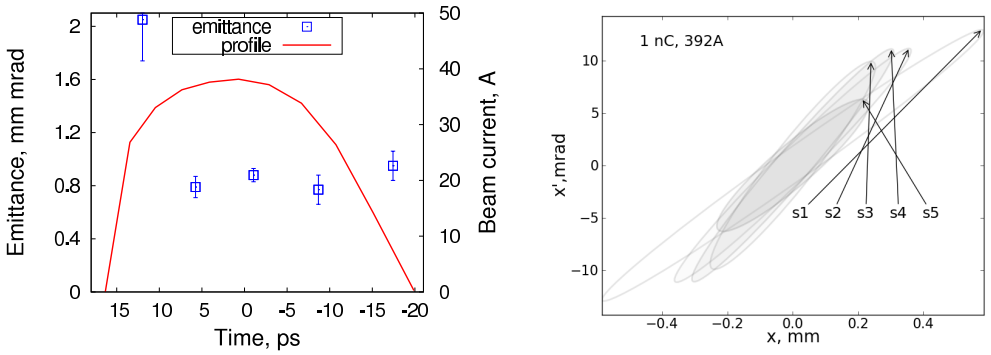


(a) (b)

**Figure 5.25:** The measurement result of 1 nC beam, laser spot size 0.30 mm, $I_{main} = 392$ A

0.41 mm mrad and the solenoid current of 383 A. The beam slice emittance minimum was obtained with the same spot size, but at 382 A solenoid current, and the value equals to 0.59 mm mrad. This result is about 25% lower than the measured value and the reasons for that are assumed to be the same as mentioned in section 5.2.2.3.

From the previous projected emittance measurements with low bunch charges one learns that the laser spot size corresponding to the minimum value is systematically lower than the one expected from the simulation. The reason can be in a difficult to detect low intensity halo of the laser beam. It would lead to a situation when the 1.2 mm diameter spot is saturated and does not emit more charge with more laser power, but in the halo region the extracted charge is growing. In this way the halo gets amplified in respect to the charge content of the main spot. It would make the effective laser spot size larger than measured with the virtual cathode. This assumption could explain the low intensity halo that is observed in the electron beam (see next section). The study of this subject is out of the scope of this thesis, but it is definitely of great importance for the beam characterization purposes.

### 5.2.3 Slice emittance measurement using slit scan

#### 5.2.3.1 Measurement # 8. Flat-top laser pulse temporal profile, 1 nC bunch charge, with an RMS laser spot size of 0.3 mm

The following measurement was performed for 1 nC bunches in the same conditions as the projected emittance measurement at EMSY1 and as the quad scan presented in the previous section ($I_{main}$ = 392A). The peak current slice emittance measured to be 1.49 mm mrad. The phase space distributions of slices (for example see Fig. 5.27(c)) were strongly divergent, the beamlet RMS sizes were about 100 $\mu$m, there was an intensity core observed in the phase space distribution that concentrates about 90% of the integral signal, although its transverse coordinate span is only half of the full beam. That means the contributions of the pixel RMS equivalent resolution (18 $\mu$m), optics resolution (40 $\mu$m), and the potential screen resolution (60 $\mu$m) are significant. These components are independent and have to be accounted quadratically to the electron beam size contribution.

The situation can be improved if the electron beam contribution is increased. This is realized by focusing the beam at the slit mask using a quadrupole right after the booster (H1Q1). The measured beam emittance changed significantly with the applied quadrupole focusing. Then the decision was made to measure the slice emittance as a function of the quadrupole current.

For each quadrupole current the emittance values of the same four slices were measured. The minimum emittance value appeared between 2.1 A (corresponds to the X beam size focus at the slit mask location) and 2.5 A of the quadrupole current. The scan curve in Fig. 5.26(a) shows the average slice emittance as a function of the quadrupole current. On Fig. 5.26(b) the emittance values of individual slices are shown for different quadrupole currents together with the beam current profile.

We see that the slice emittance measurement 70 cm downstream from the place, for which the emittance was reconstructed in the previous section, delivers twice higher results. First, we need to understand what is the reason for the emittance decrease caused by the quadrupole focusing. The role of the quadrupole focusing in this case is to induce a higher space charge interaction. The space charge performs a non linear transformation of the phase space distribution that reduces the RMS emittance at the position of EMSY2.

Fig. 5.27(a) and Fig. 5.27(b) show the beam transverse profiles on the

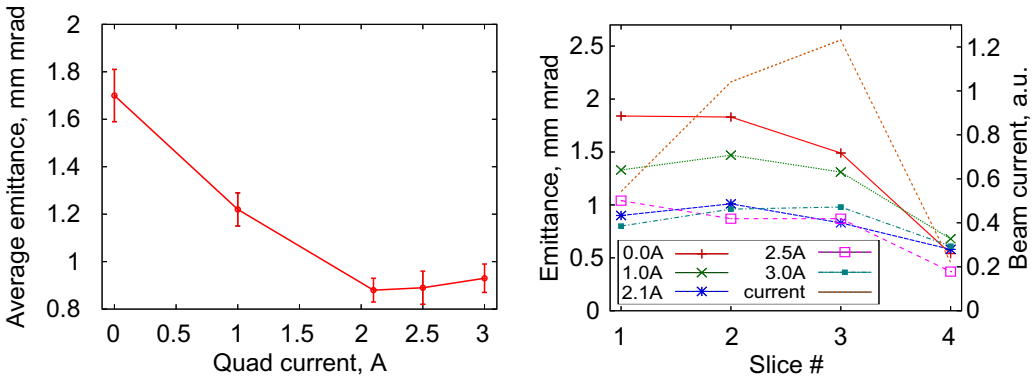


**Figure 5.26:** A quadrupole magnet focusing in front of the slit mask to minimize nonlinear correlated divergence contribution.

slit mask. When there is no quadrupole magnet applied the beam has a symmetric wing like pattern in X direction. The wings have considerably lower intensity. Now if one looks at the phase space distribution of the beam (Fig 5.27(c)) there is a linear distribution with a more intensive core and the periphery parts which correspond to the wings. Now one focuses the beam in x direction on the slit mask ($I_{quad} = 2.1\,A$). In the transverse profile there is still some halo but the wings are not so distinct. On the other hand in the phase space distribution (Fig 5.27(d)) these wings have the same X coordinate as the core part, but they are stronger divergent. In this configuration the phase space distribution forms an "s" like shape that has a smaller RMS emittance value. The most outer particles of the transverse profile cross the x=0 axis with the smallest impact from the transverse space charge. The core part particles do not cross the divergence axis. They are stopped and accelerated backwards by the space charge repulsion. The space charge impact grows from the outer particles toward the core, and particles loose their transverse momentum dependence on the transverse position. The phase space folds into a more compact distribution that has a lower RMS emittance. This situation can be observed in simulations and a simulated distribution similar to the measured one is shown in Fig. 2.5.

The assumption that the phase space distortion leads to the emittance reduction suggests that the original emittance is correct with no additional quadrupole applied. The phase space distribution has a 'banana' like shape and the RMS emittance value is not supposed to be applied in case of non-

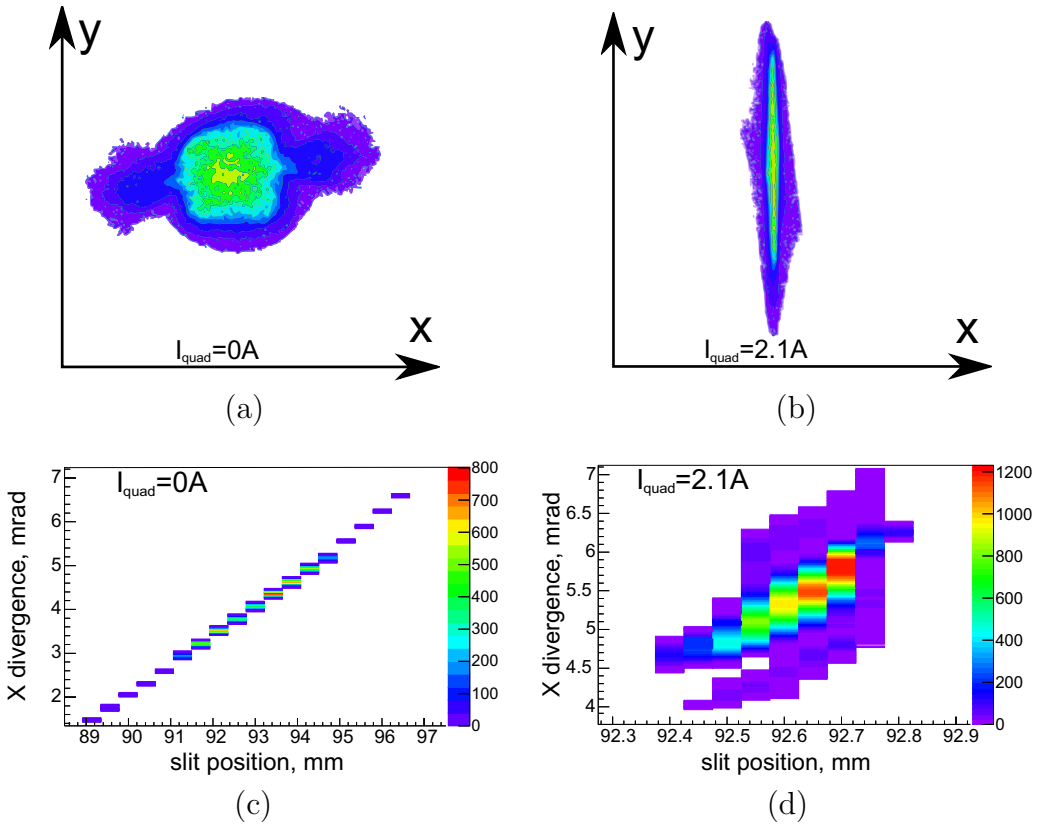


**Figure 5.27:** (a) and (b): transverse profiles of the beam for the H1Q1 quadrupole current of 0 A and 2.1 A correspondingly. (c) and (d): phase space distributions of the peak current slice for the quadrupole current of 0 A and 2.1 A correspondingly.

linear distributions. After the distribution from Fig 5.27(c) is linearized by shearing along the divergence axis the RMS emittance reduces from 1.83 mm mrad to 1.71 mm mrad, meaning that the non-linearity contribution does not dominate the result.

On the other hand the emittance value with the quadrupole current of 2.1 A approaches the results of the quadrupole scan presented in the previous section. In the emittance quadrupole scan one focuses the beam on the observation screen and measures the beam sizes. But the focused distribution might undergo the similar non-linear transformation, the size scan delivers only the information about the distorted phase space. The quadrupole scan with 1 nC illustrates exactly this case, although the simulation described in

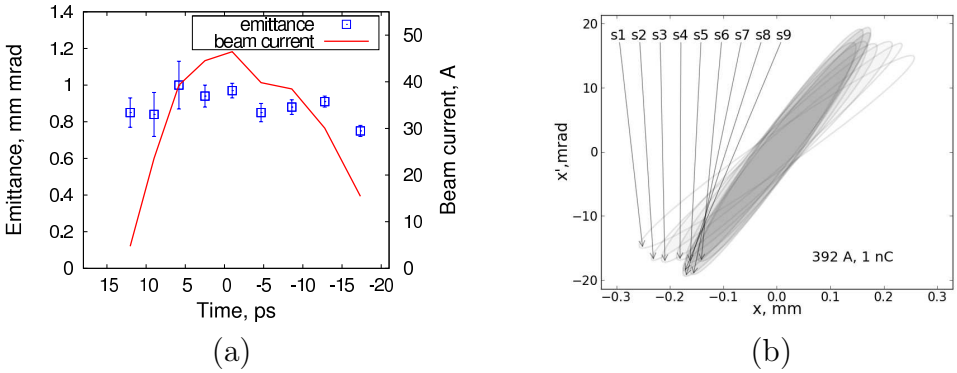


**Figure 5.28:** Detailed slice emittance measurement with 1 nC using the slit scan technique. (a) Slice emittance versus time within the bunch. (b) Equivalent ellipse phase space distributions of the slices

section 5.1.3 has not shown any effect of the space charge. The idea was confirmed by comparing the Twiss parameters obtained in the quadrupole scan (previous section) and those of the slit scan. The best matching of the parameters is achieved when the beam has a focus at EMSY2 for the slit scan.

A detailed slice scan was then performed with the quadrupole current 2.5 A, which had shown slightly higher emittance but better signal to noise ratio. The results are shown on Fig. 5.28. The left plot represents emittance as a function of time. The peak current slice has an emittance value of $0.97 \pm 0.04$ mm mrad. The right plot is a qualitative schematics of the slices orientation in phase space.

The low intensity halo observed in Fig. 5.29(a) contains only about 10% of the bunch charge. But we are interested in its contribution to the emittance. The emittance can be represented as a function of the charge cut, which is described below. Every pixel in phase space that has a value lower than a certain threshold is set to zero, what corresponds to skipping the charge out of an equal charge density contour. The bunch emittance as a function of the fraction of the discriminated bunch charge for the peak current slice distribution is shown on Fig. 5.29 together with the 100% charge phase space distribution. The emittance values 0.97 mm mrad, 0.79 mm mrad, 0.65 mm mrad are corresponding to 100%, 95% and 90% of the charge considered in the reconstructed phase space distribution. Here one concludes that the halo containing 10% of the charge is responsible for about 30% of emittance.

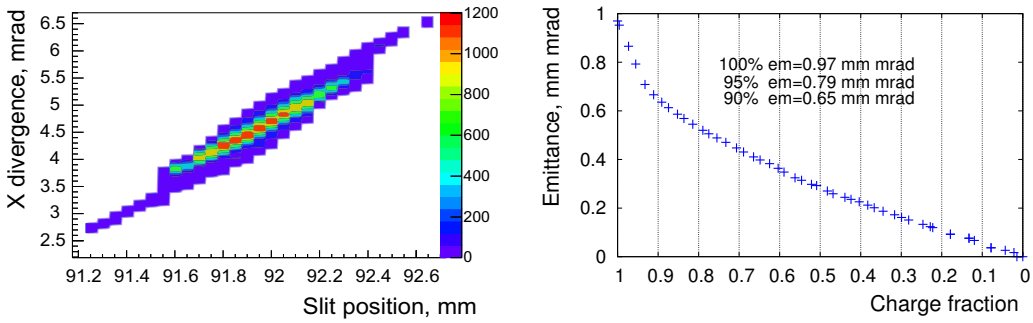


(a) (b)

**Figure 5.29:** The phase space of the peak current slice and the corresponding charge cut curve.

The slit scan technique suffers from low intensity beamlets on the beam edge, where the charge passing the slit is already tiny and then it is spread over a certain area on the observation screen, and the distribution appears to be fully below the sensitivity threshold of the system. The level of the distribution tails discrimination can be figured out by comparing the RMS beam size on the screen at EMSY2 of 0.28 mm and the size of the profile (Fig 5.30(a)) reconstructed from the integrated intensity of distribution[2] on the observation screen in HEDA1 that equals to 0.22 mm. Now a charge cut is applied to the beam transverse profile at the EMSY2 screen similar to the phase space distribution cut described above. The aim is to estimate the fraction of the initial beam charge that is included in the reconstructed phase space distribution. Fig. 5.30(b) shows the cut and one gets equal sizes when 5% of the charge are discriminated.

#### 5.2.3.2 Beam projected emittance measurement using slit masks of different widths

The above described slice emittance measurement is performed using a 50 $\mu$m slit. The projected emittance the section referres to is measured with 10$\mu$m slit. In order to compare the results an additional experiment was done. The projected horizontal emittance was measured using EMSY2 with both slit masks of 10 and 50 $\mu$m. High1.Scr5 positioned 1.8 m downstream was used as the observation screen. The camera settings were adjusted to have

[2]integrated along horizontal divergence spread and over all slices.

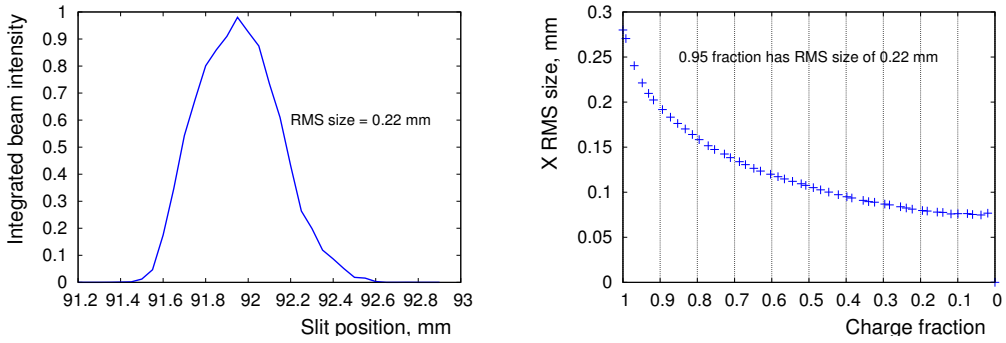


(a) (b)

**Figure 5.30:** Estimation of the tails loss for the slit scan technique. (a) The beam X transverse projection at the EMSY2 position reconstructed from the slit scan. (b) The original X transverse profile size at EMSY2 screen as a function of the charge remaining after the charge density below a certain level is discriminated.

the maximum peak intensity in both cases for about the same number of pulses. For the 10 $\mu$m case 15 pulses were used, 2x2 binned mode of the camera, the camera gain 20. For the 50 $\mu$m case 20 pulses were used, full frame mode of the camera, the camera gain 10. The resulting phase space distributions are presented in Fig. 5.31.

The emittance measured with the 10 $\mu$m slit mask equals 0.7 mm mrad and the reconstructed beam size in the phase space is 40% smaller than the size resulting from a direct measurement at the EMSY2 screen; with the 50 $\mu$m slit mask the measured emittance equals 1.71 mm mrad and the phase space beam size is 7% smaller than the measured size at EMSY2.

The first visual difference found is a significant low intensity halo, measured with the 50 $\mu$m slit mask. Integrally the halo charge is about 30% of the full bunch charge, but it contributes the difference between the 10$\mu$m and the 50 $\mu$m slits in emittance value ( almost 2.5 times). Another fact that supports the halo existence is the factor between the reconstructed and the directly measured beam sizes at EMSY2, which is smaller for the 10 $\mu$m slit mask case due to the halo discrimination.

The final beamlet RMS size is between 100 $\mu$m and 200 $\mu$m for the 10 $\mu$m slit mask, and between 100 $\mu$m and 300 $\mu$m for the 50 $\mu$m slit mask. The initial slit size contribution is about 1% for the wider slit and is negligible

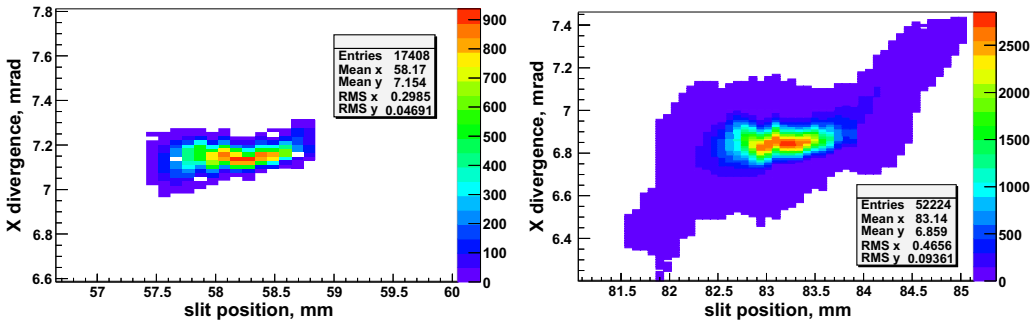


(a) (b)

**Figure 5.31:** Phase space distribution resulting form the slit scan measurements with (a) 10 $\mu$m slit and (b) 50 $\mu$m slit.

for the narrower slit.

A disadvantage of the wider slit is of course more space charge influencing the finally measured divergence distribution. In the simulations one obtains for similar beamlets that the difference caused by space charge between the beamlet sizes after the slit masks at the observation screen is about 1%. Even if the wider divergence spread in the central part is caused by the space charge, it cannot explain the charge appearing at the edges of the slit position scan range for the 50 $\mu$m slit mask.

There is still an argument that the measurements were done with quite different camera settings. Higher gain can lead to low signal discrimination if the camera is damaged by the radiation (see section 4.5.1). But this was not the case. The effect that switching from the binned mode to the full frame was observed to reduce the measured beam size due to the lower signal, is again not an explanation because lower sensitivity is compensated by higher intensity from the screen.

With this experiment it was found that the 50 $\mu$m slit mask is more sensitive to the low intensity halo unlike the projected emittance measurements that were done using the 10 $\mu$m slit mask at EMSY1. The halo phase space distribution is non-linear and therefore RMS emittance does not deliver a comparable value. Shearing of the distribution results in an RMS emittance value of 1.45 mm mrad.

### 5.2.4 Summary: different charge with RMS laser spot size at the cathode of 0.3 mm

Three measurements with 230, 500 and 1000 pC were conducted with the same laser spot size at the cathode (0.3 mm) and using the same quadrupole scan approach. The thermal emittance is assumed to be the same, the emittance changes only due to a difference in the space charge impact. This study should give an idea on how the electron beam brightness changes with the bunch charge.

Fig. 5.32 shows the peak current slice emittance as a function of its current. The experimental points from left to right correspond to 230 pC, 500 pC, and 1 nC. The data is fitted using the square root function. The electron beam brightness is constant along the curve, if the slice emittance is assumed to be equal in both transverse planes. The space charge induced emittance growth with the slice current in such a way that the brightness stays constant. One can still increase the beam brightness for 230 and 500 pC by reducing the laser spot size on the cathode. The presented data and the fit curve cover a certain range where the edge effects could not be observed. From the lower current side the emittance should go down only to the level of the thermal emittance. From the higher current side the emittance will start growing rapidly due to virtual cathode formation near the cathode surface. Even further it will not be possible to increase the current by increasing the laser pulse energy. For completeness of the study one needs more measurements especially for these both edges of the range.

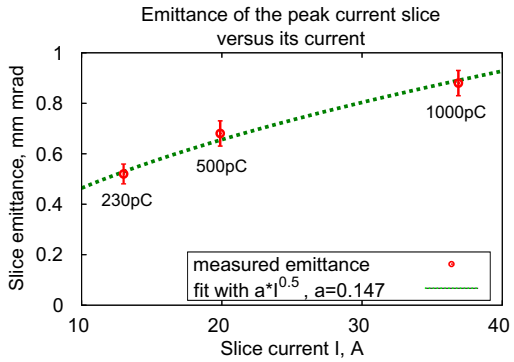


**Figure 5.32:** Summary of slice emittance measurements with different charge for an RMS laser spot size of 0.3 mm.

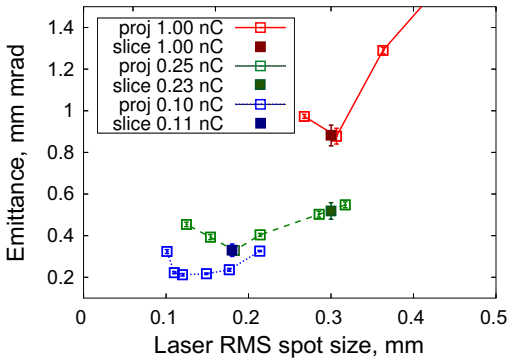


**Figure 5.33:** Summary of projected emittance results with different charge and peak current slice emittance results.

### 5.2.5 Summary: slice versus projected emittance

A set of projected emittance measurements [41] was done with similar to slice emittance conditions (gun on-crest). Fig. 5.33 summarizes the results of both types. The main difference is that the full projected emittance optimization is done and that the slice emittance was measured with one laser spot size per bunch charge only. For 110 pC the slice emittance result is higher than the projected values. Systematical errors are caused by strong laser transverse profile modulations in case of the slice emittance measurement with 0.1 nC (emittance increase), and by the usage of the 10 $\mu$m slit scan in case of projected emittance that has proved to be insensitive to low intensity halo (emittance decrease). Another systematical difference is that for the slice emittance measurements with 1 nC and 0.23 nC a new iris diaphragm aperture was used that allows to have any diameter within its range, but the shape is not strictly round. It is formed by 14 overlapping blades, which create a circle like transverse profile with 14 corners connected by almost straight lines. On the other hand no evidence of an effect on emittance was found in simulations.

### 5.2.6 Summary: the quadrupole and slit scans, 1 nC bunch charge

Measurements # 7 and # 8 were conducted using 1 nC bunches at the same phase off-crest, but with two different approaches. In this summary the results are compared and discussed.

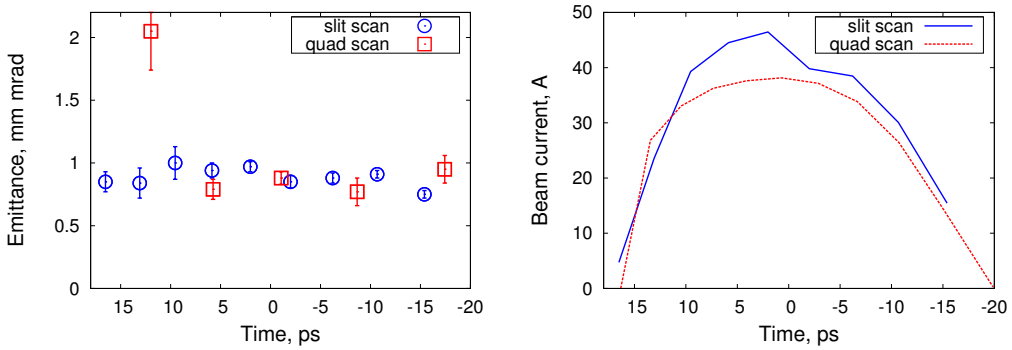


(a) (b)

**Figure 5.34:** Comparison of quadrupole scan and slit scan results for 1 nC.

Fig. 5.34 presents the data at the same plots. One can see that one point of the quadrupole scan is equal to the slit scan measurement within the statistical error, two quadrupole scan points lie 15% lower, and the edge points are higher than it is measured with the slit scan. The slit scan results represent the emittance of 95% of the bunch initial charge, as it was estimated above. There is no decent estimation for such an effect during the quadrupole scan. A general consideration is that the bunch charge is focused and low intensity of the beam distribution tails will exceed the system sensitivity threshold, keeping the intensity ratio between the tails and the core. If there is an effect it must be much smaller compared to the slit scan.

One of the systematical impacts that influences both methods is the space charge. It is contributing differently to both approaches though. In the slit scan data the measured divergence is overestimated by 3-6% (results of ASTRA simulations) due to the residual transverse space charge interactions in the drift between the slit mask and the screen. In case of the quadrupole scan the space charge modifies the beam size versus the quadrupole magnet current dependence. The plot in Fig. 5.14 explains the cases when emittance can be underestimated or overestimated. The beam size error due to the space charge observed in the simulations was up to 3%.

Another systematical error is caused by the limited temporal resolution of the setup. In the simulation section 5.1.3 an estimation of this effect for the quadrupole scan was done. It was shown that the peak current slice

emittance error depends on the solenoid current and is in the range from 2 to 20% for the off-crest phase of -30 degrees, where the minimum error corresponds to the minimum measured slice emittance in the solenoid scan.

During the slit scan studies it was found that emittance was changing with the focusing applied in front of the slit mask. Due to the introduced focusing the beam undergoes a non-linear transformation in the drift from the quadrupole to the slit mask. The space charge makes the phase space distribution more compact in the sense of RMS emittance. But this minimum has nothing to do with the projected emittance measured at EMSY1. In case of the quadrupole scan measurement the phase space distortion can not be avoided. This can be proven by measuring the emittance with the quadrupole (H1Q3) scan for several currents of the pre-focusing quadrupole (H1Q1) used in the case of the slit scan. If the assumption is correct there must be no difference in the emittance numbers, only the minimum of the size will be shifted along the quadrupole current.

The slit scan approach is a direct measurement and it allows to reconstruct the phase space distribution without modifying it. The disadvantages are: low intensity, mechanically comprehensive measurement setup. In the quadrupole scan the beam is always focused and generates enough signal even for low bunch charges down to 100 pC. In general the quadrupole scan can be extended to perform a tomographic reconstruction of the phase space distribution. The implementation requires a detailed study of the space charge influence on the reconstruction. Due to space charge the parameters can vary within the quadrupole scan itself causing an emittance uncertainty and faking the phase space distribution.

The results of both measurements differ 10-15% for 1 nC case, what is beyond the statistical error bars and might indicate some systematical error that is unknown yet.

# Chapter 6

# Summary and outlook

## 6.1 Summary of slice emittance studies

The possibility to measure slice emittance using an energy-chirped beam in a dispersive section was studied and the slice emittance diagnostics was implemented and successfully commissioned at PITZ. The setup allows to measure horizontal emittance only. The new recently installed dispersive section (HEDA2) will allow the measurements of the vertical transverse slice emittance in future.

The studies have shown that in the nominal operation mode with a beam duration of about 20 ps for a 1 nC bunch the setup RMS resolution can reach down to 1.5 ps (-50 degrees off-crest phase in the booster). The simulations of the setup predict that the minimum measured slice emittance should only slightly depend on the booster phase and on the measurement position along the setup in a certain range. This means one can compare the measurements done using the slit masks at EMSY1 and EMSY2 with the measurements done using the quadrupole magnets in front and after the dipole. One might still encounter different systematical errors at different measurement locations.

During the commissioning phase the depth of focus problem did not allow to make a reliable measurement using the slit scan technique. Therefore a new optical read-out was designed based upon the Scheimpflug rule to avoid the depth of focus issue.

The beam size were expected to be down to 20 $\mu$m in the quadrupole scan process, but the minimum beam size obtained experimentally was about 60 $\mu$m. A space charge influence was not observed in simulations, which

does not exclude that it is present in the experiment. Still several laboratories have reported an unexpected resolution limitations of YAG screens. Therefore it was decided to use a more distant quadrupole, the one in front of the 180°dipole. In this case the minimum size is about 100$\mu$m. In order to study the YAG resolution problem one can use the OTR screen, but the intensity was 10-20 times lower compared to the YAG screen. A wire scanner needs to be considered as an appropriate candidate for these studies.

The emittance optimization was first done using ASTRA simulations. They showed that the slice emittance optimum is usually close to the projected emittance optimum in the parameter space of the solenoid current and the laser spot size. The simulations were conducted for the PITZ setup with the CDS booster and showed very week dependence of the lowest emittance on the booster gradient in the range from 15 to 25 MV/m. From simulations with 1 nC bunches the average slice emittance is expected to be only 6% lower than the corresponding projected emittance in the optimum case.

A set of measurements was done using the quadrupole scan for different bunch charges. It showed that that the slice mismatch minimum along the solenoid current is shifted with respect to the solenoid current of smallest individual slice emittance. In case both effects occur at the same solenoid current the resulting projected emittance will be lower.

The set of measurements with constant laser RMS spot size of 0.3 mm for different bunch charges led to the conclusion that the slice emittance versus peak current follows a constant brightness curve[1]. The slice emittance optimum for the bunch charges of 500 and 230 pC is expected to be at lower laser spot sizes, meaning that the optimum beam brightness increases from 1 nC towards 230 pC bunch charge.

The systematical differences between the slice and the projected emittance setups were studied. Among them is the different width of the slit for the scans: 10 $\mu$m for the projected emittance and 50 $\mu$m for the slice emittance. It was observed that the 50 $\mu$m slit was more sensitive to the low intensity beam halo, which was strongly suppressed when the 10 $\mu$m slit was used. Although the halo contains about 30% of the integral signal in the phase space, the emittance of the distribution obtained with the 50 $\mu$m slit is about 2.5 times higher.

The quadrupole scan data shows lower emittance for 1 nC bunch charge than the slit scan without any additional focusing applied. The slit scan was also conducted with an assisting quadrupole. A strong dependence of

[1]with the assumption that the emittance is equal in both transverse planes.

the emittance on the quadrupole current was observed. The Twiss parameters obtained in the slit scan and the quadrupole scan coincide when the beam is focused with the additional quadrupole on the slit mask. From this result it was concluded that the beam experience a non-linear deformation by the space charge in the quadrupole scan measurement and a set of modified Twiss parameters in front of the quadrupole is obtained. The resulting emittance is by chance comparable with the projected emittance values measured without the halo.

In the scope of the halo studies we encountered strong phase space non-linearities which increase the RMS emittance. As a consequence the average phase space charge density is considered as reduced, although the peak phase space charge density stays the same. Regarding this issue one can apply a phase space shearing procedure to exclude non-linearities. Still this solution is not applicable for strongly non-linear (containing loops) distributions. One can also discriminate the low intensity non-linear part of the phase space distribution. In this manner the RMS emittance value is acceptable for the average phase space charge density calculation of the beam core.

The halo needs further investigations as well as dedicated instrumentation. There were several possibilities studied in other labs, e.g. [69].

The results obtained at PITZ can be compared to the similar experiments of SPARC [10] and SLAC [9] groups. The SPARC team has obtained a slice emittance of 1.3 mm mrad applying a deflecting cavity and quadrupole scan technique for the bunch charge of 300 pC at the beam energy of about 150 MeV. At SLAC the measurement was performed using energy-chirped bunches in a dispersive section. The bunch emittance was measured using quadrupole scan technique and the result for 300 pC bunch charge was in a range of 1-3 mm mrad. At the PITZ measurement setup the slice emittance values in a range of 0.8-2 mm mrad were obtained for the 1 nC bunches.

## 6.2 Future of slice emittance diagnostics at PITZ

Beam slice emittance at the gun output is of essential interest for FELs with a linear bunch compression, especially for HGHG scheme. The gun contribution to the beam emittance at the undulators is the major one. Therefore characterization of the slice emittance allows to obtain the lower limit of the emittance contribution and to distinguish between the emittance

optimization goals: the best slice matching and the lowest individual slice emittance.

It's worth to mention that this simple diagnostics should provide a possibility to measure thermal emittance with long bunches. Normally, it is done using the slit scan in the straight section with a short Gaussian bunch to minimize the RF field contribution, and with very low charge to exclude space charge as much as possible [70].

For slice emittance measurements with higher longitudinal resolution one can apply a transverse deflecting cavity that among other diagnostics based on it allows high temporal resolution slice emittance measurements of the electron beam without a need to introduce additional energy spread. A deflecting cavity system is under installation at PITZ right now. A comparison of both methods will be an important option, as the comparison of the current setup up to now is only done with respect to simulation results which show significant differences.

# Appendix A

## A.1 Solenoid calibration and emittance compensation and emittance double minima

The field to current calibration for the solenoid is a linear function with two parameters c=0.0005889 and d=0.00007102:

$$I = cB + d \tag{1.1}$$

### A.1.1 Emittance double minima

The solenoid current is 372A. The RMS projected emittance evolution along the z axis is shown in Fig. A.1. The compensation occurs first at about 3 m (Fig. A.2) and the second time at 8 m (Fig. A.3), although the second emittance minimum occurs at about 7 m. The difference can be explained by the growth of the individual slice emittance due to the non-linear transformation.

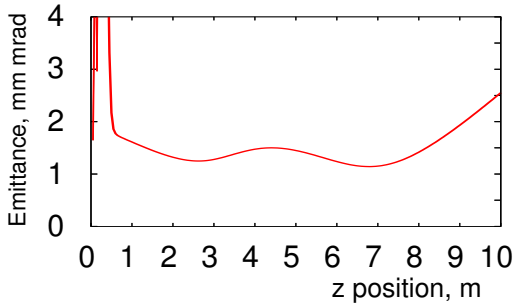


**Figure A.1:** Emittance as a function of the longitudinal coordinate along the setup.

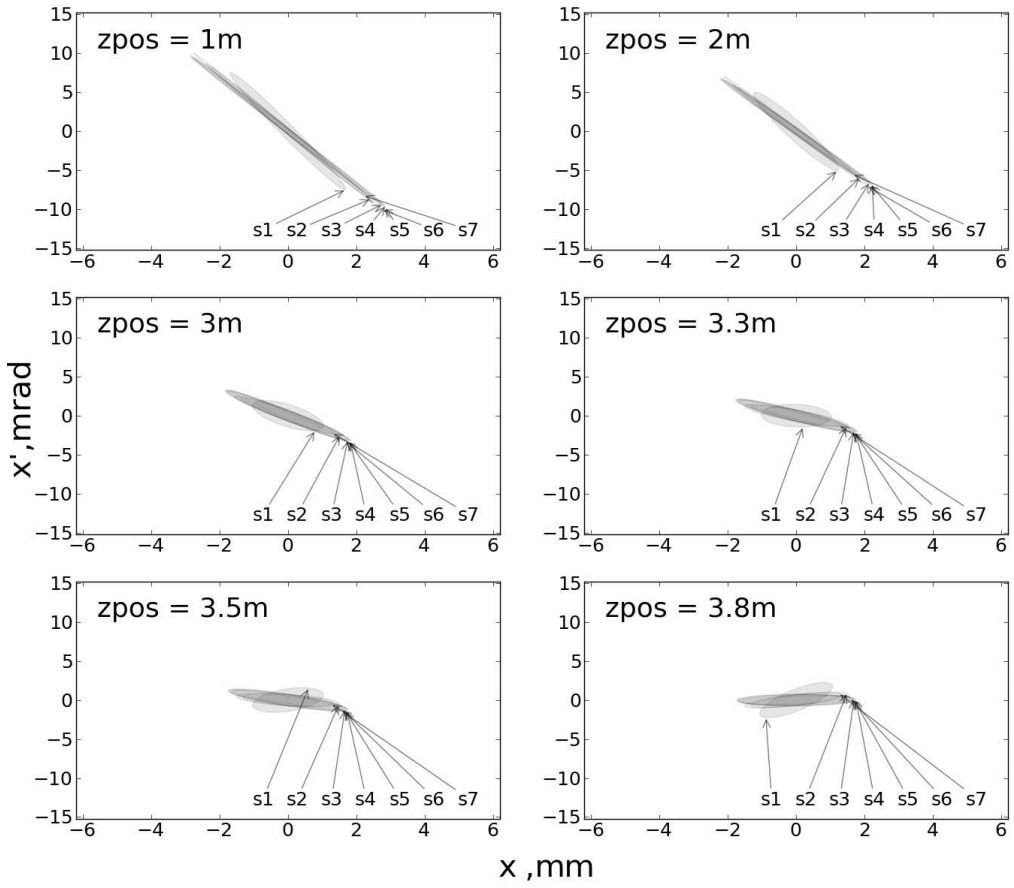


**Figure A.2:** The array of the phase spaces shows the evolution of slices' distributions along the beamline. First projected emittance minimum.

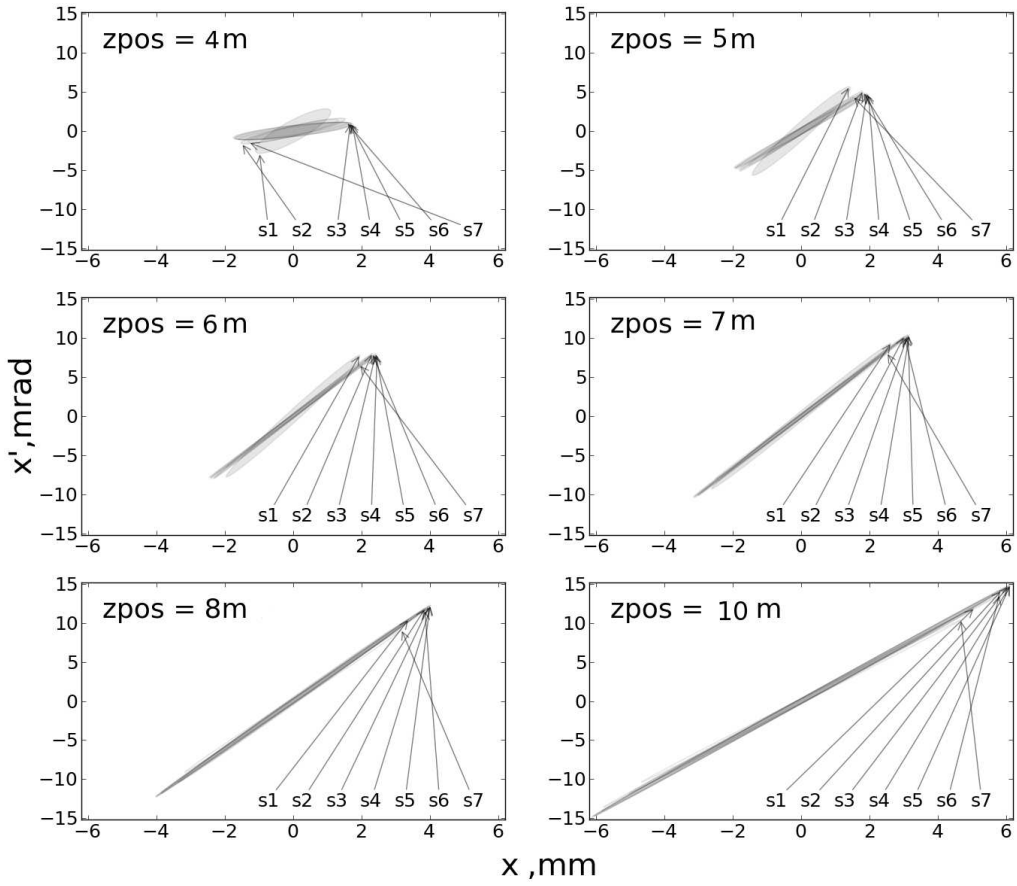


**Figure A.3:** The array of the phase spaces shows the evolution of slices' distributions along the beamline. Second projected emittance minimum.

# Appendix B

## B.1 Slice emittance setup parameters

| measurement type | slit (quad) position | drift before the dipole | drift after the dipole | full drift |
|---|---|---|---|---|
| slit scan (EMSY2) | 7125 | 375 | 1950 | 3260 |
| quad scan (H1Q3) | 6780 | 720 | 1950 | 3606 |
| quad scan (D2Q1) | 6757 | - | 1207 | 1207 |

The quadroupole gradient dependence on the current is described by: $G = a \cdot I + b$. The function describes a linear part of the hysteresis curve coming from field saturation down to zero.

| Quadrupole | Effective length, mm | Maximum gradient, T/m | a, T/m/A | b, T/m |
|---|---|---|---|---|
| High1.Q3 | 43 | 7.0 | 0.73 | -0.29 |
| Disp2.Q1 | 226 | 2.0 | 0.12 | -0.01 |

# Appendix C

## C.1 Quadrupole scan simulation schematics

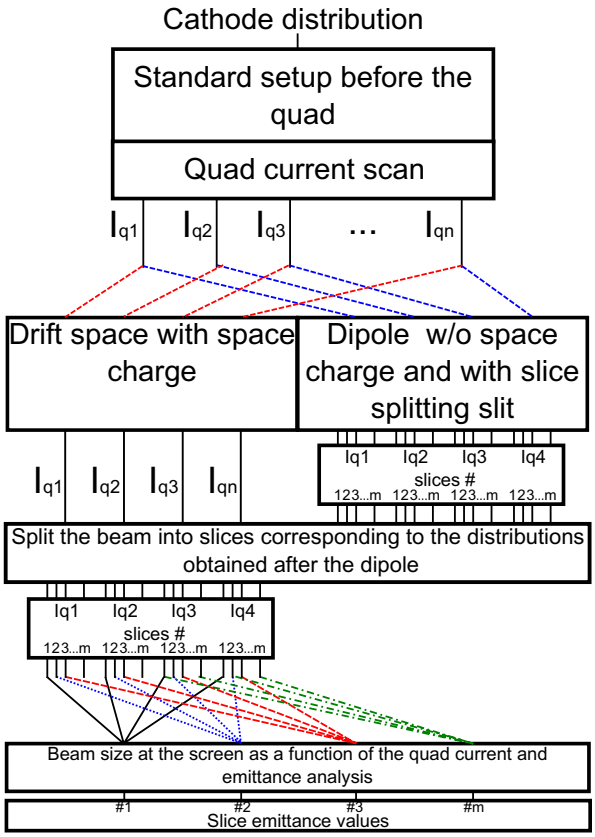


**Figure C.1:** A scheme of emittance measurement procedure simulation using a quadrupole scan

# Appendix D

## D.1 Laser pulse shapes for different measurements

This appendix contains the laser temporal and transverse profiles with horizontal (blue line) and vertical (red line) cuts through the center of transverse distributions for the sets of experimental results obtained in this work.

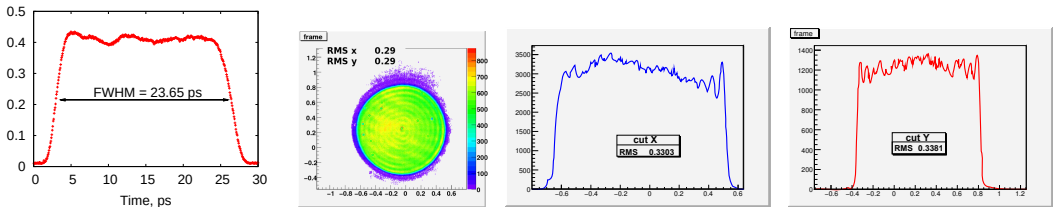


**Figure D.1:** Measurement ID 1

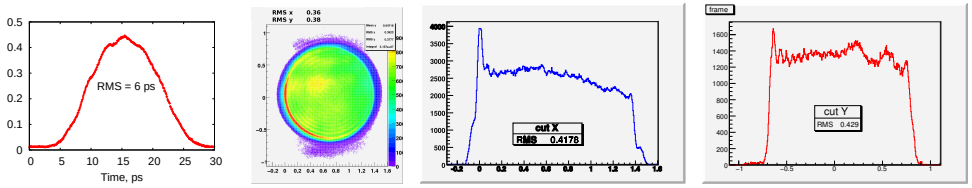


**Figure D.2:** Measurement ID 2

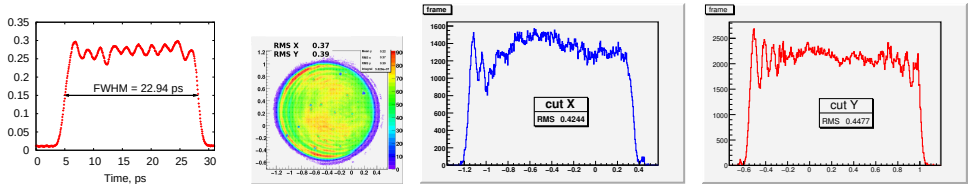


**Figure D.3:** Measurement ID 3

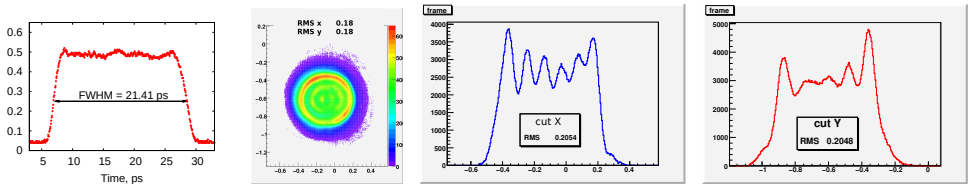


**Figure D.4:** Measurement ID 4

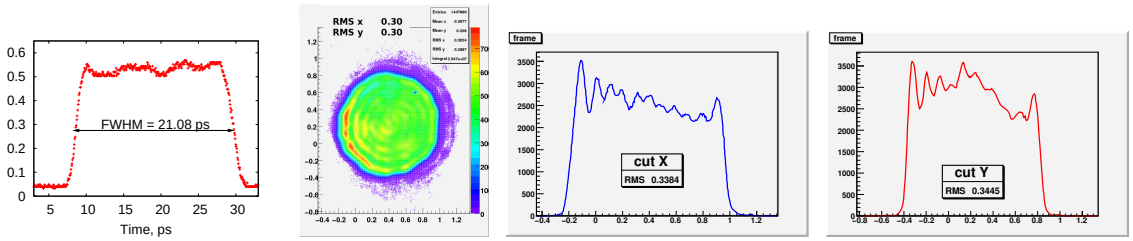


**Figure D.5:** Measurement ID 6

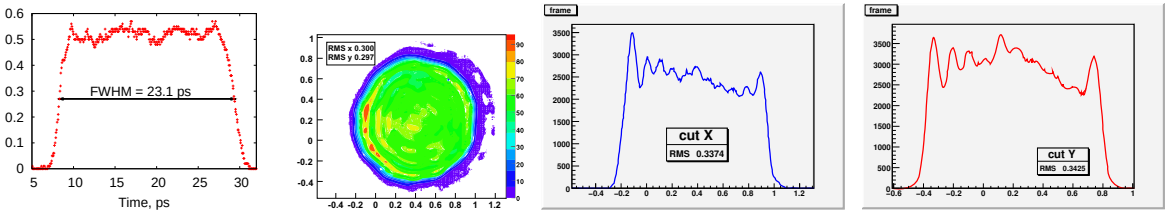


**Figure D.6:** Measurement ID 5 and ID 7

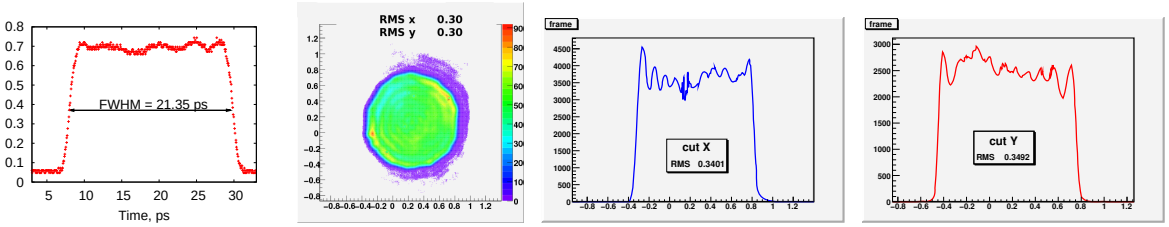


**Figure D.7:** Measurement ID 8

# Bibliography


[1] W. Ackermann et al., *Nature Photonics* **1**, 336 (2007).

[2] P. Emma et al., First lasing of the LCLS X-Ray FEL at 1.5 Å, Technical report, SLAC, 2009.

[3] T. Shintake and SCSS group, Status of the SCSS test accelerator and XFEL project in Japan, in *Proceedings of EPAC06*, Edinburgh, UK, June 2006.

[4] S. Liu et al., Generation and acceleration of high brightness electron bunch train at ATF of KEK, in *Proceedings of PAC07*, Albuquerque, New Mexico, USA, June 2007.

[5] M. Hernandez et al., Emittance measurements for the SLAC gun test facility, in *Proceedings of PAC97*, Vancouver, B.C., Canada, May, 1997.

[6] BNL ATF project web-page, http://www.bnl.gov/atf/.

[7] R. Ganter et al., *Phys. Rev. ST Accel. Beams* **13**, 093502 (2010).

[8] F. Stephan et al., *Phys. Rev. ST Accel. Beams* **13**, 020704 (2010).

[9] D. Dowell et al., Analysis of slice emittance measurements for the SLAC gun test facility, in *Proceedings of PAC03*, 2003.

[10] C. Vaccarezza et al., Slice emittance measurements at SPARC photoinjector with a RF deflector, in *Proceedings of EPAC08*, 2008.

[11] L. Staykov, *Characterization of the transverse phase space at the photo-injector test facility in DESY Zeuthen site*, PhD thesis, Universität Hamburg, 2008.

[12] S. Rimjaem et al., Study of transverse projected emittance for different bunch charges at PITZ, in *Proceedings of FEL10*, Malmö, Sweden, August 2010.

[13] M. Reiser, *Theory and Design of Charged Particle Beams*, WILEY-VCH Verlag, 2008.

[14] K. Wille, *The Physics of Particle Accelerators*, Oxford University Press, 2000.

[15] K. Floettmann, *Phys. Rev. ST Accel. Beams* **6**, 034202 (2003).

[16] J. Buon, Beam phase space and emittance, in *Proceedings of CERN ACCELERATOR SCHOOL*, 1992.

[17] M. S. D. Edwards, *An Introduction to the Physics of High Energy Accelerators*, John Wiley and sons, 1993.

[18] C. A. Brau, What brightness means, in *Proceedings of ICFA Workshop: The Physics and Applications of High Brightness Electron Beams*, Chia Laguna, Sardinia, Italy, July 2002.

[19] S. Lederer et al., Investigations on the Thermal Emittance of $Cs_2Te$ Photocathodes at PITZ, in *Proceedings of FEL07*, Novosibirsk, Russia, 2007.

[20] K. Steffen, *High Energy Beam Optics*, Interscience, 1965.

[21] L. Landau and E. Livshitz, *Teoreticheskaja fizika. Tom 2: Teorija polja*, Nauka, 1988.

[22] B. Carlsten, *Nuclear Instruments and Methods in Physics Research Section A: Accelerators, Spectrometers, Detectors and Associated Equipment* **285**, 313 (1989).

[23] T. Naito and T. Mitsuhashi, *Phys. Rev. ST Accel. Beams* **9**, 122802 (2006).

[24] M. Masaki and S. Takano, Beam size measurement of the SPring-8 storage ring by two-dimensional interferometer, in *Proceedings of DIPAC01*, 2001.

[25] J. Krider, *Nuclear Instruments and Methods in Physics Research Section A: Accelerators, Spectrometers, Detectors and Associated Equipment* **278**, 660 (1989).

[26] S. T. Boogert et al., *Phys. Rev. ST Accel. Beams* **13**, 122801 (2010).

[27] T. Shintake, *Nuclear Instruments and Methods in Physics Research Section A: Accelerators, Spectrometers, Detectors and Associated Equipment* **311**, 453 (1992).

[28] G. Kube, Resolution studies of inorganic scintillation screens for high energetic and high brilliant electron beams, in *Workshop on Scintillating Screen Application in Beam Diagnostics*, Darmstadt, Germay, 2011.

[29] A. Murokh et al., Limitations on measuring a transverse profile of ultra-dense electron beams with scintillators, in *Proceedings of PAC01*, Chicago, Illinois, USA, June 2001.

[30] B. Gitter, Optical Transition Radiation, Technical report, UCLA Department of Physics, 1992.

[31] X. Artru, M. Castellano, L. Catani, R. Chehab, D. Giove, K. Honkavaara, P. Patteri, M. Taurigna-Quere, A. Variola, and L. Wartski, *Nuclear Instruments and Methods in Physics Research Section A: Accelerators, Spectrometers, Detectors and Associated Equipment* **410**, 148 (1998).

[32] S. Rimjaem, Screen investigations for low energetic electron beams at PITZ, in *Workshop on Scintillating Screen Application in Beam Diagnostics*, Darmstadt, Germay, 2011.

[33] A. Lumpkin et al., Spatial resolution limits of YAG:CE powder beam-profile monitors at the Fermilab A0 photoinjector, in *Proceedings of FEL09*, Liverpool, UK, August 2009.

[34] M. Yan, Influence of observation geometryon resolution for beam profile measurements using scintillation screens, in *Workshop on Scintillating Screen Application in Beam Diagnostics*, Darmstadt, Germay, 2011.

[35] T. Scheimpflug, Improved Method and Apparatus for the Systematic Alteration or Distortion of Plane Pictures and Images by Means of Lenses and Mirrors for Photography and for other purposes, British Patent, 1904.

[36] G. Asova, *Tomography of the electron transverse phase space at PITZ*, PhD thesis, 2011.

[37] FLASH project web-page, http://flash.desy.de/.

[38] European XFEL project web-page, http://www.xfel.eu/.

[39] M. Altarelli and Deutsches Elektronen-Synchrotron (Center). X-Ray Free-Electron Laser Project, *XFEL: the European X-ray free-electron laser : technical design report*, DESY (Series), DESY XFEL Project Group, 2006.

[40] S. Rimjaem et al., Generating low transverse emittance beams for linac based light sources at PITZ, in *Proceedings of IPAC10*, Kyoto, Japan, May 2010.

[41] S. Rimjaem et al., Measurements of transverse projected emittance for different bunch charges at upgraded PITZ facility, in *Proceedings of FEL11*, Shanghai, China, August 2011.

[42] I. Will and G. Klemz, *Opt. Express* **16**, 14922 (2008).

[43] Y. Ivanisenko, Photo Injector Cathode Laser Beam Intensity and Position Monitoring System, Master's thesis, Karazin Kharkiv National University, 2007.

[44] M. Hänel, *Experimental Investigation on the Influence of the Photocathode Laser Pulse Parameters on the Electron Bunch Quality in an RF - Photoelectron Source*, PhD thesis, 2010.

[45] Y. Ivanisenko and PITZ group, Recent gun characterisation results at PITZ, in *Future Light Sources Workshop Talks*, March 2010.

[46] A. Oppelt et al., Status and first results from the upgraded PITZ facility, in *Proceedings of FEL05*, Stanford, California, USA, August, 2005.

[47] V. Paramonov et al., The PITZ booster cavity - a prototype for the ILC positron injector cavities, in *Proceedings of PAC05*, Knoxville, Tennessee, USA, May 2005.

[48] V. Miltchev, *Investigations of the transverse phase space at a photo injector for minimized emittnace*, PhD thesis, Humboldt-Universität zu Berlin, 2006.

[49] S. Khodyachykh et al., Design of multipurpose dispersive section at PITZ, in *Proceedings of FEL06*, Berlin, Germany, August 2006.

[50] J. Rönsch, *Investigations on the electron bunch distribution in the longitudinal phase space at a laser driven RF electron source for the European X-FEL*, PhD thesis, 2009.

[51] J. Bähr, V. Djordjadze, D. Lipka, A. Onuchin, and F. Stephan, *Nuclear Instruments and Methods in Physics Research Section A: Accelerators, Spectrometers, Detectors and Associated Equipment* **538**, 597 (2005).

[52] Hamamatsu Photonics. Universal streak camera C5680 series, Technical report.

[53] L. Kravchuk et al., Layout of the PITZ transverse deflecting system for longitudinal phase space and slice emittance measurements, in *Proceedings of LINAC10*, Tsukuba, Japan, September 2010.

[54] S. Rimjaem et al., Physics and technical design for the second high energy dispersive section at pitz, in *Proceedings of DIPAC11*, Basel,Switzerland, May 2011.

[55] P. Schmüser, M. Dohlus, and J. Rossbach, *Ultraviolet and Soft X-Ray Free-Electron Lasers*, Springer, 2008.

[56] M. Abo-Bakr et al., The BESSY Soft X-ray Free Electron Laser, Technical Design Report, Technical report, BESSY, 2004.

[57] Ayvazyan et al., *Phys. Rev. Lett.* **88**, 104802 (2002).

[58] M. Röhrs, *Investigation of the phase space distribution of electron bunches at the FLASH-linac using a transverse deflecting structure*, PhD thesis, Universität Hamburg, 2008.

[59] H. Edwards et al., 3.9 GHz CAVITY MODULE FOR LINEAR BUNCH COMPRESSION AT FLASH, in *Proceedings of LINAC10*, Tsukuba, Japan, September 2010.

[60] X. Qiu, K. Batchelor, I. Ben-Zvi, and X.-J. Wang, *Phys. Rev. Lett.* **76**, 3723 (1996).

[61] K. Flöttmann, A space charge tracking code - ASTRA, http://desy.de/∼mpyflo/.

[62] SIGMAPHI, 180 degree bending magnet, Technical report.

[63] MINUIT, Function Minimization and Error Analysis, http://wwwasdoc.web.cern.ch/wwwasdoc/minuit/minmain.html.

[64] JAI RM-2030GE camera specification, http://www.jai.com/EN/Products/Pages/TM-2030GE.aspx.

[65] Prosilica GC1350 camera specification, http://www.alliedvisiontec.com/de/produkte/kameras/gigabit-ethernet/prosilica-gc/gc1350.html.

[66] OSLO EDU, http://www.lambdares.com/education/oslo_edu.

[67] S. Rimjaem et al., *Nuclear Instruments and Methods in Physics Research Section A: Accelerators, Spectrometers, Detectors and Associated Equipment* **671**, 62 (2012).

[68] M. Krasilnikov et al., Beam based monitoring of the RF photo gun stability at PITZ, in *Proceedings of BIW10*, Santa Fe, New Mexico, USA, May 2010.

[69] J. Egberts and C. P. Welsch, *Journal of Instrumentation* **5**, P04010 (2010).

[70] M. Otevrel et al., Investigations on thermal emittance at PITZ, in *Proceedings of FEL11*, Shanghai, China, August 2011.

# Acknowledgments

Finally, I'd like to express my sincere gratitude to all people who contributed to the success of this thesis:

- **Dr. Matthias Groß, Dr. Mikhail Krasilnikov, Prof. Jörg Roßbach and Dr. Frank Stephan** for proofreading the thesis, for their comments, suggestions and advice;
- **Dr. Frank Stephan** for supervising this work;
- **all members of the PITZ group 2006-2012** for fruitful discussions and their critical minds.
- **engineers, technical staff, and the DV group** for doing their best for the experiment;
- **Dr. Marc Hänel, Dr. Chase Boulware, Dr. Marek Otevrel and Grygorii Vashchenko** for sharing time, knowledge and the office;
- **Pablo Ruiz de Olano, Xiaohui Wang and Mohammad Tanha** for great cooperation experience with mutual profit;
- **my family, Inna and Denis Ivanisenko** for their endless support, encouragement, and for being the main source of motivation;
- **my parents, Nadiya and Yevgen Ivanisenko,** for their great effort of guiding me to this point.